Plasmonic Superconducting Single Photon Detectors

by

Amin Olah Eftekharian

A thesis
presented to the University of Waterloo
in fulfillment of the
thesis requirement for the degree of
Doctor of Philosophy
in
Electrical and Computer Engineering

Waterloo, Ontario, Canada, 2013

I hereby declare that I am the sole author of this thesis. This is a true copy of the thesis, including any required final revisions, as accepted by my examiners.

I understand that my thesis may be made electronically available to the public.

Abstract

A theoretical model with experimental verification is presented to enhance the quantum efficiency of a superconducting single-photon detector without increasing the length or thickness of the active element. The basic enhancement framework is based on: (1) Utilizing the plasmonic nature of a superconducting layer to increase the surface absorption of the input optical signal. (2) Enhancing the critical current of the nanowires by reducing the current crowding at the bend areas through optimally rounded-bend implementation. The experimental system quantum efficiency and fluctuation rates per second are assessed and compared to the proposed theoretical model. The model originated from an accurate description of the different liberation mechanisms of the nano-patterned superconducting films (vortex hopping and vortex-antivortex pairing). It is built complimentary to the existing, well-established models by considering the effects of quantum confinement on the singularities' energy states. The proposed model explains the dynamics of singularities for a wide range of temperatures and widths and describe an accurate count rate behavior for the structure. Furthermore, it explains the abnormal behaviors of the measured fluctuation rates occurring in wide nano-patterned superconducting structures below the critical temperature. In accordance to this model, it has been shown that for a typical strip width, not only is the vortex-antivortex liberation higher than the predicted rate, but also quantum tunneling is significant in certain conditions, and cannot be neglected as it has been in previous models. Also it is concluded that to satisfy both optical guiding and photon detection considerations of the design, the width and the thickness of the superconducting wires should be carefully determined in order to maintain the device sensitivity while crossing over from the current crowding to vortex-based detection mechanisms.

Acknowledgements

The author wishes to thank several people. Foremost, my sincere gratitude goes to my supervisor, Professor A. Hamed Majedi for his persistent support, useful comments, remarks and engagement through the process of my Ph.D. studies. His guidance helped me in all the time of research and writing of this thesis. I also express my special acknowledgement to my committee members Professor Safieddin Safavi-Naeini, Professor Raafat Mansour and my internal-external examiner Professor Thomas Jennewein. Special thanks to my external examiner, Professor Amr Helmy. I deeply acknowledge all of them for their insightful comments. Many thanks to my fellow colleagues at Integrated Quantum Optoelectronic Lab (IQOL), Mohsen Keshavarz, Amir Jafari Salim, Milad Khoshnegar, Thomas G. McConkey and Haig Atikian at Harvard university for their useful discussions as well for their supports on the way. I also would also like to thank to Institute for Quantum Computing (IQC) for the financial support granted through Mike and Ophelia Lazaridis fellowship. Last but not the least, I would like to thank my family for their support, encouragement, and unshakable faith in my abilities during the course of my studies.

Dedication

I wish to dedicate this thesis to my family, for your continued support and encouragement.

Table of Contents

List of Tables

List of Figures

Nomenclature

BCS	Bardeen, Cooper, and Schrieffer theory of superconductivity
BKT	Berezinskii, Kosterlitz, and Thouless transition temperature
DCR	Dark count rate
DLSPP	Dielectric loaded surface plasmon polariton
FDTD	Finite difference time domain simulation
Fig	Figure
FWHM	Full width at half maximum
HSQ	Hydrogen Silsesquioxane
IR	Infrared bandwidth
MCP	Micro channel plate
MFD	Mode-field diameter
MI	Metal-insulator interface
NIR	Near infrared bandwidth
PMT	Photomultiplier tube
PNR	Photon number resolved single-photon detector

QE	Quantum efficiency
QKD	Quantum key distribution
QP	Quasiparticle
RPM	Reflection pole method
RT	Rate equation
SC/I	superconductor-insulator interface
SEM	Scanning electron microscope
SNSPD	Superconducting nanowire single-photon detector
SPAD	Single-photon avalanche diode
SPD	Single-photon detector
SPP	Surface plasmon polariton
SQUID	superconducting quantum interference amplifier
STJ	Superconducting tunnel junction
TE	Transverse electric mode
TES	Transition edge sensor
TM	Transverse magnetic mode
VAP	Vortex-antivortex pair

Chapter 1

Introduction

Due to the new achievements in the field of quantum information over the past few years, there has been a growing interest in detectors with the capability of ultra-low power detection, particularly those with single-photon sensitivity. Among all the available optical detectors, single-photon detector (SPD) provides the utmost level of sensitivity in optical measurements making it a vital option for quantum information processing. The unique characteristics of these devices distinguish them from their classical counterparts. This is represented by the fact that their response is discernible from the noise level even when the optical intensity is within the range of the quantum of light. SPD's are the only candidates in the applications where physical phenomena with a very small number of photons are involved - often just one. SPDs are essential components in various fields such as quantum optics and information [1], quantum key distribution [2], lunar laser communication [3], diagnosis of integrated circuits [4] and characterization of single-photon sources [5]. Among all available candidates to do the single-photon detection, superconducting nanowire single-photon detectors (SNSPDs) are the most promising devices. They outperform other detectors in properties such as infrared quantum efficiency[1], dark count rate, timing jitter [7], and maximum count rate [8]. Furthermore, they provide wide-band optical detection, a fast response time, and dispose of a platform for potential quantum system integration [9, 10, 11]. This particular class of detectors has applications in dif-

[1] In 2013, an SNSPD detector with 93% system efficiency has been reported in [6]

ferent domains such as astronomy [12, 13], biology and biochemistry [14, 15], quantum key distribution (QKD) [16, 17], linear quantum computation [18], and are considered a promising technology for photon counting applications [19].

In order to evaluate the performance of an ordinary detector, several technical definitions such as noise equivalent power or data transmission rates are followed. However, in the case of single-photon detection, the quantum nature of these devices raises the need for a new set of quantum level parameters. Summarized below are, those parameters and specifications that will be used frequently throughout this thesis,

- Quantum Efficiency (QE): QE in general is the probability of detecting a photon by a detector. More precisely, it is the ratio of output click rate to input photon rate. Depending on the location of the input and output measurements, it can be divided into internal or external quantum efficiencies [20]. In the former case, QE is only dependent to the internal parameters. In latter definition, however, the entire system is seen as a single block and all measurements are performed at the input and output terminals. For the most part, this parameter is highly optical wavelength-dependent and is evaluated as to how effectively the incoming single-photons are converted to discriminated-electric pulses.

- Dark Count Rate (DCR): This is the output rate of electric pulses when the input optical signal is entirely blocked or the detector is in an absolute darkness. This parameter represents a proper measure of the detector's noise performance.

- Timing Jitter: It expresses the deviation in time resolution of a detector and is computed by measuring the full width at the half maximum (FWHM) of the delay histogram between photo-excitation and photo-registration events.

- Maximum Count Rate: This specifies the minimum amount of time delay required by a detector to perform another successful detection. There is no unique definition for this parameter; however it is usually defined as the sum of output rise and fall (recovery) times [21].

Apart from these *intrinsic* parameters, there are other important criteria that help the selection of an appropriate single-photon detector. Some important parameters are listed below:

- Operation temperature;
- Size of detector's active element;
- Size of the entire detection system;
- Sensitivity and dynamic range of the detector;
- Complexity of the readout circuit;
- Implementation cost;
- The capability of being integrated.

Single-photon detectors can also be classified based on their capability to recognize the number of incoming photons. The vast majority of available single-photon detectors can only differentiate between the presence and absence of photons. Photon number resolved (PNR) single-photon detectors cannot only distinguish between the presence and absence of photons, but can also provide information about the number of photons that the detector comes into contact with. In order to assess the relative performance of the proposed detector among other available counterparts, and to reveal the motivation for this work, different state of the art single-photon detection mechanisms are presented below:

Photomultiplier Tube (PMT): Photomultiplier tubes are the most long-established single-photon detectors. They consist of a vacuum tube along with a GaAsP or InP/InGaAs photocathode which absorbs optical power from an input terminal. The absorption of photons in the photocathode triggers the photoelectric effect and produces many excited electrons. These excited electrons then flow through the vacuum tube, producing a weak electric current. This current is multiplied by a cascade of secondary electron-emissions until a sensible current is produced at the output terminal. The spectral range of a PMT is governed by the material of the photocathode element such that the energy of absorbed

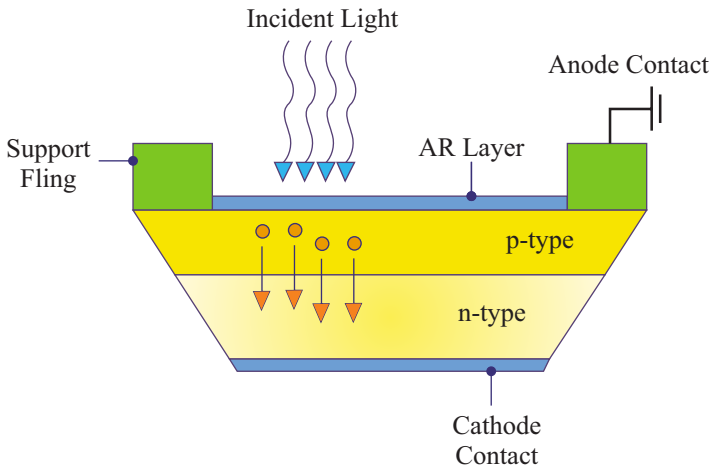

Figure 1.1: Schematic of an avalanche photodetector. The large external bias accelerates photoelectrons so that each primary electron ultimately results in thousands of electrons at the electrode terminals.

photon must exceed the work-function of the photocathode material in order to have excited electrons. This class of single-photon detectors is primarily carried out in visible bandwidth, as their quantum efficiency drops rapidly at longer wavelengths [7].

Single-Photon Avalanche Diode (SPAD): These are solid-state based photodetectors that are usually manufactured using either silicon or InGaAs/InP materials. In the former case, the sensitivity is from visible wavelengths to about 1000 nm which is restricted by the silicon's band gap. However in the latter case, the operation wavelength can be up to 1700 nm. In both cases, the quantum efficiency drops rapidly for frequencies which are greater than the band gap frequency. The operation is based on a reverse biased p-n junction such that the electric field is so high that even a single-photon injected into the depletion layer can cause a self-sustaining avalanche process.

Transition Edge Sensor (TES): Transition edge sensors are also referred to as superconducting phase-transition thermometers. They consist of a micrometer-sized superconducting thin-film which operates in a narrow temperature domain close to their critical temperature. In this way, the electrical resistance after absorption of a single-photon varies from the superconducting to non-superconducting values. In general, the absorption event

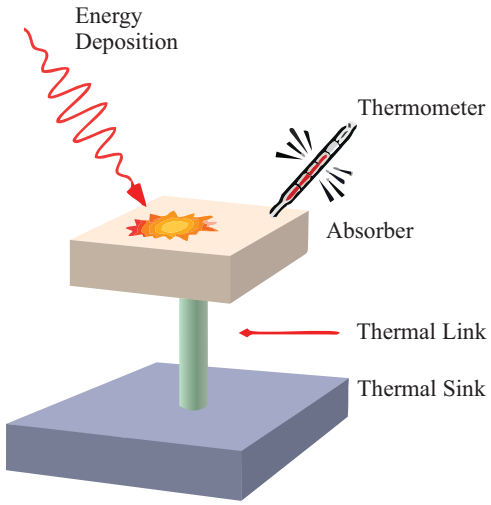

Figure 1.2: Schematic of the operation of a TES single-photon detector [24].

pushes the detector, which was in the superconducting state, into the normal state by momentarily changing the local temperature and hence increasing the electrical resistance. This small increase in the resistance is then amplified by a series of high-gain superconducting quantum interference amplifiers (SQUIDs) [22, 23].

Superconducting Tunnel Junction (STJ): Superconducting tunnel junction consists of two superconducting elements separated by a thin insulating barrier (the photodetection element in this detector is a Josephson junction). After the absorption of an optical photon in one of these pads, superconducting pairs will be excited to free excess charge carriers (quasiparticles) provided that the energy of a single absorbed photon is greater than the superconducting energy gap Δ. As these quasiparticles penetrate the barrier, they generate a temporary increase in the device current. This class of detectors is renowned for their high energy resolution. This high resolution is mainly due to the fact that the energy required for generation of an excess charge (about 1 meV) is about an order of magnitude smaller than the energy gap of a typical semiconductor counterpart. This implies an improved energy resolution of about $(1000)^{0.5}$ in this detector [25]. In an actual STJ detector, the superconducting elements consist of two different superconducting layers: a thick absorber with a large energy gap Δ_{abs} for high efficiency and a thin trapping layer with small energy gap Δ_{trap} for fast tunneling performance (see Fig 1.3). Quasiparticles

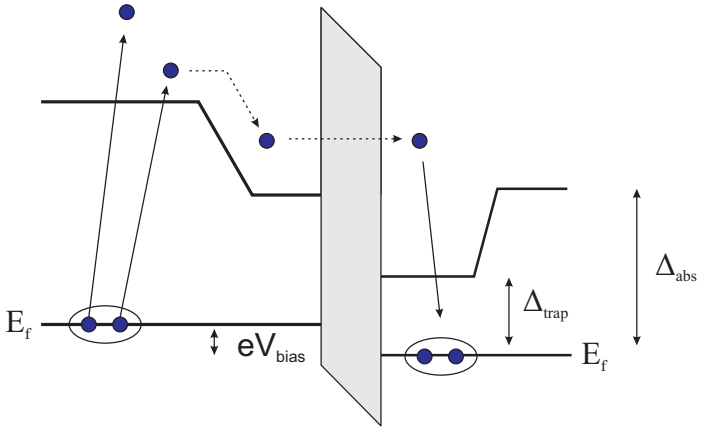

Figure 1.3: Band diagram of an STJ detector with a trapping layer in each superconducting element. Photon absorption generates excess charge carriers producing a current pulse through direct quantum tunneling of the carriers.

are absorbed in the absorbing layer and then trapped in the lower-gap region by inelastic scattering. In this detector, photoexcited quasi-particles usually tunnel several times by breaking many superconducting pairs until their energy reduces to 2Δ, which is insufficient for further pair breaking. At this point, they regroup to form a new superconducting pair. While this detector is mainly an X-ray detector, it also has applications in visible and infrared optical detection as well.

Superconducting Nanowire Single-Photon Detector (SNSPD): The active element of a superconducting nanowire single-photon detector is a meander line made from an ultrathin superconducting material. The absorption of a single-photon similar to a localized quasiparticle injection introduces a local nonequilibrium perturbation with an excess number of excited quasiparticles[2]. This change in the number of the superconducting pairs results in the depression of the local superconducting gap. Accordingly, the bias current tends to expel from the hotspot region to the sidewalks between the hotspot and the edges of the film where superconductivity is still stronger. The presence of a higher current density in these regions weakens the superconducting gap at the sidewalks. If the

[2]This also leads to an increase in the effective temperature of the film

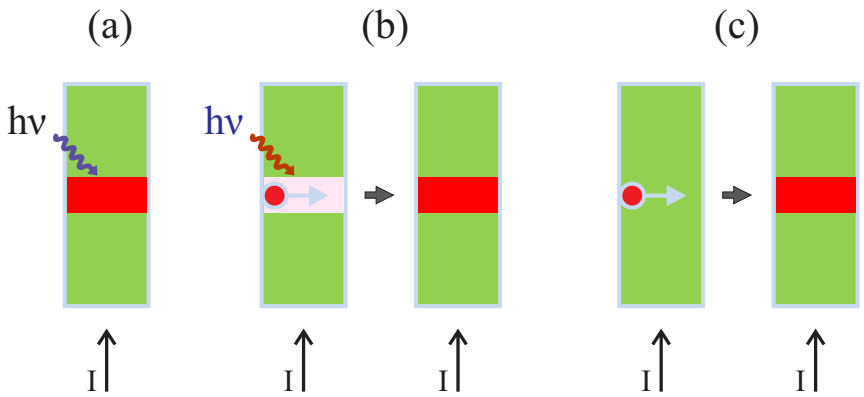

Figure 1.4: Schematics of the formation of a normal belt across a superconducting nanowire which results in a detectable voltage pulse. (a) Direct photon count. (b) Vortex-assisted single-photon count. (c) Dark count.

current density reaches the maximum allowed value (equivalent to zero energy gap), there would be a transition from the superconducting state to a normal state which results in the formation of a local resistive barrier across the entire cross-section of the nanowire. Eventually, since the device is biased with a constant current, this resistive barrier leads to the generation of a detectable voltage pulse [26].

Aside from this mechanism of the normal belt generation, there are two other mechanisms all resulting in equivalent voltage pulse generations. The first one is vortex assisted single-photon detection. It occurs when the input photon has insufficient energy for generating an initial hotspot, but it has enough energy to initiate a subsequent vortex crossing. The cross of this vortex generates a normal belt across the wire width and, due to the same physical origin, a voltage pulse is formed at the output terminal. Another source of voltage pulse generation in the absence of input photons is the vortex crossing. This process is initiated with either thermal activation or dissipative quantum tunneling of the vortices located at the edges of the film. These three different methods of voltage pulse generation mechanisms are summarized in Fig. 1.4.

Generally, it is not meaningful to compare the performance of these single-photon detectors through a set of independent parameters, as each detector offers potentials for a particular application. Nevertheless, to get an insight about the general performance of

Table 1.1: Perfomance comparison of commercially available single-photon detectors.

Detectors	Si	InGaAs	SNSPD	TES	STJ
Temperatures (K)	300	200	$2-4.2$	0.1	0.4
Wavelength (μm)	$0.4-1.1$	$0.9-1.7$	$0.4-5.6$	$0.1-5$	$0.2-1$
Time Resolution	300ps	300ps	18ps	300ns	$<$ 2ns
Quantum Efficiency	70% @ 630nm	25% @ 1.55μm	10% @ 1.55μm	92% @ 1.55μm	50% @ 500nm
Dark-Count Rate (Hz)	<25	$<10^4$	<0.01	<0.001	N/A
Maximum Count Rate	10MHz	1MHz	250MHz	20KHz	50KHz

SPDs in terms of operation temperature, wavelength, quantum efficiency, and dark count rate, we could refer to tables similar to table 1.1 which is found in the literature [27, 7].

1.1 Goal of This Thesis

The main objective of this work is to introduce an *integrated* version of a superconducting single-photon detector. The idea is to have a detector as a part of an integrated optical system such that all processes including photon generation, guiding, and detection could take place inside a single chip. Furthermore, to have a compatible device with a general optical fiber communication network, the detector should also preferably operate within the infrared bandwidth. This is primarily due to the fact that the minimum absorption window for a common silicon fiber occurs at this bandwidth.

Generally, sensitivity at this frequency range is more challenging than that of a visible light, as the amount of energy carried by each quantum of light is smaller for cases of telecom photons. Among all detectors introduced in the table 1.1, InGaAs based detectors, SNSPDs, and TESs are the best candidates for telecom bandwidth.

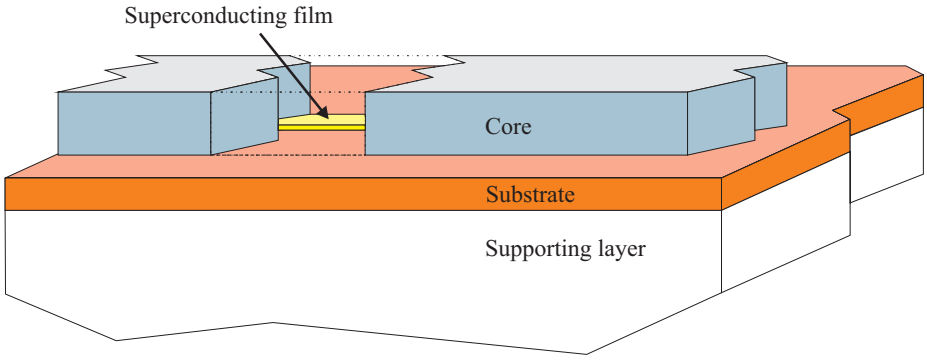

Figure 1.5: Schematic of our proposed plasmonic detector. As an alternative configuration, the superconducting layer can be placed on top of the dielectric core layer as well.

Preference of TES over SNSPD is usually due to its photon number resolution and higher quantum efficiency at near-infrared (NIR). However, the operation temperature of this class of detectors is much lower than SNSPD (about 0.1 K), which demands a lot of precautions and preparations. Thus, if photon number detection is not a concern[3], usage of SNSPD becomes more inclined. Having high maximum count rate, low timing jitter, very small dark count rate, and high quantum efficiency, especially at NIR, are among the points that motivated us to base our work on this class of detectors.

As mentioned before, the active element of an SNSPD is a superconducting nanowire. To have a reasonable operation temperature, the critical temperature of the superconducting material should be at least two times greater than the liquid helium bowling temperature, even when the film is narrowed down to a few nanometers of thicknesses[4]. Nb [28], NbN [29] and NbTiN [26] are among those superconducting materials that have high critical temperatures. In addition they have known electrical and optical parameters and established thin-film technology. This makes them an ideal choice for selection as the

[3]For number state photon statistics, looking at a sample at a time window T is equal to sample the spatial length of $v_g T$ at a single time-shot. This sample has a statistical distribution with variance of $\Delta n = 0$ where $|n\rangle$ is the number state. This implies that the chance that two or more photons simultaneously hit the detector is zero. So if a number stater single-photon source is available, there is no need to have a detector which is sensitive to the number of photons.

[4]To have high performance, SNSPD is usually operated at temperature less than $T_c/2$.

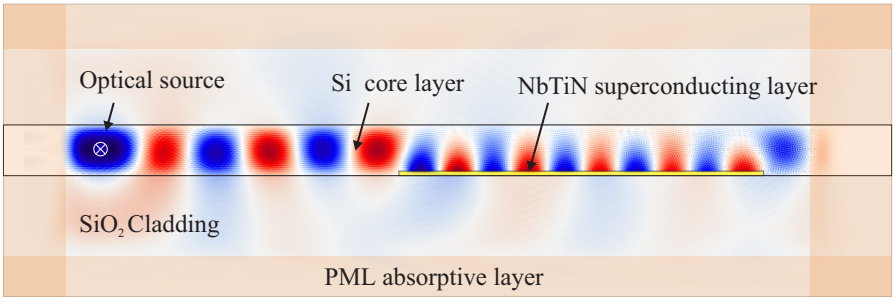

Figure 1.6: Two-dimension FDTD simulation for TM mode of a dielectric loaded plasmonic waveguide. The dispersive layer is NbTiN with a thickness of 20 nm and the guiding channel is silicon. Both cladding layers are SiO_2. The operation wavelength is 1310 nm. Before optical wave reaches the dispersive layer, power concentrates at the center of the core layer. However, in the dispersive section, the field is compressed into sub-wavelength dimensions around the dispersive layer.

active element. The spectral cut-off frequency for Nb thin-film occurs at the wavelength less than 0.25 μm, while for NbN and NbTiN the corresponding wavelength exceeds 2 μm [29]. Furthermore, Nb thin-film is more susceptible to latch into a finite voltage state instead of self-resetting to the superconducting state after detecting a single-photon than NbN or NbTiN counterparts. This is due to the fact that phonon mediated cooling in this film is much slower [30]. As a consequence, Nb detectors are less desirable for high count rate applications. To provide high sensitivity at NIR bandwidth, NbTiN has been chosen as the active element of the detector in this work.

For single-photon detectors, the total quantum efficiency or system detection efficiency, η, can be expressed as a product of three independent factors: $\eta = \eta_c \times A \times P_r$, where η_c is the coupling efficiency, which is the probability that an incident photon from free space or a fiber reaches the active area of the detector; A is the absorptance of the active area, which is the probability that the photon is absorbed by the film once it has reached the active area, and P_r is the voltage-pulse generation probability for absorbing the incident photon [26].

Generally, enhancing the $\eta_c \times A$ for an SNSPD is not a trivial task; mainly because in

practice, (1) the length of nanowire is limited by the kinetic-inductance of the wire [31]. This kinetic-inductance put an upper limit to the nanowire length and hence the size of the active area, and this size is usually smaller than the size required for achieving an efficient coupling. (2) There is a great difference between the thickness of the superconducting film and skin depth of the optical wave and therefore the input optical wave readily passes through a normal-incidence meander-line structure [32]. Intuitively speaking, to enhance the $\eta_c \times A$ of a detector, the *spatial overlap* between the light and active area must be enhanced. In traditional SNSPDs, to do so, one can place a reflector beneath the active area such that if a photon passes through the detector, with some possibilities, it could reflect back to the active area [26] or additionally, the detector could be placed in an optical cavity to increase the absorption probability [33]. However, in this work, I tried to enhance the photon absorption by using the idea of plasmonic guiding. Plasmonic guiding is an alternative to the standard dielectric waveguiding. Over the past decades, this guiding method attracted great interest as it can compress the spatial cross-section of an optical mode to sub-wavelength dimensions[5] and moreover, it combines the small size of electronic circuits with the speed of optical circuits.

In this work, I present a new single-photon detection structure to address these issues without increasing the length or the thickness of the active element such that two seemingly contradictory properties, high speed operation (requiring small active area) and high photon absorption probability (requiring large active area), can be maintained simultaneously. The design is based on the plasmonic nature of the superconducting layer [34] to improve the photon absorption process by exciting the surface plasmon polaritons, SPPs, at the interface of the superconducting layer and a positive index dielectric layer [35]. Here, the active element is patterned on the top or bottom of a dielectric slab waveguide. Likewise a normal insulator/metal/insulator (IMI) plasmonic structure, the optical interaction occurs through a dielectric channel and hence there is no direct optical excitation anymore. The schematic of the layers is shown in Fig. 1.5. To get an insight about the operation, a two-dimensional finite difference time domain simulation is performed and the result is presented in Fig. 1.6. If the dimensions of the both plasmonic and core layers are chosen properly, the optical mode will be confined in the proximity of the nanowire layer (nega-

[5]This allows a low bending loss

tive index layer) as it reaches to the active area. Thus, in contrary to traditional SNSPD structures, the difference in the length scales of the nanowire and the input optical wave is not a limiting factor anymore which concludes a significant enhancement of the absorption probability. Furthermore, since the initial guiding occurs inside a dielectric channel, ideally no power is transfered to the radiation modes of the system and hence the only source of loss is the absorption inside the dispersive superconducting section. In an actual device, to provide fiber coupled operation, an inverse taper is placed at the tip of the dielectric channel to minimize the coupling loss at the connection port. By choosing the right dimensions and materials for the taper, the coupling loss can be negligibly small.

1.2 Outline of the Thesis

Similar to a typical SNSPD, the active element of the proposed detector is made of current biased meandering superconducting nanostrips with 180 and 90-degree turns. The photons are guided through a dielectric structure and are absorbed in the straight section of nanowires, while the turns only serve the purpose of electrical connection and thus do not directly contribute to the photon detection. However, they can degrade the overall performance of the detector by acting as current bottlenecks or by generating dark counts as the current crowds at the inner edges of these turns and thus reduces the measured critical current of the entire structure. In chapter 2, I will try to address these problems by introducing an optimum design for the turns. It will be shown that there exists an optimum design for an arbitrary bend shape where no current crowding occurs at the inner edge of the bend and hence no reduction in critical current is expected.

As mentioned before, reduction of the experimental critical current is degrading the overall performance of the system. The primary source of this reduction is discussed in chapter 3. It will be shown that in an experimental detection process, even when the input terminal is fully blocked, still randomly distributed signals (clicks) are still generated at the output electrical terminal of the detector if the current is close to the critical current of the nanowires. These dark count events are of great importance not only because they affect the precision of input photon rate to output click rate conversion, but also because of

their adverse effect on the maximum achievable critical current of the device. In short, the presence of these dark counts dramatically degrades the overall performance of an SNSPD. In this chapter, the origins of dark count generation will be discussed in detail. I will provide a clear picture of all the processes that lead to this dissipative transition of the initial metastable state of a general superconducting nanostrip in the absence of an input signal.

In chapter 4, the general guideline to design a plasmonic detector is provided. It will be shown that to observe well-defined plasmonic confinement in a thin superconducting layer, there is a minimum feature size for the width of both the dielectric waveguide and the superconducting layer. This imposes an undesired limitation on the nanowire from a detection perspective, particularly on single-photon sensitivity, since there is an upper bound for the cross section area of the active element to be sensitive to single-photons. In general, it will be shown that that there is a trade-off between the probability of photon absorption and the internal quantum efficiency of the device. I will also present an alternative to decouple these two phenomena based on the optical design and photon detection mechanisms of the detector.

Although the principal goal of this work is to present a single-photon detector for integration purposes, still free-space or fiber-coupled operations are of great importance. Chapter 5 addresses two different coupling mechanisms. The first one is end-fire excitation which is suitable for fiber-coupled operation and the other one is grating excitation which is often used in free-space detections. I will show that the end-fire excitation can provide a high performance coupling at the expense of performing a precise alignment of the input fiber to the actual detector. However, in the case of the grating excitation, the alignment is done without any great effort, but it lacks the high coupling performance.

Chapter 6 is dedicated to the conclusions and contributions of this work. As a closing note, the primary challenges of this work are reviewed here:

1. From an optical point of view, the thickness of the superconducting layer needs to be greater than the skin depth of electromagnetic field inside the dispersive layer; however, to have single-photon sensitivity, the thickness of the superconducting strip is limited to a few nanometers.

2. Same issue is valid for the width of the nanowire. Again from an optical point of view, we are interested in large surfaces; however, from an electrical point of view, the narrower the film is, the better the electrical performance.

3. To have high quantum efficiency, a long strip is of interest. In fact, the longer the strip is, the greater the probability of absorption of the nanowire is. However, it is known that the length of the nanowire is directly related to the operation speed of the detector and hence this would be at the expense of having a slow speed detector. This implies a trade-off between the operation speed and the quantum efficiency.

Chapter 2

Superconducting Nanowire Design

In the proposed plasmonic structure, similar to a typical SNSPD (Fig. 2.1), the active element of this detector is made of current biased meandering superconducting nanostrips with 180-degree turns[1]. The photons are guided to nanostrips that form the active area, while the turns only serve the purpose of electrical connection. The closer the bias current is to the critical current of the nanostrips, the higher the detection efficiency, but also the higher the dark count rate [19]. Although the turns are typically placed outside the photon absorbing area, and thus do not directly contribute to the photon detection, they can degrade the overall performance of the detector by acting as current bottlenecks or by generating dark counts.

Recently, Clem et al. [36] recaped the possible impact of sharp turns on SNSPDs: the current crowds at the inner edge reducing the measured critical current of the meander. Also, the current bottleneck in wide superconducting strips (300nm to 1μm wide) with sharp bends has been experimentally demonstrated [37, 38]. However, an open question remains on the impact of current crowding on present SNSPDs that feature much narrower strips ($\sim$ 100nm wide), in which both increased ratio of the bend curvature (due to inherent finite fabrication resolution) to nanowire width, and reduced width to coherence length ratio make the expected effect smaller [36, 38].

[1]Note that the number of turns has been greatly reduced in the proposed structure. A schematic of the final design is shown in Fig. 4.9

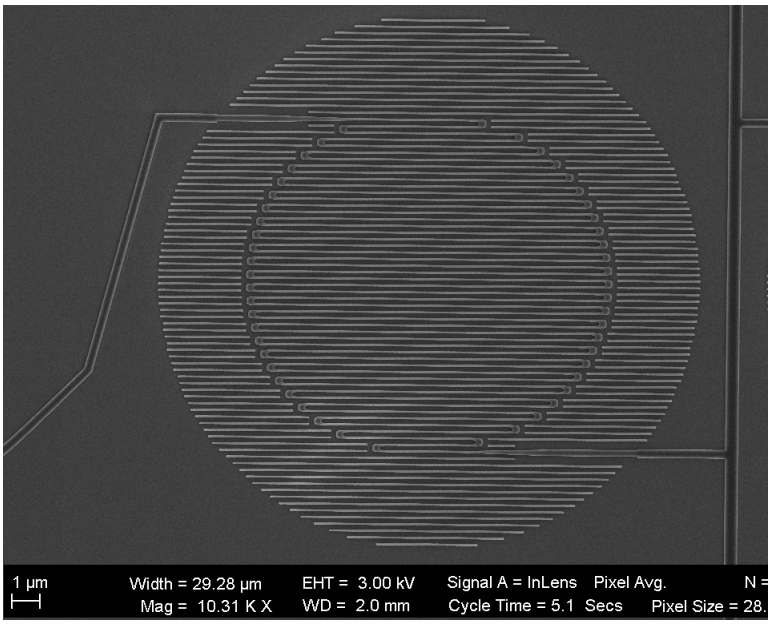

Figure 2.1: High resolution SEM image of a typical SNSPD detector. The fabrication of this project has been done in collaboration with Loncar's group at Harvard university. The actual active element is surrounded by a dummy structure to maintain the uniformity of the beam dose distribution during the fabrication process [39].

In this chapter, we present experiments that probe the current crowding effect on the critical current of superconducting nanostrips with a width comparable to the commonly used width in modern SNSPDs.

2.1 Devices and Setup

A typical device presented is illustrated in Fig. 2.2(a). A nanowire, 100nm wide and 8nm thick, is bent either 90-degree or 180-degree, and connected to large pads by a gradual transition to wider strips, similar to Fig. 2.1. The nanowire length is $\sim 0.5\mu$m on either side of the bend. Our bends fall into two categories: optimally designed with no current crowding and thus no expected critical current reduction, and traditional bends made without optimal considerations.

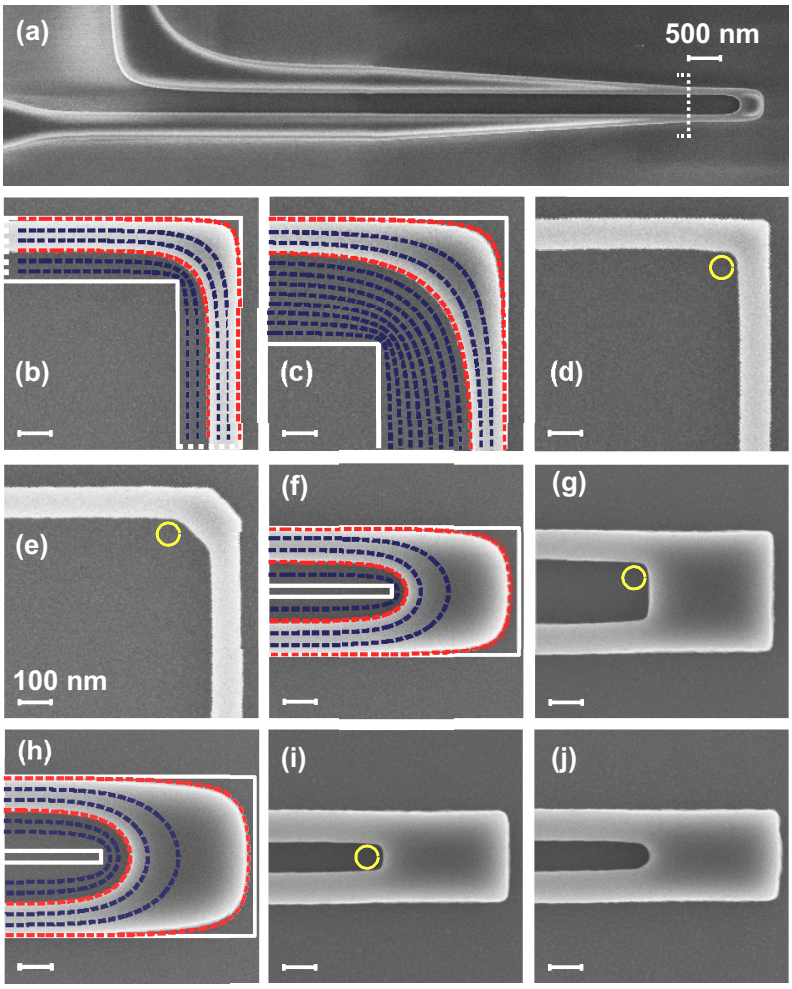

Figure 2.2: Scanning electron microscope images of the nanowires explored in this chapter. (a) A typical nanowire structure and its connection lines. (b) and (c) two optimized 90-degree bends. (d) and (e) sharp and 45° 90-degree bends. (f) and (g) optimized and sharp 180-degree turns with 200nm spacing. (h) optimized 180-degree turn with 300nm spacing. (i) and (j) sharp and circular (radius = 50nm) 180-degree turns with 100nm spacing. The circles are eye guides with 35nm radius. Blue and red dashed lines are current streamlines calculated for a superconductor thin-film enclosed by solid white lines. All the parts, except (a) share the same length scale [21].

Figure 2.2(b) shows an example of our optimum bends. To find the optimal bend design, we numerically solve $\nabla \cdot \mathbf{K} = 0$ and $\nabla \times \mathbf{K} = -d/\lambda^2 \mathbf{H} \approx 0$ within the area enclosed by the white lines [36], where $\mathbf{K}$ is the sheet current density, d is the nanowire thickness and λ is the magnetic penetration depth. The boundary conditions are $\mathbf{n} \cdot \mathbf{K}_l = 0$, and $\mathbf{n} \times \mathbf{K}_i = 0$, where $\mathbf{n}$ is a vector normal to the edge, $\mathbf{K}_l$ is $\mathbf{K}$ on the lateral boundaries (solid white lines) and $\mathbf{K}_i$ is $\mathbf{K}$ on the input boundaries (dotted white lines). Next, we find the streamlines of the vector field $\mathbf{K}$ (dashed blue and red lines). Any two streamlines (dashed red lines) that enclose a surface within which $|\mathbf{K}|$ remains less than or equal to $|\mathbf{K}|$, form an optimized bend (because $\mathbf{K}$ within them satisfies the same above boundary value problem, and $|\mathbf{K}|$ in the bend does not exceed $|\mathbf{K}|$ within the nanowire).

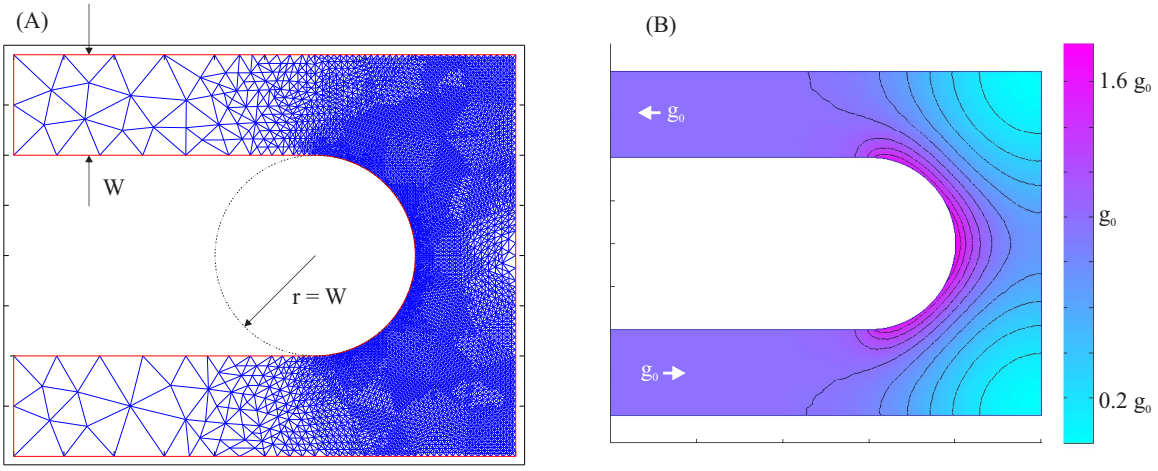

Figure 2.3: An example simulation result for modeling current crowding in nano-patterned superconducting structures. Part (A) depicts finite element meshing of a sample structure. Part (B) displays current crowding due to the presence of a 180-degree turn. According to this result, even for a fully rounded inner corner, still current crowding is considerable. This excess inner current density reduces the maximum tolerable current of the entire meander structure and hence reduces the maximum achievable quantum efficiency of the detector.

The approximation $\nabla \times \mathbf{K} \approx 0$ used in above calculations is valid as long as $w \ll \lambda^2/d$, where w is the width of nanowire (see [36] for a thorough discussion). For typical SNSPD

designs, w is less than $\sim 100nm$ while λ^2/d is larger than tens of μm [37]. Therefore the condition $w \ll \lambda^2/d$ is satisfied and the optimal designs remain independent of the exact values of λ and d. This brings robustness to the fabrication and also scalability of designed bends (as long as the condition $w \ll \lambda^2/d$ holds).

Four different 90-degree bends have been investigated: (i) optimized bend with the smallest possible footprint, (ii) optimized bend twice as big as the smallest one (to make it more tolerant to fabrication errors), (iii) sharp bend and (iv) 45° bend (as a structure between worse and best case scenarios) (see Figs. 2.2(b) through 2.2(e)). The smallest possible optimum 180-degree turn (200nm spacing) is shown in Fig. 2.2(f). It will be compared with a sharp 180-degree turn (200nm spacing) and a bigger optimum turn (300nm spacing) as shown in Figs. 2.2(g) and 2.2(h). Finally, Figs. 2.2(i) and 2.2(j) present a commonly used bend in present SNSPDs (sharp bend with 100nm spacing) and the same but circularly rounded (radius is equal to 50nm).

The critical current, dark count and photoresponse of a nanowire is a function of its dimensions (thickness and width), as well as the superconducting thin-film quality. Therefore, when investigating the effect of bend design, it is essential to keep the nanowires identical except at the bend. In our experiments, we only compare a set of different bends from the designs in Fig. 2.2 that satisfy the following conditions: (i) the bends in a set are either 90-degree or 180-degree, and (ii) they are fabricated few μm apart on the same chip. The first condition keeps the geometries as similar as possible and therefore minimizes slight width changes when different geometries are exposed by the electron beam. The second condition assures the nanowires share the most identical film thickness/quality as well as equivalent fabrication processing (to make effects of many factors including resist variations, proximity dose effects, and others less significant).

The nanowires on any given chip share a common electrical ground. Each of the other terminals connects to a 470nH inductor (placed next to the chip) and then to a room temperature bias-T by a coax cable (50 ohm impedance). A computer controlled voltage source that measures its output current (Keithley 2400) is connected to the DC port of the bias-T via a low-pass filter (to reduce high frequency noise and interference). The high frequency response of the nanowire (after room temperature amplification) is monitored through the RF port on an oscilloscope or a programmable counter. A single mode fiber, placed several

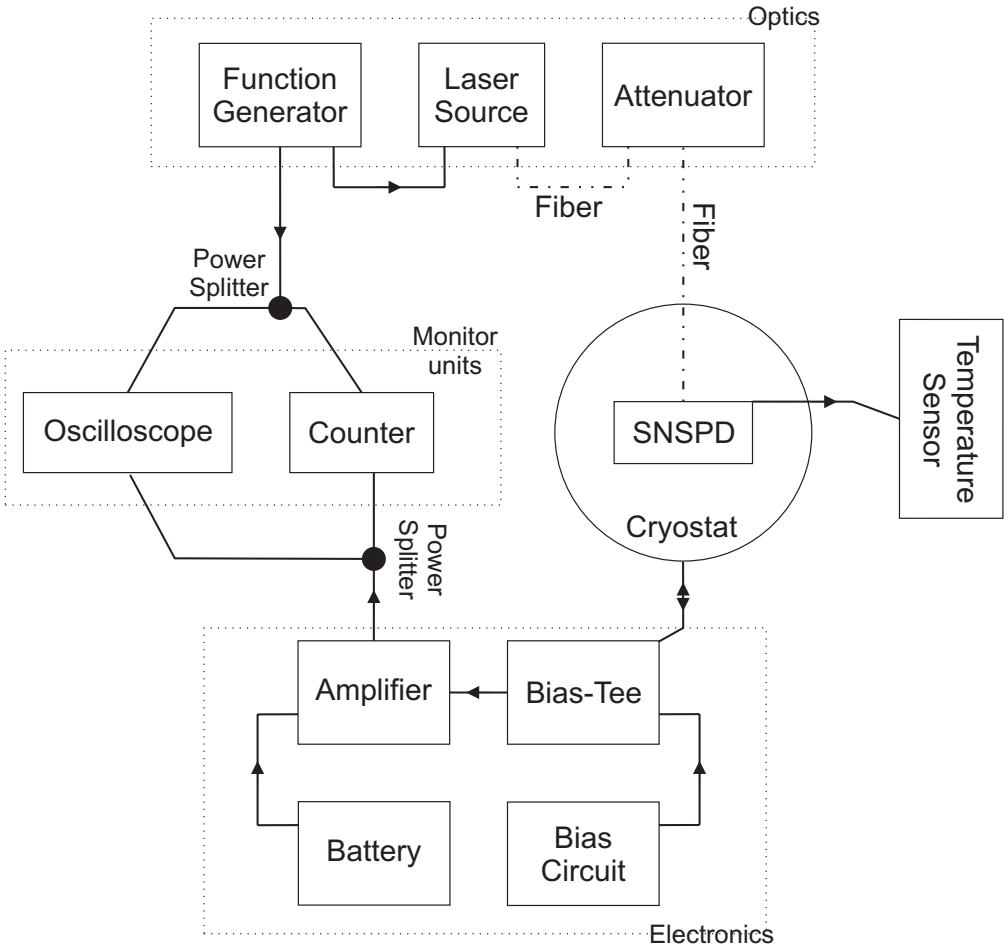

Figure 2.4: Schematic for experimental setup

centimeters away from the chip uniformly radiates the nanowires with 1310nm photons from an attenuated pulsed laser source (width $\sim$ 200ps, repetition rate 20MHz). The 50 ohm impedance together with the inductor make a large enough time constant to observe relaxation oscillations in all our current-voltage curve measurements, thus ensuring the peak current is the (experimental) critical current [31]. The measurements have been done by installing the samples in a dipstick probe and immersing it in liquid Helium (monitored temperature $\sim$ 4.2K). The schematic of our setup is shown in Fig. 2.4.

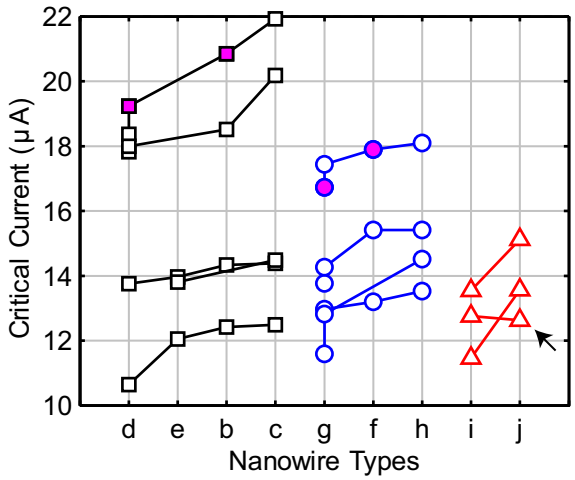

Figure 2.5: Measured critical currents of the nanowires. The horizontal axis specifies the type of bend design by using labels that correspond to the insets of Fig 2.2. The data points for the devices that were on the same chip are connected by solid lines.

2.2 Results and Discussions

Figure 2.5 summarizes the critical current (I_c) measurements on 38 nanowires with different designs that were fabricated on 12 chips. The horizontal axis specifies the type of device using the characters that name the bends in the insets of Fig. 2.2. It divides the bends into three categories: 90-degree (black squares), 180-degree with a big enough footprint to support the optimized design (blue circles), and 180-degree smaller than the minimum size to support the optimized design (red triangles). It also sorts the bends in each category in accordance to their optimality from left to right. The symbols that are connected by solid lines show the critical currents of the nanowires within the same chip. We have confirmed satisfactory operation of our measurement setup by measuring the critical current of our devices several times and finding negligible mean normalized error (equal to $\sim 0.4\%$).

We start by looking at the data for the optimum bends for which we expect no variation in critical current due to current crowding. The average I_c of devices c and h fabricated on all chips is 16.1μA with standard deviation (σ) of $3.2/16.1 = 20\%$. For devices on the same chip, the I_c of device b compared to the I_c of device c shows an average value

$\langle I_c^b/I_c^c\rangle = 97\%$ with $\sigma = 2.0\%$. Also, for devices on the same chip $\langle I_c^f/I_c^h\rangle = 98\%$ with $\sigma = 1.3\%$.

Little improvement from the smallest optimum design to the bigger one shows the validity of our design approach. The $2-3\%$ improvement can be attributed to smaller current density at the inner edge of the bigger designs and therefore their improved tolerance to fabrication errors. The small deviations (2.0% and 1.3%) show reliability of the fabrication within a chip. However, the larger deviation (20%) suggests variation of parameters from chip to chip. Investigating the devices under scanning electron microscope, we have not observed significant dimension changes. Therefore, an optimum design remains optimum on all chips, and the 20% is most probably due to slight film thickness/quality change from chip to chip.

Restricting the comparison to the devices that are on the same chip, a trend becomes clearly visible on Fig. 2.5 for almost all the samples: the more optimal the bend, the higher the critical current. For devices on the same chip: $\langle I_c^d/I_c^c\rangle = 88\%$ with $\sigma = 3.6\%$, $\langle I_c^g/I_c^h\rangle = 91\%$ with $\sigma = 3.9\%$ and $\langle I_c^i/I_c^j\rangle = 92\%$ with $\sigma = 8.5\%$. The average numbers show the sharpest bends considerably reduce the critical currents.

Another observation is an increase in σ when comparing two optimal bends (2.0% and 1.3%), to higher values when comparing a sharp bend with an optimum bend (3.6%, 3.9% and 8.5%). We attribute this to the uncontrollability of the radius of curvature ($\sim$ 35nm, see yellow circles of Fig. 2.2) for sharp bends. For the devices i and j the variation is big enough to almost change device i to j (compare images in Fig. 2.2(i) and Fig. 2.2(j)). This can justify the only exception (marked by an arrow in Fig. 2.5) in all the data, in which contrary to the general trend a rounded bend in device j shows slightly lower I_c than a sharp bend in device i. This can be also a possible explanation for small fabrication yield of SNSPDs [19] where the large number of serially connected 180-degree turns in a meander makes having at least one very sharp bend quite possible.

We have also measured the dark counts and photon counts generated by the nanowires. The room temperature end of the fiber was blocked by a shutter for dark count vs bias current measurements. Photon counts are measured by exciting the nanowires with weak laser pulses and subtracting the expected dark counts at the same bias. We ensure single-

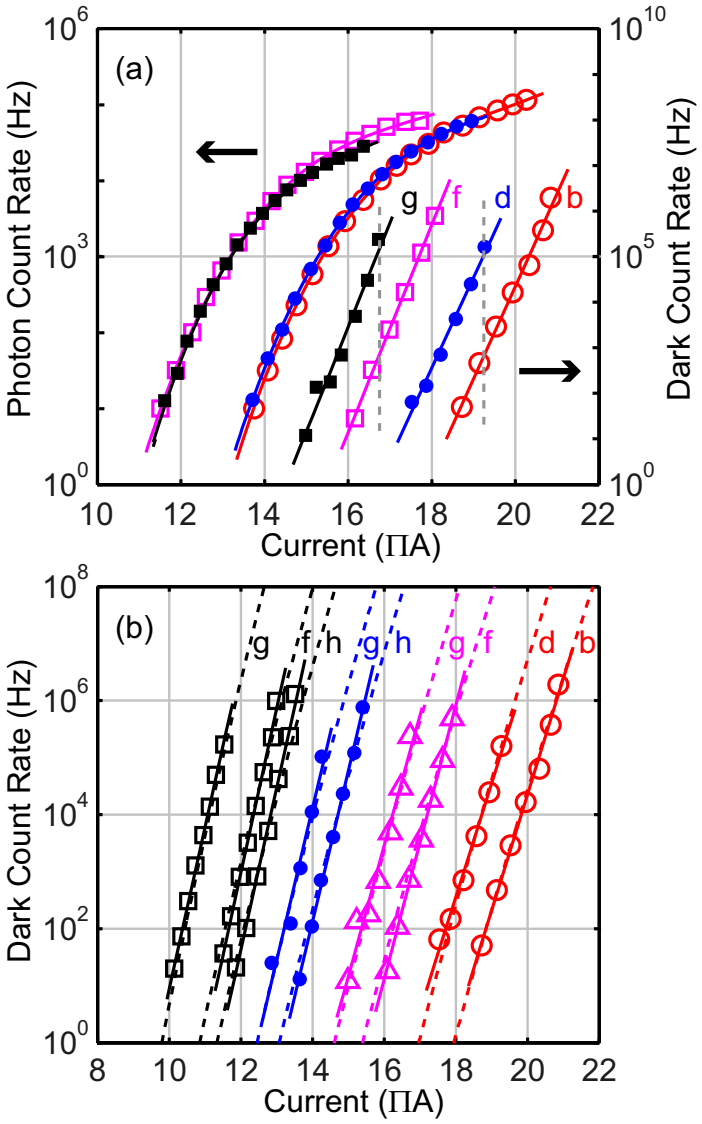

Figure 2.6: (a) Photo-response and dark count measurements for samples of devices d/b and g/f. These samples are marked on Fig. 2.5 by filled symbols. (b) Dark count measurements for more samples. Each symbol is for devices on the same chip. The letters refer to insets of Fig. 2.2. All the lines are for eye guide.

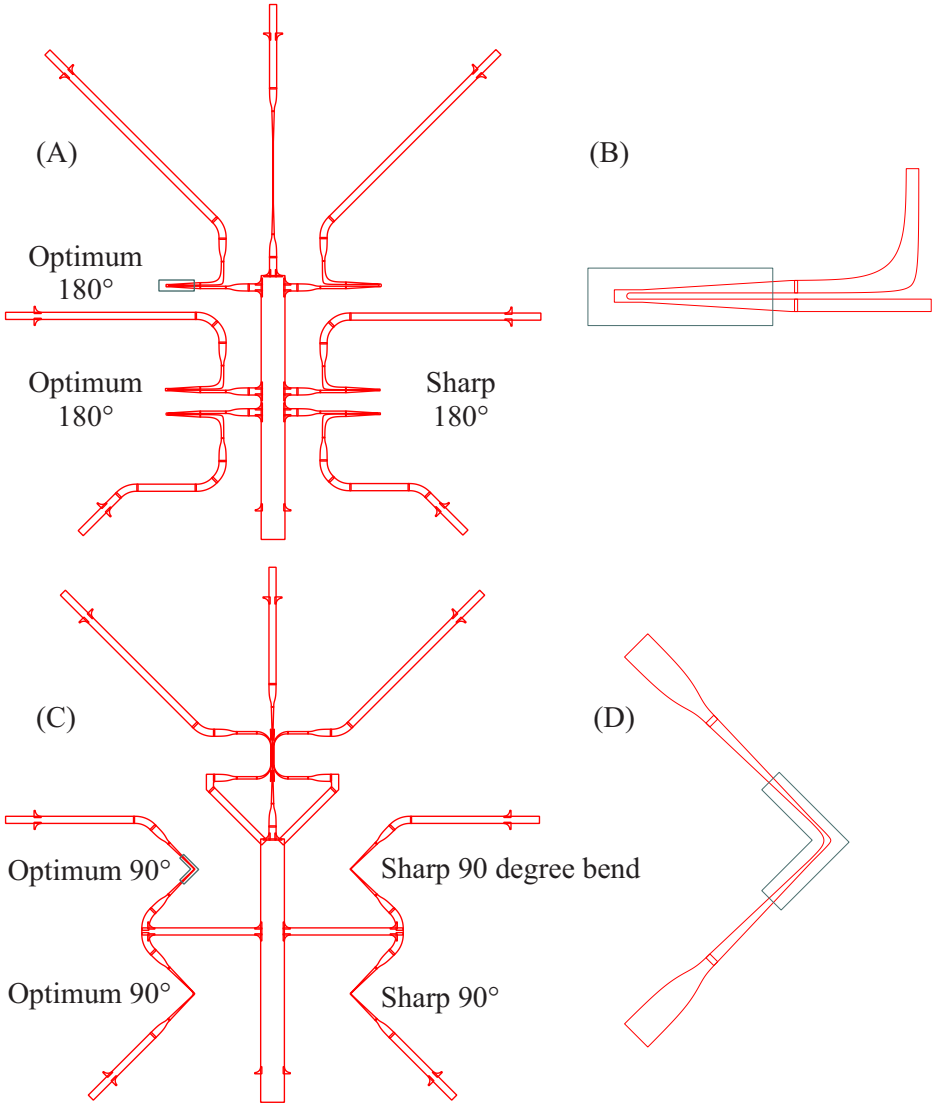

Figure 2.7: (A) and (C) Drawings of 8nm thick NbTiN sample containing 180-degree and 90-degree bends, respectively. (B) and (D) Magnified drawings of the green sections, depicting optimum designs of 180-degree and 90-degree bends.

photon sensitivity by checking the linear proportionally of the photon counts with the number of incident photons [40].

Figure 2.6(a) shows the result for a pair of 90-degree bends (d and b) (circles), and also a pair of 180-degree bends (g and f) (squares). The sharper bends are shown by filled symbols. The photo-response of the bends that make a pair is almost similar for their common range of bias. This is expected as the devices in a pair are identical except at the small bending area. However, at the same bias current, and therefore at the same quantum efficiency, utilizing an optimum bend can reduce the dark count rate by orders of magnitude, a significant result for SNSPDs. We also note that the optimum bends allow a device to be biased with a greater absolute current value, since the current density bottleneck in sharp bends is mitigated. This enables operation at higher quantum efficiency (or longer wavelength).

Dark count measurements for some of the nanowires fabricated on different chips (each symbol is for devices on the same chip) are illustrated in Fig. 2.6(b). Variations for critical current measurements of our optimum bends on different chips can be seen. However, on each chip the trend is the same: the sharper the bend the smaller the critical current, and the higher the dark counts.

At the inner edge of a sharp 90-degree turn with radius of curvature equal to ~ 35nm, we calculate the density of the sheet current, $|\mathbf{K}|$, ~ 1.7 times higher than the same density for an optimized bend (smallest possible footprint). So, a vortex at the edge of a sharp turn faces almost the same barrier as a vortex at the edge of an optimum bend but at a bias current ~ 1.7 times smaller (neglecting radius of curvature effects [36] which is reasonable because ~ 35nm is bigger than the coherence length). Therefore, assuming vortices overcoming an edge barrier is the origin of dark counts [41], we expect having the dark count vs bias current of a sharp turn to be approximately shifted to smaller currents by $\sim 1/1.7$. However, in none of our nanowires have we observed such a large shift. The trend of disagreement with this theory is nevertheless the same as what has been observed for critical current measurements on wider strips [37, 38]. The other possible explanation for the origin of dark counts: unbinding of vortex-antivortex pairs [41], needs further theoretical development before application to the bending area where the edges of the strip are not straight and the current distribution is not uniform. More details about

origins of dark count generation will be provided in the next chapter.

2.3 Concluding Remarks

To conclude, we have explored the possible adverse impact of sharp turns on SNSPDs through (i) limiting their bias current and thus limiting their quantum efficiency, and (ii) generating excess dark counts not generated by straight nanowire segments where photons are detected. We expect the utilization of optimally designed bends to further push SNSPDs to more efficient single-photon detection at longer wavelengths while generating less dark counts. This optimum design will be exploited in the later chapters to improve overall performance of the proposed detector.

Chapter 3

Origin of Dark Count Generation

In a single photon detection, even when the input terminal is fully blocked, randomly distributed signals (clicks) are still generated at the output electrical terminal of the detector. These output clicks, or dark counts, are of great importance not only because they affect the precision of input photon rate to output click rate conversion, but also due to their adverse effect on the maximum achievable critical current (known as experimental critical current) of the device. In short, the presence of dark counts dramatically degrades the overall performance of an SNSPD. In this chapter, the origins of dark count generation will be discussed in details. I will try to provide a clear picture of all the processes that lead to this dissipative transition of the initial metastable state of general superconducting nanostrips in the absence of an input signal. This study provides a better understanding on all aspects of the detection process, and also opens up new possibilities in using this class of detectors as a quantum level detector.

It is generally believed that there are two distinct processes leading to this dissipative transition, both involving vortex motion. The first, and usually the dominant mechanism, is the motion of spontaneously generated vortices accumulated at the edge of superconducting strips at high bias currents [42, 41]. These vortices are formed when the self-generated magnetic field at the edge of the strip is considerably greater than the lower critical field of the superconducting material and the width of the strip is also larger than the superconducting coherence length. The motion of these vortices at the direction normal to the

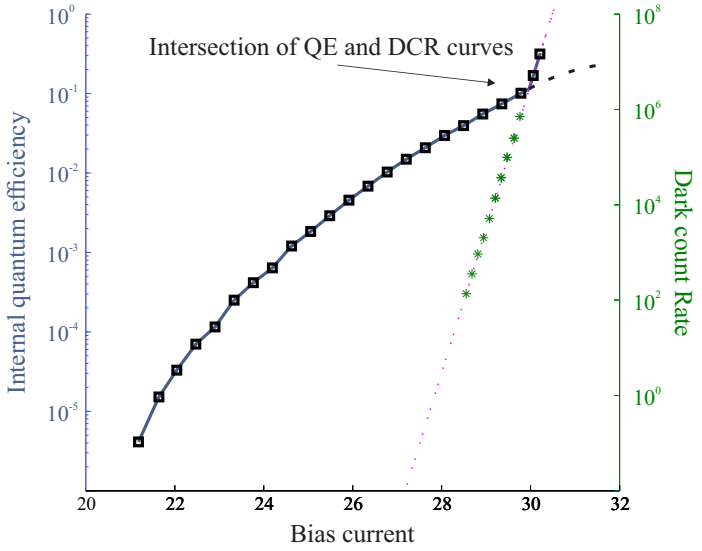

Figure 3.1: Internal quantum efficiency (blue curve) as well as dark count rate (green curve) of a 5nm thick NbTiN straight superconducting strip measured at 3.5K. For a normal width of a superconducting strip (100nm is used for this experiment), there would always be an intersection between these two curves. Since by nature (will be explained more later in this chapter), dark count generation has a power law dependence to the input driving current; therefore, the presence of these intrinsic fluctuations always puts an upper bound to the internal efficiency of the detector. By pushing the dark count curve to higher bias currents or eliminating their generation, one could reach the saturation limit of the detector (black dashed-line section) and thus operate the detector at its ideal detection mode.

current density causes the formation of a normal belt across the strip which usually leads to a normal state transition. The other source of fluctuation is attributed to the unbinding of the spontaneously nucleated vortex-antivortex pairs (VAPs) moving across the strip in opposite directions [43, 44]. Again, due to the same mechanism, a normal belt is formed. Interestingly, for the nucleation of VAPs there is no direct need for an external magnetic field as these pairs are topological excitations of the superconducting strip itself [45], but again the presence of the bias current is crucial for VAPs to overcome the potential barrier at the film edge.

Although the physics behind both fluctuation mechanisms has been widely studied in the past, there are still some ambiguities in the interpretation of the experimental observations. For instance, the fluctuation rates for wide samples decay faster than what is predicted by the thrmodynamical model proposed by Bartolf et. al. [42]. Also, the bias current dependence of the measured dark count rate across a wide temperature range, below the Berezinskii-Kosterlitz-Thouless (BKT) phase transition, does not fit well within neither the current-assisted VAP unbinding nor the thermally-excited vortex hopping model [46].

In this chapter, we present a new model for vortex and vortex-antivortex liberations in a superconducting nanowire. The model is built complimentary to the existing, well-established models by considering the effects of quantum confinement on vortex and antivortex initial energy states. It will be shown that on the length scale of the coherence length, the potential barrier at the edge of the superconducting strip is strongly confined such that the initial energy levels for both cases are affected by the size and shape of the current- and temperature-dependent potential barrier. In this limit, it is not sufficient to only consider the ground state in the classical thermodynamic calculations, but also the dissipative quantum tunneling of singularities may have a significant impact on the final fluctuation rates.

3.1 Modeling a Single Vortex in an Isolated Superconducting Strip

In reference [47], it has been shown that to quantitatively describe the motion of an isolated vortex in a single thin-film superconductor, it is useful to make use of the London [48] or Ginzburg-Landau [49] theory. The current density obeys the classical Maxwell's equations and is defined as,

$$\mathbf{g} = -n_{2\mathrm{D}}^{*} e^{*} \mathbf{v}_s \tag{3.1}$$

where $n_{2\mathrm{D}}^{*}$ is the sheet density of the superconducting pairs integrated over the film thickness and e^{*} is the pair charge which is equal to $2e$. Pair velocity is define from BCS theory as follows,

$$\mathbf{v}_s = \left(e^{*}/m^{*}c\right)\left[\mathbf{A} + \left(\Phi_0/2\pi\right)\boldsymbol{\nabla}\gamma\right] \tag{3.2}$$

Here m^{*} defines the pair mass, $\mathbf{A} = \boldsymbol{\nabla} \times \mathbf{B}$ is the vector potential. γ is the phase of superconducting order parameter in the London limit. Substituting equation (3.2) in equation (3.1), it is easy to show that the sheet current density can be written as,

$$\mathbf{g} = -\left(c/2\pi\Lambda\right)\left[\mathbf{A} + \left(\Phi_0/2\pi\right)\boldsymbol{\nabla}\gamma\right] \tag{3.3}$$

In equation (3.3), Λ symbol is used as the two-dimensional magnetic film screening length and is defined by,

$$\Lambda = m^{*}c^2/2\pi n_{2\mathrm{D}}^{*}\left(e^{*}\right)^2 \tag{3.4}$$

Consequently, as an alternative way, a thin-film superconducting strip can be considered as a bulk medium such that $n_{2\mathrm{D}}^{*} = n_{3\mathrm{D}}^{*} d$ and $\Lambda = \lambda^2/d$ where $\lambda = \sqrt{m^{*}c^2/4\pi n_{3\mathrm{D}}^{*}\left(e^{*}\right)^2}$ is the London penetration depth of a bulk superconducting medium.

When the thin superconducting film contains an isolated vortex with a quantum flux, $\Phi_0 = hc/2e$ located inside a superconducting layer far from the film edges, the Pearl solution is obtained in cylindrical coordinates (ρ, ϕ, z) from the general solution of the equation $\boldsymbol{\nabla} \times \mathbf{B} = 0$, where $\mathbf{B} = \boldsymbol{\nabla} \times \mathbf{A}$ and $\mathbf{A} = \hat{\mathbf{a}}_{\phi} A_{\phi}\left(\rho, z\right)$. Solving the Maxwell equation for magnetic field results in following current density distribution [47],

$$\mathbf{g}_{\phi}\left(\rho\right) = \left(c\phi_0/8\pi\Lambda^2\right)\left[H_1\left(\rho/\Lambda\right) - Y_1\left(\rho/\Lambda\right) - 2/\pi\right] \tag{3.5}$$

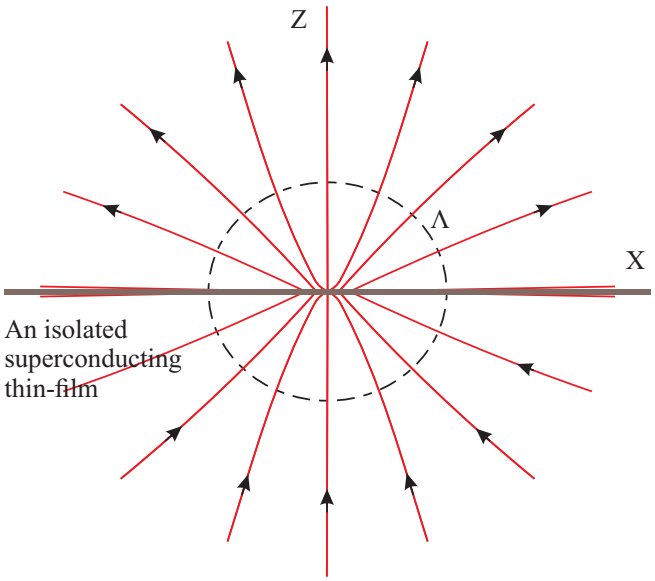

Figure 3.2: Magnetic field generated by a two-dimensional Peal vortex in an isolated superconducting thin-film [50]. The field distribution for $z > 0$ and $r > \Lambda$ resembles that of a magnetic monopole ($B = \phi_0/2\pi r^2$) [47].

where H_1 is the Struve function[1] and Y_1 is the second order Bessel function. Using this current distribution, magnetic field distribution of a single isolated vortex is sketched in Fig. 3.2.

Having the super-current distribution of the film, the self-energy of a vortex in a limiting conditions ($\rho \ll \Lambda$ and $\rho \gg \Lambda$) is simplified as,

$$U_0(\rho) = \left(\phi_0^2/4\pi^2\Lambda\right) \ln(\Lambda/\rho), \qquad \rho \ll \Lambda \tag{3.6}$$

$$U_0(\rho) = \phi_0^2/4\pi^2\rho, \qquad \rho \gg \Lambda \tag{3.7}$$

This potential energy is the work done by the repulsive Lorenz force ($\mathbf{g}(\rho) \times \phi_0/c$) to move a vortex of the same sign from infinity to position of ρ from the isolated vortex. The idea of having a vortex of the same sign at the distance of ρ is in fact the mathematical

[1] Struve function in power series form is $\sum_{m=0}^{\infty} \frac{(-1)^m}{\Gamma(m+\frac{3}{2})\Gamma(m+\alpha+\frac{3}{2})} \left(\frac{x}{2}\right)^{2m+\alpha+1}$

implementation of an infinite potential barrier at the entrance edge of the superconducting film such that the barrier acts as a mirror for the vortex[2].

3.2 Fluctuation Rate Modeling

Throughout this thesis, the structure of both singularities (vortex and VAP) are described by the Pearl model [50] introduced in the previous section. As usual, to study the dissipation rate in both quantum and thermal levels, the surface potential barrier i.e. Gibbs free energy barrier faced by each singularity is defined as the starting point.

For the case of vortex hopping, the surface barrier is dependent on the current distribution of the film in the presence of vortices. In the London framework, the supercurrent flow obeys [51]:

$$\boldsymbol{\nabla} \cdot \mathbf{g} = 0 \tag{3.8}$$

$$h_z + \frac{2\pi\Lambda}{c} \left(\boldsymbol{\nabla} \times \mathbf{g}\right) \cdot \hat{\mathbf{a}}_\mathbf{z} = \Phi_0 \delta \left(\mathbf{r} - \mathbf{r}_V\right), \tag{3.9}$$

where Λ is the Pearl penetration depth of the superconducting strip, $\mathbf{g}$ defines the surface current density, $\mathbf{r}_V$ points to the vortex location and Φ_0 is the quantum of magnetic flux passing through the superconductor. In this formulation, the effect of the vortex core is simplified to just a local phase perturbation of the order parameter. Also, it has been assumed that the vortex density is low enough, such that interaction between vortex pairs are negligible. The first term on the left-hand side of equation (3.9) introduces the screening of the magnetic field in the strip. In reference [36], it is shown that in a straight strip, the divergence of the supercurrent normal to the boundary is less than 0.02% for a typical width of a strip ($w \approx 100$nm) and hence the effect of the screening is negligible. Now by introducing a scalar stream function G such that $\mathbf{g} = \boldsymbol{\nabla} \times G\hat{\mathbf{e}}_\mathbf{n}$, the current distribution is simplified in the form of a Poisson equation [52]:

$$\Delta G = -\frac{c\Phi_0}{2\pi\Lambda}\delta(\mathbf{r} - \mathbf{r}_V). \tag{3.10}$$

[2]similar to the electromagnetic image theory

Finally, the self-energy of a single vortex in the strip with a uniform current flow is given by:

$$\epsilon(\mathbf{r}_V) = \frac{\Phi_0}{2c} G(\mathbf{r} \to \mathbf{r}_V). \tag{3.11}$$

This is, indeed, the surface barrier when there is a negligible current flow across the strip. In the presence of a bias current, there is an additional term due to the Lorantz force, $\mathbf{g}(\mathbf{r}_V) \times \Phi_0/c$, between the vortex and the external supercurrent. Combining these two terms, the final potential barrier reads:

$$\begin{aligned} \epsilon_V(x_V) &= \epsilon_0(T, I_b) \times \ln\left(\frac{2W}{\pi\xi(T)} \sin\left(\frac{\pi x_V}{W}\right)\right) \\ &\quad - |\mathbf{g}_{\text{ext}}|\, x_V \Phi_0/c, \end{aligned} \tag{3.12}$$

where x_V is the normal distance between the position of the vortex and the entrance edge of the film. W is the film width and $\epsilon_0(T, I_b) = \Phi_0^2/8\pi^2\Lambda(T, I_b)$ defines the characteristic vortex energy in a thin superconducting strip.

For the case of VAP, the surface energy barrier depends on the initial position of the spontaneous nucleation. It can be shown that the minimal increase in the Gibbs free energy occurs only if the nucleation takes place in the middle of the strip [53]. Under this condition, the energy barrier as a function of the pair separation (b) reads,

$$\begin{aligned} \epsilon_{\text{VAP}}(b) &= 2\epsilon_0(T, I_b) \times \ln\left(\frac{W}{\pi\xi(T)} \sin\left(\frac{\pi b}{W}\right)\right) \\ &\quad - |\mathbf{g}_{\text{ext}}|\, b\Phi_0/c. \end{aligned} \tag{3.13}$$

Regardless of the nature of these decay rates, the thermal activation in the limit of weak damping obeys the classical Kramers formula, which concludes the following rates for equation (3.12) and equation (3.13), respectively:

$$R_V = \alpha_{\text{v}} \frac{I_b}{I_c(T)} \times \exp\left(-\frac{\epsilon_{\text{v,m}}}{k_B T}\right) \tag{3.14}$$

$$R_{\text{VAP}} = \alpha_{\text{VAP}} \times \exp\left(-\frac{\epsilon_{\text{VAP,m}}}{k_B T}\right). \tag{3.15}$$

Here m refers to the maximum point of the potential barrier and α_V and α_{VAP} are the attempt frequencies. In the case of vortex hopping, the prefactor is also proportional to

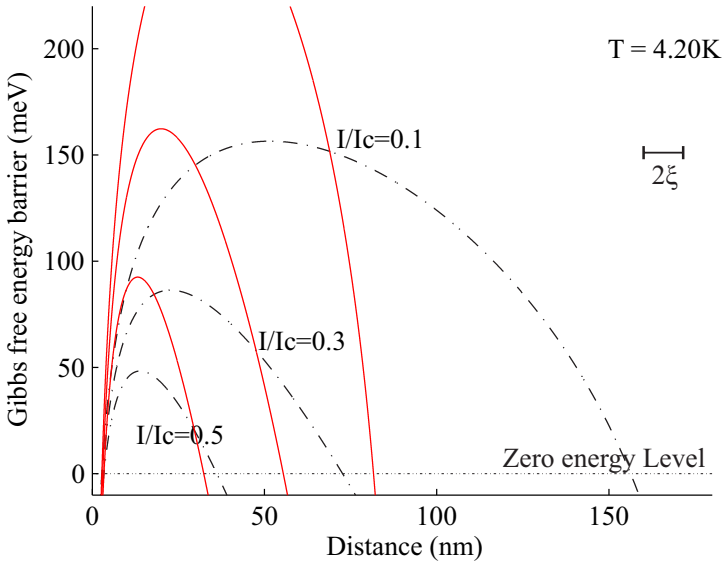

Figure 3.3: Gibbs free energy barrier as a function of distance for vortex hopping model (black dash-dot lines) as well as vortex-antivortex pairing model (red solid lines). All the curves are plotted for a NbTiN strip with 180nm width and 8nm thickness. Critical temperature of 8.50K (experimental critical temperature of the wires) and the coherence length of $\xi(I_b = 0, T = 0) = 4.7$nm at zero temperature were used for these calculations. In the derivation of equations (3.12) and (3.13), the current and temperature dependent coherence length and penetration depth have been employed (see equation (5) and (14) of ref. [42]).

the number of available vortices penetrating the film and hence it is proportional to the driving current.

The thermal fluctuation rates are the dominant processes only when the thermal activation energy is on the order of the barrier height. At sufficiently low temperatures, these sources of dissipation gradually freeze out, opening a new possibility for quantum based tunneling [54]. In this scenario, vortices tunnel through the surface barrier either with or without dissipation. In the current context, the dissipative fluctuation rates are of interest. In the limit of strong dissipation, the tunneling rate reads [55]:

$$R_{\mathrm{Q}} = \alpha_{\mathrm{Q}} \frac{I_b}{I_c(T)} \times \exp\left(-\beta_B \frac{\pi \hbar x_B^2}{2e^2 R_N \xi^2(T)}\right) \tag{3.16}$$

where R_N is the normal sheet resistance of the superconducting film, β_B relates to the surface barrier shape and is on the order of one, and x_B is the barrier width at the ground energy level and can be calculated from equation (3.12). Similarly in this model, the attempt rate is proportional to the driving current with the same physical origin. It is interesting to mention that unlike the previous thermal models, here the rate is related to the Gibbs free energy through the barrier width rather than the barrier height.

3.3 Ground State Consideration

As a starting point, we refer to the experimental results of ref. [42]. In section III of this paper, the measured fluctuation rates for wide wires decay faster than what is expected by the power law dependence which cannot be explained within the formalism of either thermal models, i.e. Vortex hopping or VAP unbinding. Interestingly, the deviation is only observed at very low count rates (less than about 100Hz) where the bias current is noticeably smaller than the experimental critical current of the device.

To explain this abnormal behavior, we highlight that to stay in the London limit, the finite size of the vortex core has been neglected in the derivation of equations (3.12) and (3.13). This implies the real potential barrier deviates from the theoretical predictions at the edges of the strip. The impact of this simplification is more pronounced by examining

the behavior of the Gibbs free energy barrier and it's divergence at the film boundaries. Consequently, a more sophisticated approach, such as the direct solution of the Ginzburg-Landau equation, is required to predict the barrier shape around the edges [56]. However, in the majority of the previous works [42, 41, 57, 58], to simplify the calculations, a standard cutoff is defined for the vortex location at the boundaries and the initial energy level is arbitrary set to zero. Although this assumption gives an acceptable qualitative picture for the vortex liberation, when it comes to explaining the temperature or width dependence without adding a set of free parameters, the models do not accurately justify experimental observations. Here, a current-dependent energy level is suggested for the initial states. We [59] claim that this assumption has a major impact on explaining the behavior of the fluctuation rates in both quantum or thermal regimes.

Figure 3.3 depicts the Gibbs free energy of the vortex hopping and VAP unbinding models as a function of vortex location and vortex-antivortex separation, respectively, for different bias currents. From this figure, it is clear that the vortex freedom at zero energy level in both models is on the order of the superconducting coherence length. Now the question is what happens if this confinement is also comparable to the de-Broglie wavelength of the vortices. In this limit, the quantum-mechanical effects such as energy discretization and quantum tunneling are significant. To measure the importance of quantum phenomena at the vicinity of the strip edge, the potential well is approximated as a harmonic potential. If the frequency of the oscillation, $\omega = \sqrt{k/M^*}$, is in the range of the superconductor's natural frequency, $\Delta/\hbar$, then the lowest achievable energy level is not equal to the minimum of the potential well anymore, meaning that in the thermal activation calculations, the barrier height is lower than that of the classical model. Furthermore, the quantum tunneling barrier would be also smaller than what has been predicted by the classical model. In the context of the current model, although there is no intrinsic mass defined for a vortex, an effective mass (inertial mass, M^*) can be associated with the vortex motion [60, 61, 62, 63].

For a Nb film at a temperature close to the critical temperature, an order-of-magnitude estimate on the inertial mass varies from $M^* \simeq 10^{-2}m^*$ per length at the dirty limit [64] to $M^* \simeq 10^4 m^*$ per length at the superclean limit [65]. In order to circumvent the problem associated with the uncertainty in the mass of a vortex, the quantum mechanical

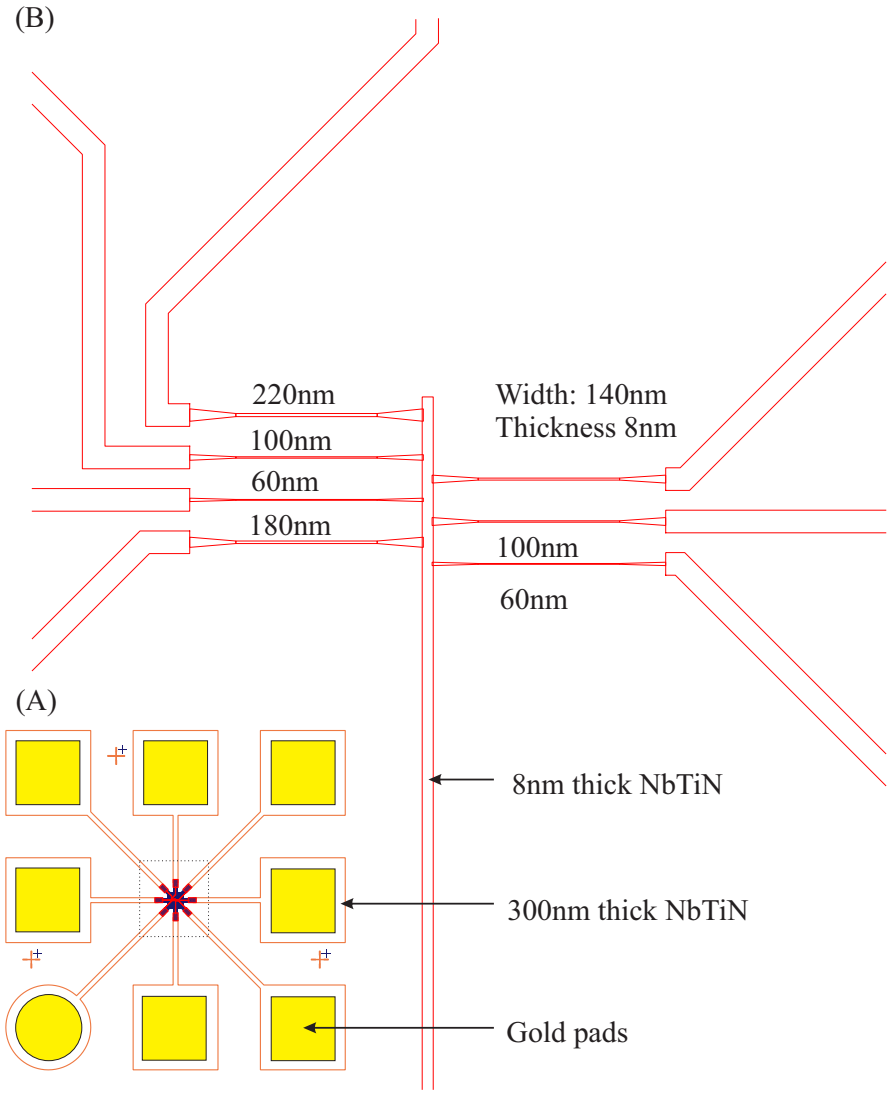

Figure 3.4: (A) Drawing of the actual device containing the nanowires of varying thicknesses. The gold pads are colored in yellow and are deposited for the purpose of wire-bonding. The actual 8nm NbTiN (dotted area) is connected to the Gold pads through 300nm thick NbTiN layer. (B) Magnified drawing of the dotted area. All the straight nanowires are 20 μm in length and are connected to four times wider wires with width to length ratio of 1/10 to prevent current crowding at the sharp edges.

property of harmonic oscillators is used as an approximate model for the dynamics of a trapped vortex at the edge of a superconducting wire. The kinetic energy and the potential energy of a trapped vortex are related by $E_{K_{\max}} = E_{P_{\max}}$, where $E_{K_{\max}} = \frac{1}{2}M^* v_F^2$ [62] and $E_{P_{\max}} \approx \frac{1}{2}k\xi^2$, where k is the force constant. For such a system, the minimum quantum energy is $\hbar\omega/2 \approx \hbar v_F/2\xi \approx \Delta(I,T)$. This suggests that the initial energy of the vortex at the edge, due to the local confinement, is a current and temperature dependent value and cannot, arbitrarily, be set to zero. In the London's framework this phenomenon can also be explained: vortices are dynamical objects with finite extensions about the size of the superconducting coherence length; therefore, they cannot be localized in a confining potential less than the coherence length. This minimum length of the potential determines the initial energy of a vortex.

3.4 Experimental Verifications

Figures 3.6 and 3.5 illustrate the experimental decay rates of 20μm long straight nanowires at different temperatures and widths. All the strips are made of 8nm thick NbTiN films deposited on oxidized silicon [21]. To measure the fluctuation rates, the samples have been installed in a dipstick probe immersed in liquid Helium. To ensure low noise operation which is required to measure the very low level fluctuation rates (less than 100Hz), a custom-made remotely controlled voltage source and pulse-counter have been employed.

As shown in Fig. 3.5b, at high bias currents, there is a power law dependence between the decay rates and the bias current as predicted by the log dependence of the rate models. But interestingly when the bias current is reduced, a deviation from the standard model is observed especially for wide wires.

Another abnormal observation is on the dark count curves of a single wire measured at different temperatures (see Fig. 3.6). To describe the dark count generation of the wire at a fixed temperature, one can fit the experimental data to equation (3.14) by defining an attempt frequency, α_V. The rest of the curves are produced according to the rate equation without adding new free-parameters to the model. From this figure, it is seen that in the thermally excited vortex hopping model with zero initial energy level, the curves

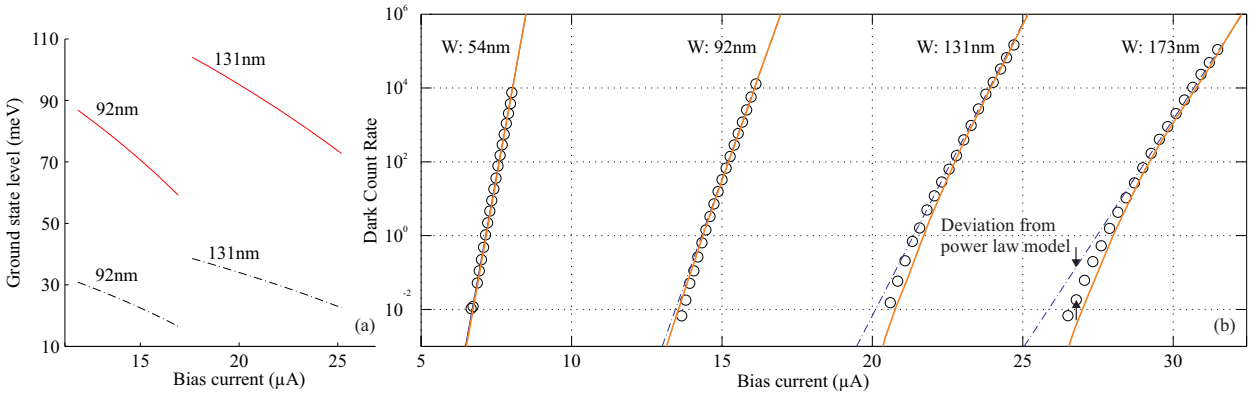

Figure 3.5: a) Ground state energy level prediction for vortex hoping model (black dash-dot lines) as well as VAP unbinding model (red solid lines) for different film widths. b) Dark count rate versus bias current for NbTiN strips with different widths (measured from high resolution SEM images). Orange solid lines, blue dash-dot lines and empty circle lines represent theoretical calculation of the ground state model, power law fitting and the experimental results, respectively. For the theoretical calculations, the total rate of the vortex hopping (equation (3.14)) and VAP unbinding (equation (3.15)) models with equal prefactors ($\alpha_{\rm v} = \alpha_{\rm VAP}$) is used. Note that at the operation temperature (4.2K) the quantum tunneling rate (equation (3.16)) is several orders of magnitude smaller than the thermal activation counterparts and hence it has been neglected. To fit the ground state model to the experimental data, the uncertainty in vortex location at the ground state level is set to $\Delta(x) = 1.3\xi(I_b, T)$.

at the lower temperatures deviate from the experimental data. To explain the origin of these abnormal behaviors, the theoretical prediction of the current dependent ground state levels are calculated and the results are plotted in Figs. 3.5a and 3.6. According to these calculations when a wire is wider, based on the Heisenberg uncertainly, the ground state is located in a higher energy level in comparison to narrow wires which is in accordance to the higher confinement of the potential barrier for the wider wire. Also the slopes are slower which suggests lower current dependence of the decay rate. Consequently, higher deviation is expected for wider wires. In other words, when the wires are wider, the London approximation for the potential shape at the edges of the film is less accurate and hence zero level approximation also results in a more inaccurate estimation. Although when the current approaches the experimental critical current of the structure, the coherence length is large enough to compensate the effect of the ground state (see Fig. 3.3). This is the reason why the deviation is only observed at low bias currents.

According to the quantum ground state model, when the barrier is more confined, the ground state level is placed at a higher energy level. This naturally implies higher energy levels for the case of the VAP unbinding potential in comparison to the vortex hopping potential (see Fig. 3.5a). Consequently, the corresponding barrier for vortex-antivortex pairing is not anymore twice as high as for the single vortex hopping model in the normal operation temperature (4.2K) as suggested by zero energy level model. For equal prefactors ($\alpha_{\mathrm{v}} = \alpha_{\mathrm{VAP}}$), vortex hopping is the only dominant mechanism for wide wires ($w > 100$nm). For narrow wires, the rate depends on the temperature and width of the strip but since the barriers are on the same order, neither source of dissipation can be neglected (see Fig. 3.7). Likewise, for lower temperature, the effect of quantum tunneling (equation (3.16)) would be more significant as the barrier width is much narrower than the prediction of the zero ground state level. Using the quantum ground state model, for a NbN film of width 100nm, it is possible to show that for temperatures lower than 2K, the effect of quantum tunneling is considerable. For a temperature of about $T = 0.5$K, the dissipative quantum tunneling would be the dominant process which explains the approximately equal rate observed for the two lowest curves of figure 2 of reference [46].

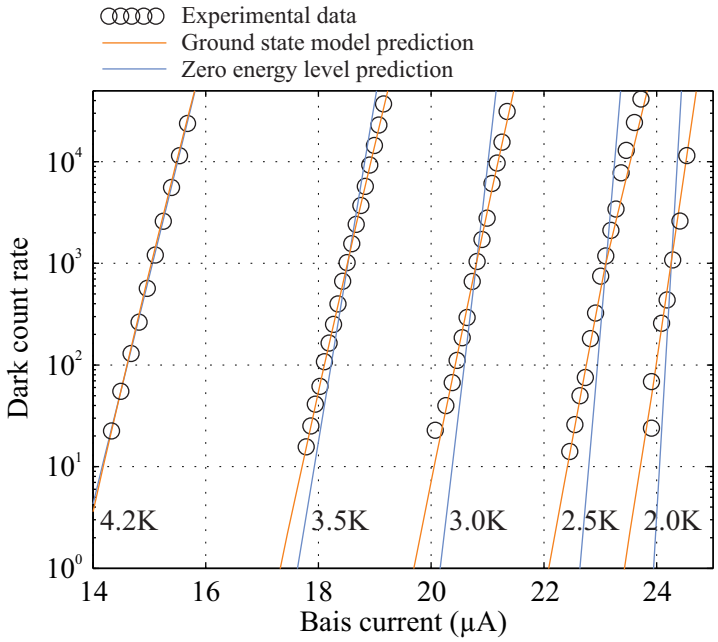

Figure 3.6: Dark count rate versus bias current at different temperatures for a 92.0nm width NbTiN superconducting strip. The orange line is the quantum ground state model prediction and the blue line is the zero ground state model predition. In both models, only the first left curve is fit to the experimental data at $T = 4.2$K.

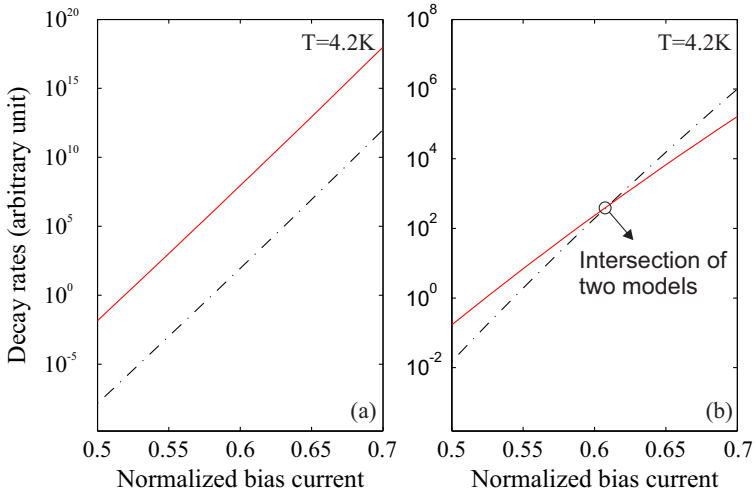

Figure 3.7: Vortex hopping rate (black dash-dot lines) compared to VAP unbinding rate (red solid lines) for different bias currents at $T = 4.2$K for a strip of 82nm width. The superconducting parameters are the same as the ones used in Fig. 3.3. The left figure (a) depicts the classical model where the energy barrier is calculated from zero energy level while in the right figure (b), the ground state level is calculated based on the quatum well confinements. These calculations suggest that in contrary to the classical model, both of the rate models (Vortex hopping and VAP unbinding) may be the dominant origin of the dark count generation if the confinement is taken into account.

3.5 Concluding Remarks

It has been both theoretically and experimentally shown that to determine either the thermal activation or quantum tunneling liberation rate, a precise estimate for the shape of the Gibbs free energy barrier at the film edge or at the location of VAP nucleation is crucial. Using the London approximation for the barrier shape results in an inaccurate current distribution which leads to an inaccurate barrier height or width estimations. However, using quantum mechanical approach it is possible to define a current-controlled initial energy level for both singularities based on their inertial mass and the barrier confinement. It has been shown that the consequent calculations result in a more accurate prediction for the rate equations. The quantum treatment of the decay rate also revealed that both the VAP unbinding and dissipative quantum tunneling models may have higher rates than those predicted by the classical zero level energy models which suggests higher contribution of these sources of dissipation in the final rate.

Chapter 4

Plasmonic Superconducting Nanowire Single-photon Detector

Despite all the promising properties of SNSPDs, low system quantum efficiency remains one of the major obstacles in this class of detectors [7, 66, 28]. This is mainly due to the input optical wave readily passing through a normal-incidence meander-line structure as a result of the great difference between the thickness of the film and skin depth of the optical wave [32]. In this chapter, we present a novel single-photon detection structure to address this issue without increasing the length or the thickness of the active element such that two seemingly contradictory properties, high speed operation (requiring small active area) and high photon absorption probability (requiring large active area), can be maintained simultaneously. The design is based on the plasmonic nature of a superconducting layer [34] to improve the photon absorption process by exciting the surface plasmon polaritons, SPPs, at the interface of the superconducting layer and a positive index dielectric layer [35]. The general idea is to deposit and pattern thin-film superconducting wires on top of a dielectric slab waveguide. Similar structures based on dielectric slab waveguides have been previously reported, where the optical energy is mostly confined at the center of the high index dielectric layer [11, 67]. Consequently, there is a small overlap of the optical field with the active element, and only a small portion of the available power is absorbed. In our plasmonic design however, the presence of a negative index superconducting layer

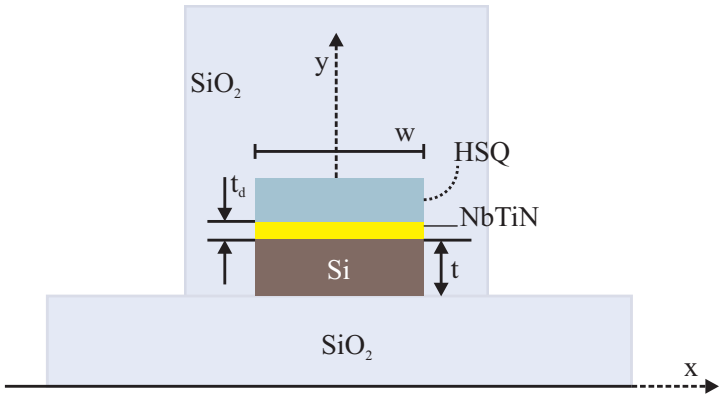

Figure 4.1: Layered structure of the proposed detector. Superconducting layer (nanowires) with thickness t_d is placed on top of a Si layer of thickness t and width w in an environment of HSQ/SiO_2 cladding layers. The HSQ layer is used during patterning of the wires and can be kept as a protective layer.

leads to an additional confinement resulting in sub-wavelength mode formations.

Excitation of SSPs in a thin superconducting layer (normally less than 12nm) is the main challenge of this work. To observe well-defined plasmonic confinement, there is a minimum feature size for the width of both the dielectric waveguide and the superconducting layer. This imposes an undesired limitation on the nanowire from a detection perspective, particularly on single-photon sensitivity, since there is an upper bound for the cross section area of the active element. In general, we will show that there is a trade-off between the probability of photon absorption and the internal quantum efficiency of the device. We present an alternative to decouple these two properties based on the optical design and photon detection mechanisms in SNSPDs (current concentration beyond the depairing current density at the sidewalks upon photon absorption [29, 68] and vortex hopping from one edge across the strip or vortex-antivortex unpinning [69, 42]).

This chapter is organized as follows. In section 4.1, the complex conductivity of a superconducting material in optical frequency range is discussed. Section 4.2 describes the possibility of plasmonic excitation of a thin-film superconductor. In spite of the extremely thin thickness of the superconducting layer in comparison to the other layers, still excitation of the fundamental plasmonic mode is possible with proper design of the thickness and

width of all layers. In section 4.3, all different possible excitation mechanisms of the proposed structure are briefly reviewed. The pros and cons of each model are also discussed in details. In Section 4.4, the nonequilibrium to equilibrium relaxation dynamics of the order parameter in a superconducting film after absorption of a single-photon is studied. The objective is to find the optimum size of each layer such that the structure can benefit from both photon detection mechanisms mentioned above.

4.1 Complex Conductivity of a Superconductor

In this section, I will deal with complex conductivity of a superconducting sheet in the presence of an electromagnetic field. It is known that the ideal DC properties of a superconductor are governed by the flow of lossless super-current within an equilibrium state of the system. In this state, a superconductor can be approximated as a perfect conductor which also exhibits perfect diamagnetism. This lossless behavior starts to disappear as the frequency of electromagnetic field increases. This is because of the dissipation introduced in the system since now normal electrons are also contributing in the conduction. In order to calculate the conductivity at this frequency range, the BCS theory of superconductivity comes in handy. In 1991, Zimmermann used this theory and introduced an explicit expression to describe macroscopic conductivity of a homogeneous superconductor with an arbitrary purity. The detail derivation can be found in ref [70]. Here, we only summarize those physical behavior predicted by this model.

A bulk superconductor shows a residual real conductivity for frequencies less than the gap frequency provided that number of Cooper pairs exceeds the number of normally excited quasiparticles (approximately $T < 0.5T_C$). If there is no power consideration when frequency is about the critical value, $E \simeq 2\Delta$, a sudden increase of loss happens. The reason for this is that an individual quantum of electromagnetic radiation is powerful enough to break down a pair and form two excited quasiparticles. If frequency further increases, each photon can break down several quasiparticles; hence the contribution of excited QPs in conductivity would be dominant. In fact, pairs cannot contribute anymore in conduction unless they are first broken down to excited quasiparticles. As a consequence,

the superconducting gap becomes smaller and material tends to behave like a normal metal. Although this complex model gives an accurate description of microwave behavior of a superconductor[1], for higher frequencies, it approaches to the more intuitive model introduced by Mattis and Bardeen [73, 74],

$$\frac{\sigma_1}{\sigma_n} = \frac{2}{\hbar\omega}\int_{\Delta}^{\infty}\left[f\left(E\right) - f\left(E+\hbar\omega\right)\right]g\left(E\right)\,\mathrm{d}E \tag{4.1}$$
$$+\frac{1}{\hbar\omega}\int_{\Delta-\hbar\omega}^{-\Delta}\left[1-2f\left(E+\hbar\omega\right)\right]g\left(E\right)\,\mathrm{d}E$$
$$\frac{\sigma_2}{\sigma_n}|_{\hbar\omega<2\Delta} = \frac{1}{\hbar\omega}\int_{\Delta-\hbar\omega}^{\Delta}\left[1-2f\left(E+\hbar\omega\right)\right]g\left(E\right)\,\mathrm{d}E \tag{4.2}$$
$$\frac{\sigma_2}{\sigma_n}|_{\hbar\omega>2\Delta} = \frac{1}{\hbar\omega}\int_{-\Delta}^{\Delta}\left[1-2f\left(E+\hbar\omega\right)\right]g\left(E\right)\,\mathrm{d}E$$

here σ_n is the normal state conductivity, and $f\left(E\right)$ and $g\left(E\right)$[2] are Fermi function and coherent factor in the BCS theory, respectively:

$$f\left(E\right) = \frac{1}{1+\exp\left(\frac{E}{k_BT}\right)} \tag{4.3}$$

$$g\left(E\right) = \frac{1}{\left(E^2-\Delta^2\right)^{1/2}\left(\left(E+\hbar\omega\right)^2-\Delta^2\right)^{1/2}}\left(E^2+\Delta^2+\hbar\omega E\right) \tag{4.4}$$

Note that these two models coincide for all frequencies if an extreme limit where the coherence length (ξ) is large compared with the penetration depth λ is considered [3].

The first term in equation (4.2) is due to the contribution of thermally excited normal quasi-particles (n_n^0) with density approximated by the Gorter-Casimir expression, $n_n^0/n = \left(T/T_c\right)^4$ [75]. This term exist only if temperature is not equal to zero where carriers are a mixture of pairs and QPs. The second term is the contribution resulting from breaking

[1] BCS superconductor (weak coupling) with spherical Fermi surface; for those with nodes in energy gap refer to [71] and for strong coupling refer to [72].

[2] Signs of the square roots are such that $g\left(E\right)$ is positive in all integrals

[3] In general, the purity of a superconductor is characterized by the ratio of electron mean free path (l) over the coherence length (ξ_0). A sample is clean if this ratio is much greater than one. Otherwise, sample is considered as dirty. In most cases, clean superconductor corresponds to type I superconductor.

of the pairs by an external field which is zero unless photons have enough energy, i.e. $\hbar\omega > 2\Delta$. As a result, intrinsic loss vanishes if frequency is less than gap frequency and temperature is much lower than the critical value.

In superconductors, apart from the frequency dependency behavior introduced in equations (4.2) and (4.3), there is another important source of dispersion that arises from σ_n term. This dispersion can be calculated from classical model and is known as Drude model of conductivity:

$$\varepsilon_r(\omega) = n^2(\omega) = 1 - \frac{Ne^2}{m\varepsilon_0(\omega^2 - i\gamma\omega)} = 1 - \frac{\omega_p^2}{\omega^2 - i\gamma\omega} \tag{4.5}$$
$$\sigma_n(\omega) = \frac{\sigma_0}{1 - i\omega\tau}|_{\sigma_0=\omega_p^2\tau\varepsilon_0}$$

here, ω_0 is natural resonance frequency of the atomic system[4] and ω_p is the plasma frequency. Although this model gives an acceptable accuracy for low frequencies, the validity of it breaks for ω close to the plasma frequency[5]. This inadequacy can be fixed by applying these modifications:

1. Replacing the dielectric constant at very high frequencies, $\omega \gg \omega_p$, by ε_∞. This is due to a residual polarization of highly bounded electrons [76];

2. Adding a linear superposition of Lorentz-oscillator terms due to interaction of electrons with different phonon branches with different oscillator strengths[70];

3. Adding a Lorentz oscillator term as a result of electron absorption caused by interband transitions [70].

Thus, optical conductivity can be expressed as:

$$\varepsilon(\omega) = \varepsilon_\infty + i\frac{\sigma(\omega)}{\varepsilon_0\omega} + \text{Interband term} + \sum_{j=1}^{N} \frac{S_j\omega_j^2}{\omega_j^2 - \omega^2 - i\omega\gamma_j} \tag{4.6}$$

[4]Information about this quantity needs quantum mechanics treatment.

[5]For instance in case of gold, the model is only valid for energies below 3.8 eV

where, $\sigma(\omega)$ is the contribution of conduction electrons. For normal conductor this term is well described by a Drude model.

It is known that an ideal superconductor at zero temperature cannot absorb optical radiations with frequencies smaller than $2\Delta/\hbar$. For optical beams with higher energies, each absorbed photon breaks up a superconducting pair, creating two excited quasiparticles. The dynamics of the relaxation process back to the equilibrium state will be discussed later in the next section. For now, the main focus is on the optical conductivity of the superconducting sheet. In the framework of linear response to the electromagnetic field, optical conductivity can be calculated from Kubo formula [73] or equivalently, the superconductor can be treated as a bulk semiconductor medium with a band gap of around its Fermi energy. Using the latter model, the conductivity and hence absorption can be driven from Fermi golden rule assuming that transition probabilities for both quasiparticle scattering and new pair generation processes are known. These two transition probabilities are related to coefficient of matrix elements of interaction Hamiltonian [51]. In the normal state, all the matrix elements are independent from each other, and thus the transition probability of each particle can be easily described as the square of the corresponding matrix element. In superconducting state however, there are two matrix elements in the interaction Hamiltonian which relate two initial phase coherent states to final states with equal momentum and spin differences. Thus, for superconducting case, as long as the initial and final states remain coherent, to find the transition probability, prior to squaring, both elements must be added up. This coherency makes the transition probability of a superconductor different from that of the normal state. To solve this disparity, Bogoliubov-Valatin transformations come very handy. Using these transformations, the transition probability can be rewritten in form of normal state transition just by introducing a coherence factor. For case of optical absorption where external perturbation is in the form of $\mathbf{p} \cdot \mathbf{A}$, the coherence factor is defined as $\frac{1}{2}\left(1 - \frac{\Delta^2}{E\acute{E}}\right)$ where E and $\acute{E}$ are initial and final states. This equation suggests that superconducting phase-coherence only plays an important role in optical conduction whenever transitions with energy differences comparable to the energy gap are involved. Note that in the case of infrared detectors, to have high photon sensitivity, the wire is always biased very close to the critical current and hence the actual energy gap is very small. In fact, from physical point of view, optical conductivity of a

gapless superconductor or a superconductor with very small energy gap must be considered for optical calculations. This concludes a very small deviation in optical conductivity in comparison to the normal state conductivity should be expected for nanowires. This led us to employ the low temperature normal state conductivity for our optical calculations.

4.2 Plasmonic Guiding

This section presents the theoretical investigation on the possibility of SPP formation at the interface of an ultrathin superconducting film with a positive index dielectric medium. Figure 4.1 illustrates the layered structure of the device. All materials are selected such that the device is compatible with silicon photonics processing. For the superconducting layer, NbTiN is selected for the possibility of thin-film deposition as well as its low sensitivity to latching in the single-photon detection regime [77, 30]. From an optical perspective, the high index dielectric layer placed underneath the superconducting layer will serve as a guiding (core) layer. In the absence of the superconducting layer, the significant difference in the indices of this layer with the surrounding dielectric (cladding) layers permits strong lateral confinement of light on the order of the core dimension. Presence of the superconducting layer alters the lateral power distribution from center of the waveguide towards the superconducting interface and hence can improve the probability of optical absorption. The idea of optical confinement through plasmonic excitation arises from the fact that a superconducting film behaves like a negative index medium in the optical bandwidth [34]. Thus, by having proper dimensions in both transverse and lateral directions in all layers, it is possible to trap optical waves along the interface of these two layers.

Before we start this section, it is necessary to consider the usefulness of the classical optics for design of a quantum level detector. It is known that, in systems that are sensitive to single-photons, classical optics cannot be exploited to thoroughly describe the properties of light beams, and hence quantum mechanical formalism is used instead. In this regime, depending on the experimental setup, photons may behave like particles or wave with the energy and momentum of $E = \hbar\omega$ and $\mathbf{P} = \hbar\mathbf{k}$ where ω denotes the angular frequency

and $\mathbf{k}$ denotes the wavevector of the photon[6]. Furthermore, from similarity by mechanical harmonic oscillator in this regime, magnetic potential field operator is described as follows:

$$\mathbf{A}(\mathbf{r},t)=\sum_{k,\lambda}\varepsilon(\omega_k)_0\left[\hat{a}_{k,\lambda}(t)\,\mathbf{u}_k(\mathbf{r})+\hat{a}^{\dagger}_{k,\lambda}(t)\,\mathbf{u}^{*}_k(\mathbf{r})\right] \tag{4.7}$$

where

$$\varepsilon(\omega_k)_0=\sqrt{\frac{\hbar}{2\varepsilon_0\omega_k}} \tag{4.8}$$

$$\left[\hat{a},\hat{a}^{\dagger}\right]=1 \tag{4.9}$$

$$\frac{d}{dt}\hat{a}=\frac{i}{\hbar}\left[\hat{H},\hat{a}\right]=-i\omega\hat{a} \tag{4.10}$$

here, $\varepsilon(\omega_k)_0$ represents the magnetic potential field per photon per wavelength and $u(\mathbf{r})$ is the spatial field profile that can be found from Helmholtz equation. It is important to stress that according to the equation (4.7), quantization only occurs for the time and energy part, and accordingly, the spatial pattern of electromagnetic field is still governed by traditional Maxwell equations. This doesn't imply that the detection of a single-photon produces a spatial pattern of $|u(\mathbf{r})|^2$, instead in comparison to quantum mechanics, $|u(\mathbf{r})|^2$ gives the relative probability distribution for finding a photon in location $\mathbf{r}$. Thus, according to this argument, to design a single-photon detector with a high probability of detection, we still have to exploit to classical optics to increase the $|u(\mathbf{r})|^2$ term as much as possible in the nanowire section.

4.2.1 Dispersion Equation at Interface of a Superconductor and a Dielectric Medium

To drive the dispersion relation of our complex structure 4.1, on our first attempt, dispersion relation of a simplified model illustrated in Fig. 4.2 is explored. According to the discussion made in the previous section, most of the metallic superconductors behave like

[6]The expectation value of the field operators for true single photon Fock state is the same as classical optics and have probability interpretation.

a normal metal in the optical bandwidth and thus, they support a negative refractive index. Accordingly, if a semi-infinite superconducting sheet is connected to a normal positive index medium, the formation of surface waves are predicted by the plasmonic theory of optical guiding [34].

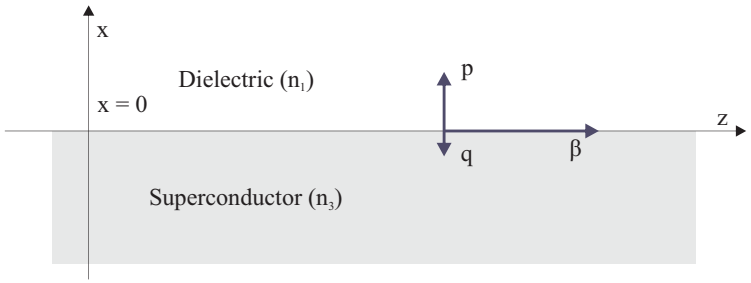

Figure 4.2: Two semi-infinite media separated by a planar interface at $z = 0$

From physical point of view, this wave is a quasi-two-dimensional electromagnetic wave coupled to the *surface* quasi-particle (polaritons) charge density. Therefore, similar to a traditional metal-insulator (MI) structure, the wave inherently tends to be confined near the superconductor surface where two-dimensional electron gas can form. Note that according to the argument made in section 4.1, in telecom bandwidth, due the energy consideration, superconducting pairs cannot directly contribute in the conduction unless they are first broken down to the excited particles.

Here, instead of solving Maxwell equations from scratch at each continuous region and applying boundary conditions to drive the dispersion equation, the interface is treated as a special case of a slab waveguide with zero core thickness. Consequently, dielectric waveguide mode conditions can be employed to drive the dispersion relation.

According to theory of optical guiding, existence of a TE mode with zero thickness requires that the sum of normal wave vectors at dielectric ($\mathbf{p}$) and metallic ($\mathbf{q}$) sections be equal to zero which is not possible as both of these normal wave vectors are positive for a *confined* mode. This implies that no surface plasmon polariton can exist for TE polarization in this special configuration. For TM polarization the same condition is valid if $\mathbf{p}$ and $\mathbf{q}$ are replaced by $\mathbf{p}_{\text{eff}}$ and $\mathbf{q}_{\text{eff}}$ (defined in equation (4.11)). This condition can be

satisfied only when materials have opposite signs in real part of their dielectric constants; hence, in general, formation of a surface wave at interface of a superconductor requires an additional adjacent positive index medium.

$$\begin{aligned} p_{\text{eff}} + q_{\text{eff}} &= 0 \\ \frac{n_2^2}{n_3^2} p + \frac{n_2^2}{n_1^2} q &= 0 \\ \beta = \sqrt{\frac{n_3^2 n_1^2}{n_3^2 + n_1^2}} k_0 &= \sqrt{\frac{\varepsilon_3 \varepsilon_1}{\varepsilon_3 + \varepsilon_1}} k_0 \end{aligned} \tag{4.11}$$

To have surface wave, one needs [78]:

$$\varepsilon_3 + \varepsilon_1 < 0 \tag{4.12}$$

$$\varepsilon_\infty + i \frac{\sigma(\omega)}{\varepsilon_0 \omega} + \varepsilon_1 < 0 \tag{4.13}$$

Wavevector β entering the dispersion relation of equation (4.11) is a 2D wavevector on the surface between a superconductor and dielectric media. Thus, if a light is incident to the surface in an oblique angle, only in-plane component of this 3D wavevector can couple to the surface wave. According to Fig. 4.3, the dispersion line of an external radiation always lies somewhere between light line inside dielectric medium, $c\beta/n_1$, and the vertical axis. This suggests that light incident to an ideal superconductor cannot directly excite surface plasmon polaritons. Special techniques such as phase-matching[7], $\omega_1/k_1 = \omega_3/k_3$, or mode matching[8] are required to excite these polaritons via a three dimensional beam which will be discussed later.

As the last note, it is reminded that although the dispersion equation for SC/I structure is driven from the dispersion of a slab dielectric waveguide, this structure has a few distinguishable properties:

[7] For instance grating or prism coupling.

[8] This method is typically used for IMI structures with end-fire coupling where SPP is weakly confined to the interface.

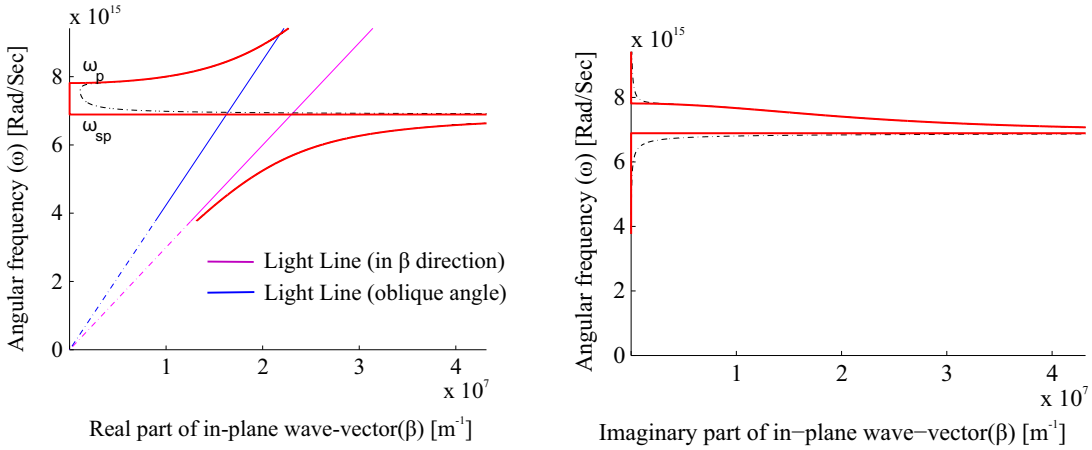

(a) Real part of the SC/I dispersion

(b) Imaginary part of the SC/I dispersion

Figure 4.3: Surface plasmon dispersion of a SC/I structure in NIR bandwidth. ω_p is the plasma angular frequency and the bold red line represents the ideal case where $\gamma \to 0$ $\left(\epsilon_d = 1 - \omega_p^2/\omega\,(\omega + i\gamma)\right)$. If β approaches to infinity, the dielectric constant would be negligible [34].

- The polarization state of $\mathbf{E}$ in the two media are mutually orthogonal ($\beta^2 = pq$):

$$\begin{aligned}\mathbf{E}\,(x>0)\cdot\mathbf{E}^{*}\,(x<0) = \\ E_x\,(x>0)\,E_x^{*}\,(x<0)+E_z\,(x>0)\,E_z^{*}\,(x<0) = \\ \frac{\beta^2-pq}{\omega^2\varepsilon_1\varepsilon_3}H_m\,(x>0)\,H_m^{*}\,(x<0)=0\end{aligned} \tag{4.14}$$

- Surface plasmon wave in superconductor in contrast to dielectric media propagates along $-z$ direction; this is as a result of having negative index of refraction in superconducting area:

$$S_z = (\mathbf{E}\times\mathbf{H}^{*})\,.\hat{a}_z = E_xH_y^{*} = \frac{\beta}{\omega\varepsilon}H_m(x>0)H_m^{*}(x<0) \tag{4.15}$$

- This structure in contrast to the dielectric counterpart only supports a single TM mode. In dielectric waveguides, if a TM mode is available, there must always be a TE mode with the same order but higher effective index.

4.2.2 Effective Index of a Mode

To describe and compare confined modes with just a single variable, it is convenient to define a normalized propagation constant, $n_{\text{eff}} = \beta/k_0 = C/v_p$, where v_p is the phase velocity of the mode. This variable plays an important role wherever an explicit analytical treatment of a structure is not possible. According to the definition, the effective index can be defined for any complex structure as far as the wavevector in direction of propagation is known; however, to directly calculate it from the effective index method, the modes of the actual structure need to be confined well above their cut-off frequencies and linearly polarized such that the scalar wave approximation is valid in all regions [79, 80, 81]. These key assumptions can be only fulfilled when the magnitude of field components in all boundary regions are small enough to be neglected. This condition can be readily violated when there is a strong interaction between layers. For instance, in case of a finite width plasmonic waveguides like our case, this strong interaction would result in a very squeezed optical mode and accordingly, the use of effective index method is on debate [82]. In this section, we introduce a numerical method to address this problem.

To investigate the possibility of mode formation, a numerical tool is required to accurately determine the complex propagation constant of the optical modes as a function of the dielectric core thickness. There are several approaches available to accomplish this task. In this work, a derivative of the well-known transfer-matrix method, namely the reflection pole method or RPM has been chosen [83].

4.2.3 Numerical Approach, Reflection Pole Method

For the design of our multilayer plasmonic waveguide, a numerical tool is required to accurately determine the complex propagation constants as a function of the dielectric core thickness. In this section, reflection pole method (RPM) is introduced for this purpose [83]. This method is a derivative of the well-known transfer-matrix method. Essentially, when the indices of a multilayer waveguide are complex, transfer matrix method boils down to a complex equation rather than a real equation. Finding the roots of this complex equation is numerically challenging. However, in RPM method, instead of directly solving the equation, changes in the phase as a function of the real part of the effective index is monitored.

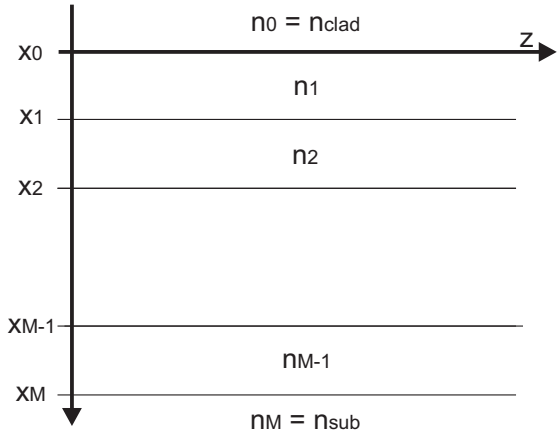

Figure 4.4: A general multilayer waveguide.

In Fig. 4.4, the total electric field of each layer, for instance layer i, is the summation of a forward and a backward propagating electric fields and is expressed as $E_{yi}(x) =$

$A_i \exp\left[-k_i\left(x-x_{i-1}\right)\right]+B_i \exp\left[+k_i\left(x-x_{i-1}\right)\right]$ where k_i is the complex transverse wavevector and A_i and B_i are complex coefficient corresponding to $+\hat{z}$ and $-\hat{z}$ propagating waves, respectively. Furthermore, x_i defines the boundary between the ith and $(i+1)$th layer. By matching the tangential field components of the electric and magnetic fields at each interface, the field expansion coefficients at the cladding and the substrate layer can be related through [83]:

$$M=\begin{pmatrix} A_s \\ B_s \end{pmatrix}=T_{M-1}T_{M-2}\cdots T_0\begin{pmatrix} A_c \\ B_c \end{pmatrix}=\begin{pmatrix} T_{11} & T_{12} \\ T_{21} & T_{22} \end{pmatrix}\begin{pmatrix} A_c \\ B_c \end{pmatrix} \tag{4.16}$$

where T_i is the transfer matrix and defined as follows:

$$T_i=\begin{pmatrix} \left[1+f_i\frac{k_i}{k_i+1}\right]\exp\left(-k_i d_i\right) & \left[1-f_i\frac{k_i}{k_i+1}\right]\exp\left(+k_i d_i\right) \\ \left[1-f_i\frac{k_i}{k_i+1}\right]\exp\left(-k_i d_i\right) & \left[1+f_i\frac{k_i}{k_i+1}\right]\exp\left(+k_i d_i\right) \end{pmatrix} \text{ for } i=0,1,\cdots,M-1 \tag{4.17}$$

For TE modes $f_i=1$ while for TM modes $f_i=n_{i+1}^2/n_i^2$. For an optical wave which is incident to the structure from substrate layer, the electric field in the cladding layer only propagates in the $-\hat{x}$ direction and hence $A_c=0$. In this case, the transmission is given as:

$$\begin{pmatrix} A_s \\ 0 \end{pmatrix}=\begin{pmatrix} T_{11} & T_{12} \\ T_{21} & T_{22} \end{pmatrix}\begin{pmatrix} 1 \\ B_c \end{pmatrix} \tag{4.18}$$

so the reflection coefficient would be $R=\frac{B_c}{A_c}=-\frac{T_{21}}{T_{22}}$. This coefficient is a function of the complex propagation constant. The guided modes are the modes which propagate in the $\hat{z}$ directions and exponentially decay away in the $+\hat{x}$ and $-\hat{x}$ directions or alternatively, they correspond to the resonances of the layered waveguide structure, which happen at the poles of the reflection coefficient R. Consequently, the poles of the reflection coefficient are the solutions of $T_{22}=0$. In RPM method, to find these roots, phase of this complex equation as a function of the real part of the propagation constant is monitored. The guided modes correspond to the rapid changes of the T_{22} phase[9]. According to Bode plot theory [84], an extremum in the derivative of the T_{22} phase corresponds to the real part of the effective index and the full width at the half maximum of the phase derivative curve is the imaginary part [85].

[9]Only phase changes equal or greater than π are correspond to an optical mode

4.3 Excitation of Superconducting Surface Plasmon

As discussed in section 4.2, a unique feature of SPPs is that their in-plane wavevector is larger than the wavevector of a free-propagating optical beam of the same energy. This implies that their dispersion relation lies to the right side of the dielectric light line and hence a special technique is necessary to excite SPPs. Generally, all excitation mechanisms are categorized in two general groups:

(1) Phase matching technique where the momentum of the free-propagating photons are increased such that the phase velocity approaches to that of the SPP.

(2) Spatial mode matching where high coupling efficiency is achieved by matching the mode size of the input wave to the SPP mode.

In the following, the most well-known excitation methods that might have application for excitation of a superconducting strip are discussed. Finally, we suggest an efficient method to excite a nanometer sized superconductor wire. Having the lowest propagation length to have the maximum detection speed and the minimum amount of coupling and radiation losses are the main criteria for selecting the excitation method.

4.3.1 Prism Coupling

This technique, also known as attenuated total internal reflection, is usually employed for the case of a three-layer system in the situations where a free spot upon the dispersive layer is available to locate the prism. As we have discussed earlier in this chapter, there is no crossing between dispersion curve of an SPP and the light line even for light beams aligned to the surface; therefore, the condition for beams oriented in an oblique angle to the surface is even worse[10]. In this method, the projected wavevector along with the interface, $k_x = |\mathbf{K}| \sin(\theta)$, is the one that should be in phase matched to the SPP dispersion [83].

The essence of the prism coupling is to change the slope of the light line by passing the beam through a higher-index dielectric medium (Prism) located just upon the metal

[10]This is a practical situation since usually fiber is placed above the metal interface

surface and rely on the fact that the tunneling of the electromagnetic fields to the lower-index dielectric can take place. If the in-plane component of this wavevector suffice the SPP condition for the other interface, the SPP of the lower-index side will be excited. The approximate angle to have matching is given by,

$$\Theta_{\text{spp}} = \sin^{-1}\left(\sqrt{\frac{\text{Re}\left\{\varepsilon_m\right\}\varepsilon_1}{\varepsilon_2\left(\text{Re}\left\{\varepsilon_m\right\}+\varepsilon_1\right)}}\right) \tag{4.19}$$

where ε_m defines the refractive index of the dispersive layer. In this technique, in addition to the absorption loss within the dispersive layer (the one that we are interested in), there are two other sources of loss: First, *backreflection* from the higher dielectric medium (Prism) due to the index difference between the lower and upper layers. Second, radiation of the excited modes because of their leaky nature. In fact, by placing the driving source in the cladding region, there is no way to excite the actual *guiding modes* of a waveguide and hence all excited modes are inherently leaky. Several options are available to address these obstacles. For instance to reduce the backreflection, one remedy is to choose a prism with refractive index close to that of the lower dielectric medium although most likely this will result in the violation of the phase matching condition 4.19. To reduce the total reflected intensity, one can alter the metal thickness such that destructive interference between these two sources of radiation achieved. With the latter method, it is even possible to reduce the reflected intensity to zero but it would be at the expense of getting far from the minimum possible thickness for our dispersive layer which dramatically degrade the total device efficiency of the detector.

This suggests that it might be more reasonable to keep the superconductor thickness as thin as it can be achieved by the fabrication process, while regenerating SPPs from both radiated sources with an indirect approach. The idea is to connect the prism to an asymmetric waveguide of the same refractive index with an appropriate thickness such that radiated beam reflects back to the metal surface at the right angle to participate in the formation of SPPs [86, 87]. In our model, the fabricated dielectric waveguide on the bottom of the superconducting strip does the same job.

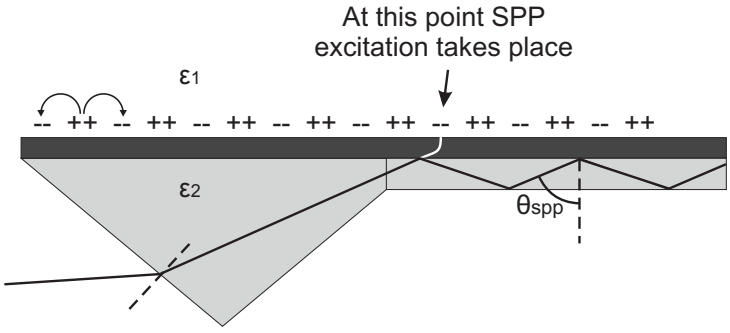

Figure 4.5: Regenerating SPP through coupling to an asymmetric slab waveguide

4.3.2 Grating Coupling

The idea behind this method is exactly the same as the prism coupling [88]. In fact, both methods employ the phase matching technique; however, in this case, the mismatch between the input wavevector and in-plane wavevector of the SPP is overcome by patterning a shallow grating (with depth of only several nanometers with an arbitrary filling factor). The effect of this grating is to reduce the in-place wavevector through the formation of a photonic crystal lattice, $\psi(k) = \psi\left(k \pm \Delta k\right)$:

$$k_{new} = k_{old} \pm n(\frac{2\pi}{|\mathbf{a}|}); \qquad n = 1, 2, 3 \cdots \tag{4.20}$$

Where $\mathbf{a}$ is the primitive vector. Phase-matching takes place whenever the condition $k_{new} = \beta\left(\omega\right)$ is satisfied. The old dispersion equation for β is only valid for a very shallow grating since a significant change in the dispersion relation is expected for the case of deep grating[11]. It is interesting to mention that this phenomena actually happens in all SPPs since in an actual structure, there always exists a random surface roughness. This surface imperfection works exactly like a series of localized scatterers with a momentum of Δk_x so the in-plane wavevector (k_x) can always be approximated as $k \sin\left(\theta\right) \pm \Delta k_x$ where θ is the incident angle.

[11] As a rule of thumb, photonic band-gap can come to the picture for a groove depth on the order of 20 nm.

4.3.3 End-fire Excitation of SPP

The underlying idea behind this method is completely different from that of traditional prism or grating couplings. Here, instead of trying to accomplish the phase matching, spatial mode matching is concerned. Since spatial mode size of an optical fiber is usually much larger than that of a surface plasmon, this method is only efficient for weakly localized SPPs in structures like IMI. Furthermore, it is also common to further decrease the mode size of the input signal with a powerful microscope objective ($60X$, $100X$, or $150X$). This would ensure us to have a sufficiently small mode size in the range of the SPP mode. One advantage of this method is that the excitation of the actual guiding modes can take place; however, due to the surface mismatch between waveguide and fiber, it requires a very high-power driving source and it is likely that most portion of the input beam reflects back from the waveguide tip or couples to the radiation modes of the waveguide.

4.3.4 Dielectric Loaded SPP (DLSPP)

The idea here is to deposit a rectangular dielectric waveguide just on top (or bottom) of the superconducting nanowire. This dispersive layer is no longer a meander structure as in a traditional SNSPD; instead, it is a straight nanowire and the waveguide is aligned with it such that it completely covers the strip. To fabricate this structure, two steps of e-beam lithography is performed to define both the superconducting nanowire and the waveguide core layer. The significant difference in the indices of the dielectric core and cladding layers provides lateral confinement on the order of the core thickness; however, an additional confinement is also expected since inside the dispersive layer, polaritons can be excited and hence surface wave can be formed at the interface of the superconducting layer with either core or substrate layers. Although that this intrinsic sub-wavelength vertical confinement can inherently occur between both interfaces, the effective index would be larger for interface of the superconductor and dielectric core interface [89]. This higher effective index assures the formation of the surface wave inside the core region. Furthermore, if the input light is coupled from the facet of the dielectric waveguide or the excitation directly takes place inside the core region, from dielectric waveguide perspective, only guided modes are

excited and consequently no power can radiate out of the core layer. This implies that in contrary to the previous methods, here, radiation modes are negligible.

4.3.5 Dielectric Loaded Guiding on an Ultrathin Layer

Fundamentally, a plasmonic excitation is attainable in configurations where there is an abnormal TM branch with a higher effective index value compared to that of the first normal TE branch in the effective index versus core thickness diagram [78]. This branch is known as the fundamental TM mode curve and when it appears in the structure, there is an optical mode with exponentially decaying tails in all layers [90, 91]. Fig. 4.6 depicts the real part of the effective index versus the core thickness for two different superconducting film thicknesses. As shown in this figure, by decreasing the thickness of the superconducting layer from 100nm to 8nm, the fundamental TM mode shifts to the right which implies lower confinement for the 8nm thick negative index layer. In contrast to the 100nm thick case, in the 8nm layer, the cut-off thickness is also reduced to zero and there is an inflection point in the curve. In a typical structure, where the thickness of dispersive layer is more than the skin depth of the electromagnetic field, the structure is like an asymmetric slab waveguide and inherently has a minimum thickness for the core layer to support an optical mode. However, when the thickness of the superconducting layer is reduced to a value smaller than the skin depth, the structure starts to behave like a symmetric slab waveguide and the cut-off thickness moves towards zero. For the 8nm thick sample, two different regimes of operation are observed for different core thicknesses. It is important to stress that to have plasmonic guiding for very thin superconducting layers, the top and bottom cladding layers must have a similar refractive index such that the effective index seen by the plasmonic mode at either side is almost equal [78]. This implies that the top cladding layer should have an index greater than or equal to that of the bottom cladding (buried oxide) layer but smaller than the core layer.

We now consider the 8nm thick superconducting structure. To qualitatively describe the importance of the core thickness, without loss of generality, the original four layer structure is considered as a three-layer structure with a semi-infinite boundary at the superconducting layer. With this assumption, surface waves at both interfaces are non-

interacting. This is only valid for structures where surface modes are tightly bound to the superconducting interface, or equivalently, the penetration depth of the electromagnetic field in the superconducting layer is smaller than its thickness. Although this condition is clearly violated in this structure, it can still elucidate the intuitive behavior of the system. At the end of this section precise numerical calculations are also provided.

For a very thick dielectric core layer, where neither a TE nor TM normal optical branch could exist, the structure can support a single plasmonic mode similar to one that is supported by a two layer structure made from semi-infinite core/semi-infinite superconducting layers. Decreasing the core thickness to the range of $\lambda_0/2n_{core}$ where the effect of core thickness is more pronounced, creates a smaller propagation length as the finite thickness of the high index medium forces the optical mode to be more squeezed inside this layer. This is a direct consequence of the fact that the optical wave always tends to distribute itself such that the highest effective index is obtained. The amount of this extra confinement is proportional to the ratio of the optical mode size to the core thickness. Therefore, a smaller propagation length occurs for smaller core thicknesses until some critical point where the optical mode cannot be squeezed any further, reaching its minimum mode field size [85]. Further decrease of the core thickness would result in an increase of the mode field size approaching to the single plasmonic operation of a semi-infinite top-cladding/semi-infinite superconducting structure. Following this idea, the optimum core thickness which yields the maximum mode squeezing and hence the maximum amount of absorption, can be calculated by searching for the maxima in the imaginary part of effective index versus core thickness diagram.

For the case of an ultrathin superconducting layer, the functionality of the core remains the same as far as plasmonic confinement is possible. This can be done by decreasing the core thickness such that the effective index of the TE_0 in the presence of a superconducting layer is larger than that of the TM_0 mode in the absence of a superconducting layer. Using the numerical tool introduced at the beginning of this section and the complex refractive index for the NbTiN film [92], the optimum core thickness for the vacuum wavelength of 1310nm is obtained and the results are summarized in Fig. 4.7. For a fixed core thickness, optical power decays exponentially along the wire due to the absorption in the superconducting film. The amount of absorption is related to the imaginary part of the

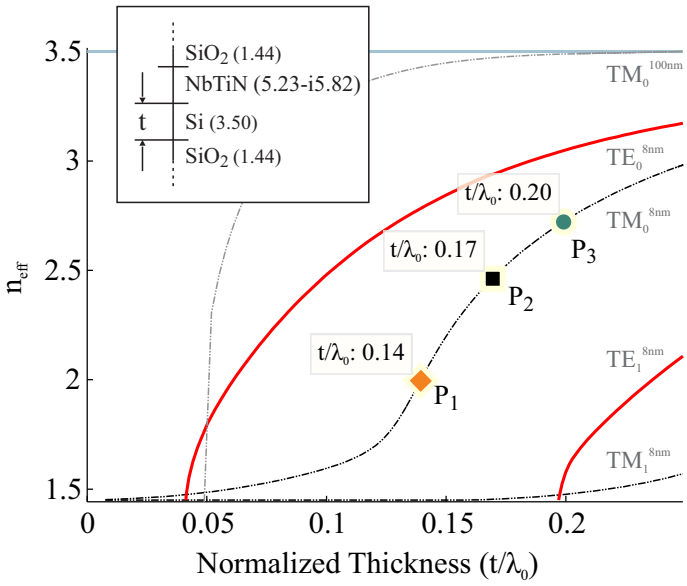

Figure 4.6: Real part of effective index versus normalized dielectric core thickness (normalized to the free-space wavelength) for 100nm and 8nm thick NbTiN superconducting films. For the 100nm case, the fundamental plasmonic mode has a cut-off thickness which is a direct consequence of the single interface plasmonic excitation at the interface of core and superconducting layers. This behavior can be attributed to the penetration depth of the optical mode being larger than the thickness of the superconducting layer. This condition is not satisfied for the 8nm structure. Therefore, no plasmonic excitation is expected unless the structure looks symmetric to the optical mode which happens only for small core thicknesses. Points P_1, P_2, and P_3 will be used later in Fig. 4.7 with the same color scheme.

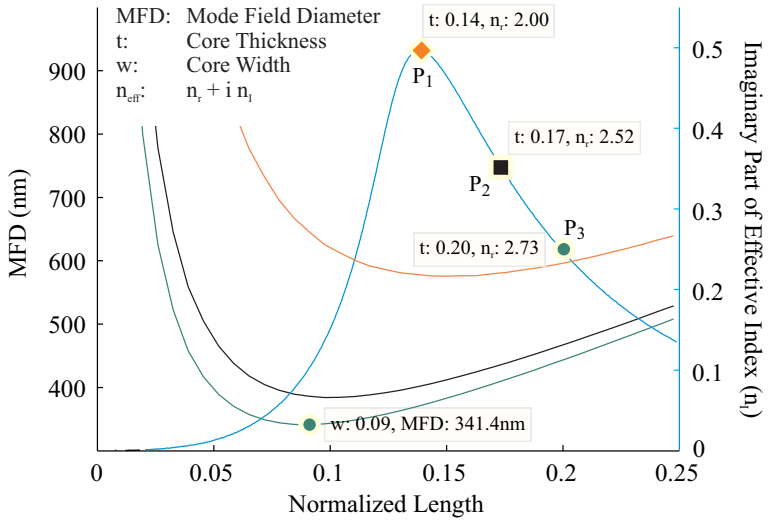

Figure 4.7: Imaginary part of effective index versus core thickness (t/λ_0) for the fundamental plasmonic mode (blue curve) as well as the transverse mode field diameters versus core width (w/λ_0) for three different core thicknesses (green, black and orange curves). The larger the imaginary part of effective index, the stronger the absorption in the dispersive layer. From this figure, the maximum absorption happens at a core thickness of $0.14\lambda_0$. This high absorption is achieved at the expense of not having a confined TM_0 mode when the dispersive layer is absent. By accepting lower confinement for optical mode, higher transverse confinement is obtainable. For instance, for a $0.2\lambda_0$ core thickness, the core width resulting in the minimum transverse mode field size is just $0.09\lambda_0$. Note that by getting far from the maximum point of the blue curve, the lateral mode starts to decouple from the transverse mode and hence a smaller variation in the transverse mode field diameter is predicted. This behavior is observed by comparing mode field sizes of $0.17\lambda_0$ and $0.2\lambda_0$ core thicknesses. Points P_1, P_2, and P_3 refer to three points in Fig. 4.6.

effective index by $e^{-2\mathrm{Im}\{n_e\}\beta_0 l}$ where n_e is the effective index of the confined mode and l is the length of the nanowires. Due to the exponentially decaying nature of the absorption, a saturation point can be defined for the nanowire length as $2\mathrm{Im}\{n_e\}\beta_0 l_{min} > 10$. Here, l_{min} can be considered as the optimum length of the nanowire since further increase of this length just increases the kinetic inductance of the nanowires without significantly improving the absorption. For the optimum core thickness ($0.14\lambda_0$) where the highest confinement is achieved, the minimum wire length to reach saturation is as short as 7.6μm. This minimum length increases by having less lateral confinement. For instance, if core thickness of $0.2\lambda_0$ is chosen, the minimum length would increase to 15.3μm which is still considerably shorter than the normal length of wires used in conventional SNSPDs. These short wire lengths would not be attainable if a higher quality negative index material (e.g., Gold) had been used in place of the NbTiN layer or the plasmonic nature of the thin-film had not been utilized.

4.4 Response Mechanism of a Superconducting Film to an Infrared Radiation

In this section, the maximum cross-section area of the nanowire which is supported by hotspot model is calculated. This area will be used later to find the optimum thickness of the dielectric core layer. To find this maximum cross-section area, dynamics of the superconducting film after photon absorption is studied. This is due to the fact that for a nanometer sized structure even a single-photon can drive the system out of its equilibrium state.

4.4.1 Power dissipation mechanism

From thermodynamic point of view, top core and bottom cladding layers are served as thermal reservoirs for the superconducting film. Any thermal perturbation imposed to the system is suppressed through a sequence of dynamics in which a phononic or an electronic process or even a mixture of both processes is responsible of external energy dissipation

[93]. Based on the dominant component, the process is attributed to different diffusion times and constants. If the perturbation is initiated by absorption of an infrared optical source with frequency much higher than superconducting gap, the downconversion process can be expressed as follows: The first step happens just after the absorption of the photon when a set of two highly excited quasiparticles are generated. These highly nonequilibrium particles are energetically unstable such that their stored energy decays out within a time scale less than a picosecond through strong electron-electron interactions. By the end of this step, a group of excited electrons with energy less than initial photon energy but much higher than Debye energy, is accumulated locally near the photon's absorbed spot. The second step begins when the electron-phonon scattering rate becomes stronger than that of electron-electron scattering which results in an avalanche multiplication of phonons. During this stage, a phonon-mediated quasiparticle generation takes place until the average quasiparticle energy decays to $3\Delta(E)$. This would be the threshold for the generation of active phonons, phonons with energy higher than $2\Delta(E)$, energetic enough to participate in quasiparticle multiplication. In the final step, no more excess quasipaticles will be generated through phononic interaction. The relaxation at this step is all done through naturally slow diffusion and recombination processes. This final step lasts long enough for some phonons to leave the superconducting film for the surrounding thermal reservoirs.

4.4.2 Nonequilibrium Dynamics

Thus far, the optimum thickness of the nanowire supported by plasmonic confinement has been calculated. In this calculation, variation of the electromagnetic field in the transverse plane has been neglected for the sake of simplicity. This approximation is only applicable when the lateral mode distribution of the actual hybrid branch is close to the profile of the equivalent two-dimensional TM mode and the optical mode in the transverse plane can be formed on top of the superconducting layer without feeling its limited width.

To investigate the possibility of mode formation, instead of using the actual indices of refraction, the effective indices of all vertical layers are employed to construct a pseudo two-dimensional waveguide. This waveguide is symmetric with respect to the optical axis which implies a zero cutoff frequency for both fundamental TE and TM modes. Therefore,

for any arbitrary width of the effective core layer, at least one optical mode is expected for both polarizations. This statement is in fact not entirely true for all thickness to width ratios. The decoupling of the actual hybrid mode into a set of perpendicular TE and TM modes is only legitimate when either the width or the thickness of the core layer can be treated as infinite in the length scale of the mode size.

As a consequence, in the slab configuration, to observe a well-defined plasmonic confinement, there is a lower bound on the feature size for the width of the waveguide dictated by the optical design. This imposes an unwanted limitation on the nanowire width from a detection perspective to achieve acceptable single-photon sensitivity, since there is an upper bound for the cross section area of the active element. Consequently, there is a trade-off between the probability of absorption and the internal quantum efficiency of the device. Although it might seem obvious that the poor optical absorption can be corrected by increasing the length of the nanowire in the direction of the wave propagation, it would come at the expense of having higher kinetic inductance or equivalently a slower operating device.

In this section, I will try to develop an intuitive model for the photon detection process, and from that estimate the optimum width of the nanowire to have reasonable detection probability as well as confined plasmonic guiding. To investigate the transient electrodynamics of the initial stage of hotspot formation, the Rothwarf-Taylor rate equations are utilized [94]. These rate equations are essentially coupled diffusion-recombination equations based on current continuity equations of participating particles:

$$\begin{aligned} \left[\frac{\partial}{\partial t} - D_{QP}\nabla^2\right] n_{QP} &= \frac{2n_{ph}}{\tau_B} - \frac{n_{QP}}{\tau_R} \\ \left[\frac{\partial}{\partial t} - D_{ph}\nabla^2\right] n_{ph} &= \frac{n_{QP}/2}{\tau_R} - \left[\frac{n_{ph}}{\tau_B} + \frac{n_{ph} - n_{ph}^0}{\tau_{es}}\right] \end{aligned} \tag{4.21}$$

here, n and n^0 denote the time and position dependent density of the subscript particle in the transient and steady-state regimes, respectively. τ_B and τ_{es} are the time required by a phonon to break a pair or to escape from the hot area if there is an imbalance in the population. τ_R is regarded as the quasiparticle recombination time. D_{QP} and D_{ph}

are phenomenological diffusion coefficients for the quasiparticles and phonons. In this model, there is no constraint on the density of quasiparticles, meaning, the number of superconducting pairs must greatly exceed that of quasiparticles such that there is no limitation on the quasiparticle generation. This condition is only valid when the bath temperature is small compared to the critical temperature and there is no significant local accumulation of quasiparticles. To fulfill these conditions, the first few picoseconds is neglected until the initial photon energy has generated quasiparticles with an average energy of 3Δ. At this point, phonons cannot contribute to quasiparticle generation and hence phonon density can be approximated by the thermodynamic equilibrium value, $n_{ph} = \tau_B/\tau_R \times n^0_{QP}/2$. Having this assumption, the population of quasiparticles as a function of time and position can be studied by injecting $(\hbar\omega/\Delta)\left(1 - e^{-t/\tau_{th}}\right)\delta(r)$ excess quasiparticles during the initial thermalization time, τ_{th}. The resulting quasiparticle distribution can then be used to determine the amount of departure from the equilibrium state by relating the order parameter to the quasiparticle density through the BCS theory considering the strong-coupling regime,

$$n_{QP} = 4 \times 2.08 N(0) k_B T_c I(\beta) \tag{4.22}$$

where $N(0)$ is the single spin electron density, β is equal to $\Delta(T)/k_B T$ and

$$I(\beta) = \int_0^\infty \mathrm{d}y \, \frac{1}{1 + \exp\left[\beta^2 \left(1 + \exp\left(-2F(\beta)\right) y^2\right)\right]} \tag{4.23}$$

$$F(\beta) = -\frac{\beta}{2} \int_0^\infty \mathrm{d}x \, \frac{x \sinh^{-1} x \, \mathrm{sech}^2\left(\left[1 + x^2\right]^{1/2} \beta/2\right)}{\sqrt{1 + x^2}}$$

To express the strong coupling behavior of NbTiN in these films the experimentally determined relation $\Delta(0) = 2.08 K_B T_c(0)$ for the zero temperature energy gap has been used [95]. Combining the normalized quasiparticle density given by the rate equations with Eq. 4.22, the local increase of temperature and suppression of the order parameter can be monitored over time through $I(\beta) = I(\beta_0) n_{QP}/n^0_{QP}$ and $\Delta = \Delta(0) \exp\left(F(\beta)\right)$.

4.4.3 Modeling of Nonequilibrium Dynamics

The nonequilibrium dynamics for absorption of a 1310nm wavelength photon in an 8nm thick NbTiN film is calculated and the results are shown in Fig. 4.8. According to this

figure, the incoming photon creates a finite-sized region with a partially suppressed order parameter within the superconducting film. This region expands over time and destroys the local pair-coherency until the temperature at the center of the spot collapses down to a value less than the superconducting critical temperature. At this point, further suppression of the local order parameter is negligible, defining the end of the first stage of photon detection.

Now the question is whether this local perturbation is strong enough to drive the whole system out of its equilibrium state or if the superconducting coherency could dissipate this extra energy without resulting in a phase transition. To answer this question, two main sources of instability must be studied. The first and the most well-known source is current density beyond the depairing current density outside the hot area in the sidewalks. This source is prominent when the effective width of the strip carrying current can be affected by the formation of the initial spot. To observe a voltage pulse between the two ends of the nanowire, one needs to bias the system with a constant current source with a current density lower than the depairing current in the normal condition, but higher than the depairing current density when the formation of the initial hotspot reaches its maximum effective size. The effectiveness of this source wanes as the film gets wider. For the case where changes in the effective width before and after hotspot formation is insignificant, the second source which is either vortex hopping or vortex-antivortex pair unbinding becomes the dominant source of instability [96, 97]. To make the vortex-based detection an effective mechanism, the Lorentz force between the vortex (antivortex) and the driving current needs to be comparable to the repulsive force due to the barrier shape when no current is flowing.

In conventional SNSPDs, there is no restriction on the minimum width of wires, therefore, to take advantage of the both detection mechanisms, the minimum possible width that can be reliably fabricated (to have vortex-based detection wires need to be wider than 4.4ξ [98]) is usually employed. However, in our plasmonic model, the wider the wires are the higher the optical performance. Therefore, based on the non-equilibrium model introduced in this section, I will try to find a measure for the effectiveness of the current crowding model for a given bias condition as a function of film width. The maximum width where current crowding still has an acceptable impact on the detection process is then selected

as the optimum width for the structure. Certainly the broadening of the nanowires results in a lower internal quantum efficiency resulting from an ebbed contribution of the current crowding mechanism. However, with recent investigations on the adverse effect of sharp turns in the maximum current achievable in practical devices [37, 38], this reduction can be compensated by utilizing an optimum bending procedure introduced in reference [36] and experimentally verified in chapter 2, and also driving the detector with a bias current high enough to have an effective vortex-based detection mechanism.

As a starting point, the current distribution in the nanowire as a function of time and position must be calculated. This can be achieved by writing down the conservation of current density for each time step. To solve this problem, the region with a suppressed superconducting order parameter is bounded to a circle with radius R, with dimensions taken from the half width at half maximum of the actual order parameter spatial distribution. Moreover, the magnitude of order parameter is considered to be a step like function with a value equal to the average of actual order parameter inside the circle and the equilibrium value for the rest of the film. Following the same approach as the one introduced in reference [99], the effect of current crowding in the sidewalks can be expressed in terms of a single coefficient (weight coefficient),

$$\eta_w = 1 - \left(\frac{\alpha R}{w}\right)^2 \frac{\int_{\text{in}} \mathrm{d}s\, n_{QP} - n^0_{QP}}{\int_{\text{in}} \mathrm{d}s\, n_{QP} + n^0_{QP}} \tag{4.24}$$

where α varies from 2 to square root of 2 based on the location of the hotspot. 2 is for absorption at the center of the film and square root of 2 is for absorption at the film edges. According to this equation, aside from the clear width dependency, the size of the initial spot becomes more pronounced when there is a significant difference in the quasiparticle density inside and outside of the hot region.

In the inset of Fig. 4.8(b), the variation of the weight coefficient for a 150nm width wire is plotted. According to this figure, the weight coefficient starts to decay by diffusion of excess quasiparticles from the location of the initial hotspot until the average quasiparticle density in the hot region degrades faster than the hotspot growth rate. At this point, the weight coefficient reaches its minimum value and hence the maximum effect. This time step can be regarded as the end of the initial hotspot formation. The value of the weight

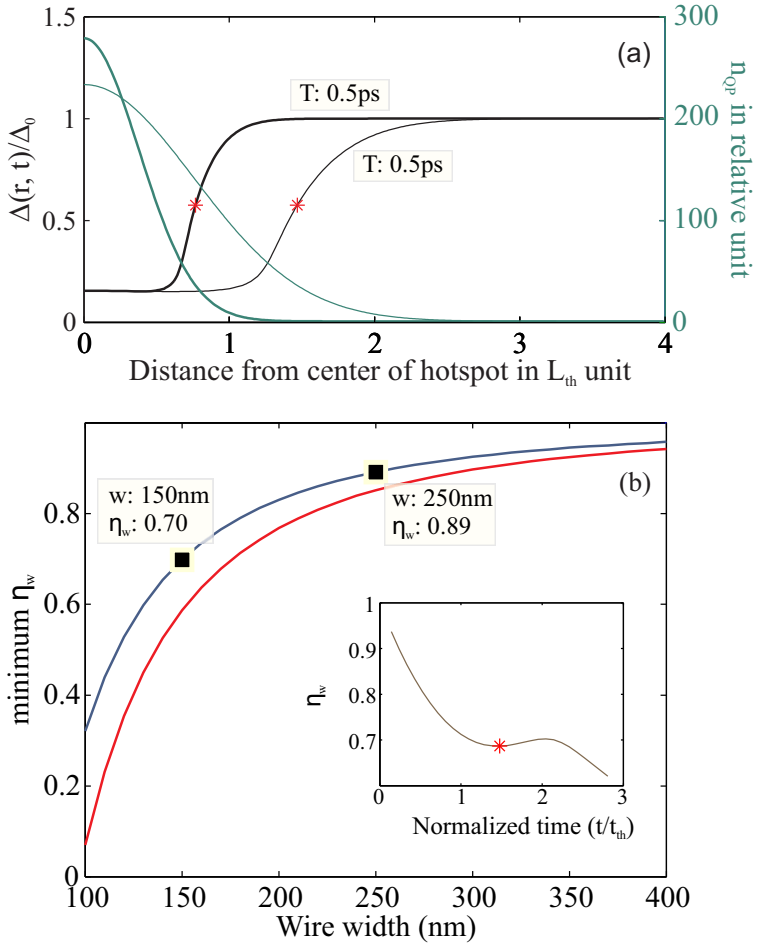

Figure 4.8: (a) Transient electrodynamics of the energy gap and quasiparticle density as a function of time and distance from the hotspot location. (b) Minimum weight coefficient versus wire width for an IR photon with 1310nm wavelength (black line). The weight coefficient can be considered as a measure of how effective the current crowding model is for a specific film width and also provides an approximate normalized current required for unpinning the vortex and antivortex. Red line shows the minimum width requirement for photons with higher energy (1.5 times higher energy compared to the black curve). For these higher energy photons, at a fixed nanowire width, lower current is required to have the same sensitivity.

coefficient at this time step can be considered as a measure of how effectively the initial spot can create a perturbation in the system. In general, two results can be obtained from this coefficient. First, it gives a measure for the effectiveness of the current crowding model for a given film width at a given driving current. Second, it provides an upper bound for the normalized current required for the unpinning of vortex-antivortex pairs from the normal region.

As a conclusion, when the film width increases, the effect of the current crowding model starts to diminish and consequently to keep the film sensitivity, one needs to increase the driving current above the value required by vortex-based detection mechanisms. Based on our simulation, if a photon with a wavelength of 1310nm is absorbed at the center of the wire and the source current is set to 0.7 of the depairing current, only wires with widths smaller than roughly 150nm are well sensitive to photons. This is comparable to the normal maximum achievable current in conventional SNSPDs with sharp turns and 50% filling factor [36]. This minimum sensitivity would jump to 250nm if the driving current can be increased by roughly 20 percent. This can be achieved by replacing all the sharp turns with optimum bends. It is important to stress that from experimental evidence, lower detection efficiency is expected for the vortex-antivortex model [100]. This can be attributed to the fact that not all nucleations can result in sample heating. Thus, by crossing over from the current crowding to vortex-based detection mechanisms, a gradual reduction in system detection efficiency is inevitable. To take advantage from both detection mechanisms, considering no sharp turns in the structure, wires with width less than 200nm are recommended for infrared photon detection.

According to the optical calculations of section 4.2, for a waveguide with confined plasmonic operation (required for getting high optical absorption), a very poor transverse confinement is expected. In this case, the size of the optical mode in the transverse plane is actually the minimum width for both the dielectric core layer and the superconducting layer required to keep the mode's surface confinement. Comparing the results of the nonequilibrium model (maximum acceptable width must be less than 200nm) with the mode field diameter of the first fundamental plasmonic mode, reveals that there is no optimum width for a single nanowire that is wide enough to cover the entire optical mode and still give high photon sensitivity. Although a single wire cannot fulfill both of these

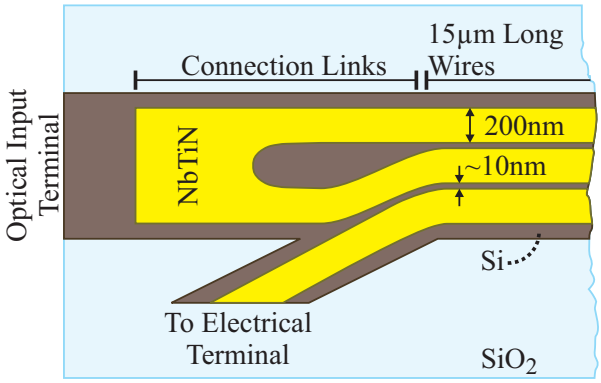

Figure 4.9: Top view of a sample connection link at the input terminal. This link can address the problem of current crowding in a high filling factor device. The detailed instruction on the design of these optimum turns is provided in chapter 2. Optical input terminal can be either an inverse taper coupler or a surface grating coupler [101].

requirements simultaneously, a set of wires parallel to the direction of propagation with a spacing much smaller than the transverse mode field size can be used as a uniform dispersive layer from an optical perceptive. The minimum spacing between wires can be as small as a few nanometers with current fabrication technology and is dictated by the resolution of the electron beam tool used for patterning the wires [32].

Connection of these parallel wires with a high filling factor can generally cause two practical problems as all dimensions are smaller than the Pearl penetration depth (more than 50μm for our device). First, there is no optimum design for bends at this high filling factor resulting in a lower critical current than the one predicted by Kupriyanov and Lukichev [102]. This low driving current leads to a quantum efficiency smaller than what can be potentially expected from the device. More importantly, for a fixed bias current, the device exhibits a larger dark count rate in comparison to straight wires with no bends. The high dark count rate can be explained due to the presence of local areas (bend areas) with current density much higher than that of straight sections. These high bias regions are very small in dimension and cannot enhance device sensitivity, but are susceptible enough to produce huge dark counts with either vortex-antivortex unbinding [42] or vortex hoping origins [46, 58, 41]. To address these issues, we propose connection links with a

non-uniform filling factor and optimally rounded bends at all inner corners (Fig. 4.9). In this design the size of connection links are small enough that they can be neglected in the optical design but can effectively enhance the maximum achievable current of the device.

4.5 Concluding Remarks

In this chapter, the idea of enhancing quantum efficiency of SNSPDs through plasmonic excitation of wires was proposed. In the first section, we discussed the possibility of plasmonic excitation on a superconducting film only a few nanometers thick. We showed that to get the maximum optical confinement, and hence maximum absorption, one needs to use a very thin high index dielectric material in proximity to a thin-film superconductor. The thickness of this core dielectric layer must be smaller than what is required for normal dielectric guiding at the same wavelength. Also, the structure needs to be placed in a structure of a symmetric low index medium. The following section described how the detection mechanism crosses over from the current crowding model to the vortex-antivortex model by increasing the width of the nanowire. A weight coefficient based on nonequilibrium superconductivity was introduced as a measure on the bias condition to keep the device sensitivity when the width is increased. We also demonstrated that there is no optimum width for wires that are wide enough to cover the entire optical mode and still provide high photon sensitivity. To address this issue a set of wires parallel to the direction of propagation with a spacing much smaller than the transverse mode field size with non-uniform filling factors was proposed.

Chapter 5

Optical excitation and coupling techniques

In the previous chapter, I proposed a method to enhance the quantum efficiency of an SNSPD through plasmonic excitation of wires. In the proposed detector, the input optical beam is guided from a slab dielectric waveguide. This is an ideal case for the integration purposes as the detector could be connected to the other integrated components through high performance dielectric guiding structures; however, to evaluate the internal performance of this detector, it is also useful to design a coupling mechanism for the dielectric slab waveguide such that the detector could operate in free-space or fiber-coupled modes too. In this chapter, two possible solutions are discussed.

5.1 High Performance Optical Coupling, End-fire Excitation

In our model, since single-photon detection is concerned and hence the available power is limited, utmost care must be taken to eliminate any potential sources of loss rather than through absorption inside the nanowire. One important location where loss may occur is the tip of the dielectric waveguide where coupling to a single-mode fiber takes place. In

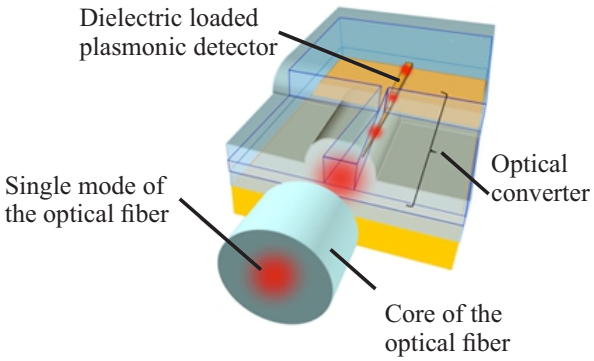

Figure 5.1: Schematic of an optical converter that scales the beam mode field diameter of the input optical fiber down to the mode field diameter of the silicon optical waveguide.

this spot, two main sources of loss are expected: (1) coupling of the fiber mode to the radiation modes of the actual detector. (2) The backreflection due to the index mismatch between effective indices of the device tip and the first optical mode of the input fiber.

To effectively mitigate the first problem, the width of the dielectric waveguide is adjusted such that the mode volume of the input tip approaches to the mode size of the fiber. However, according to the discussion made in section 4.3, the optimum width of the waveguide is always dictated by the propagation length and the amount of absorption inside the active element. To gain the highest possible coupling value without interfering with the design of the active element, it is important to make the design of the inverse taper independent of the waveguide design. To do so, the inverse taper is connected to the actual waveguide through an optical converter as shown schematicly in Fig. 5.1. Furthermore, to *adiabatically* couple the light from the coupler tip to the actual dielectric waveguide, it is important to use a long optical converter[1]. The length of this converter should be long enough such that the input optical mode gradually reduces its mode field size from the non-localized mode of the single-mode fiber to the localized first mode of the actual dielectric structure [103].

To calculate the amount of power backreflection at the input tip of the coupler, the effective indices of the coupler and single-mode fiber are compared to each other. This

[1] Around 500 μm

Table 5.1: Material constants and simulation parameters for a taper with Si core layer at vacuum wavelength 1310 nm

	n_{core}	n_{clad}	h_w [a]	$\mathrm{d}x = \mathrm{d}y$	BC [b]	CD (WS) [c]	CD (S) [d]
Si core	3.49	1.44	232.5 nm	$\frac{h_w}{140}$	000S	8.02 μm × 16.22 μm	14.04 μm × 22.23 μm

[a] Waveguide height

[b] Boundary conditions: 'A' - Hx is antisymmetric, Hy is symmetric. 'S' - Hx is symmetric and, Hy is antisymmetric. '0' - Hx and Hy are zero outside of the boundary.

[c] Computational Domain (without stretching)

[d] Computational Domain (with stretching)

value is estimated to be less than 5% if the dielectric loaded detector is surrounded with a dielectric material of refractive index close to that of the input fiber, and it can be further eliminated by placing a quarter-wavelength anti-reflective coating before the taper's input facet. To evaluate the modes profile of these structures, since the coupler is inherently a three-dimensional slab waveguide with aspect ratio (width to thickness ratio) close to unity, the guiding modes cannot be decoupled into the two-dimensional counterparts, TE and TM modes, and hence a full vectorial calculation is suggested. In the following section, a numerical tool is introduced as our primary computational tool to evaluate these hybrid modes.

5.1.1 Numerical Approach: Full Vectorial Dielectric Mode Solver

In this section, a full-vectorial numerical mode solver is introduced [104]. This method is based on writing down the Maxwell's magnetic wave equation[2] in terms of just the two transverse magnetic field components, and then forming a set of coupled equations. Eventually, these set of continuous coupled equations are converted to an eigenvalue problem by representing a discrete set of elements. The solution of this eigenvalue problem leads to the mode profiles and effective indices of the complex structure.

In the divergence relation for a non-magnetic material, $\boldsymbol{\nabla}\cdot\mathbf{H} = 0$, if one of the principal

[2] $\boldsymbol{\nabla}\times\varepsilon^{-1}\boldsymbol{\nabla}\times\mathbf{H} - \mu\dfrac{\partial^2\mathbf{H}}{\partial t^2} = 0$

Table 5.2: Material constants and simulation parameters for a single-mode fiber at vacuum wavelength of 1310 nm [105]

n_{core}	n_{clad}	r_c [a]	$\mathrm{d}x = \mathrm{d}y$	BC [b]	CD (WS) [c]	CD (S) [d]	n_{eff} for E^Y mode
1.4628	1.4600	4.7 μm	$\frac{r_c}{140}$	0S0S	16.45 μm $\times$ 16.45 μm	23.5 μm $\times$ 23.5 μm	1.461

[a] Core radius

[b] Boundary conditions: 'A' - Hx is antisymmetric, Hy is symmetric. 'S' - Hx is symmetric and, Hy is antisymmetric. '0' - Hx and Hy are zero outside of the boundary.

[c] Computational Domain (without stretching)

[d] Computational Domain (with stretching)

axes is aligned with the direction of wave propagation[3], one magnetic field component is dependent to the other magnetic field components through:

$$H_z = \frac{1}{i\beta}\left(\frac{\partial H_x}{\partial x} + \frac{\partial H_y}{\partial y}\right) \tag{5.1}$$

Making use of this relation, it is possible to express the magnetic wave equation just in terms of two transverse magnetic components only with the knowledge of material indices,

$$\varepsilon = \begin{bmatrix} \varepsilon_{xx} & \varepsilon_{xy} & 0 \\ \varepsilon_{yx} & \varepsilon_{yy} & 0 \\ 0 & 0 & \varepsilon_{zz} \end{bmatrix} \tag{5.2}$$

By substitution this equation into the magnetic wave equation, after some algebraic simplifications, two coupled eigenvalue equations are obtained. Even though the Hamiltonian of magnetic field wave equation by its nature is non-Hermitian, as long as the material indices are real, this yields a real set of effective indices since this solution coincides with

[3] Like previous sections, z dependency of field components is assumed to be $\exp(-i\beta z)$

	Symmetric	Anti-symmetric
Electric Components	$E_{\parallel}^{+} = E_{\parallel}^{-}$ $E_{\perp}^{+} = -E_{\perp}^{-}$	$E_{\parallel}^{+} = -E_{\parallel}^{-}$ $E_{\perp}^{+} = E_{\perp}^{-}$
Magnetic Components	$H_{\parallel}^{+} = -H_{\parallel}^{-}$ $H_{\perp}^{+} = H_{\perp}^{-}$	$H_{\parallel}^{+} = H_{\parallel}^{-}$ $H_{\perp}^{+} = -H_{\perp}^{-}$

Table 5.3: Boundary conditions when structure has symmetry

the solution of electric field counterpart.

$$\frac{\partial^2 H_x}{\partial x^2} + \frac{\varepsilon_{yy}}{\varepsilon_{zz}}\frac{\partial^2 H_x}{\partial y^2} + \frac{\varepsilon_{yx}}{\varepsilon_{zz}}\frac{\partial^2 H_x}{\partial y \partial x} + \left(1 - \frac{\varepsilon_{yy}}{\varepsilon_{zz}}\right)\frac{\partial^2 H_y}{\partial x \partial y} \tag{5.3}$$

$$- \frac{\varepsilon_{yx}}{\varepsilon_{zz}}\frac{\partial^2 H_y}{\partial x^2} + \omega^2 \mu_0 \left(\varepsilon_{yy} H_x - \varepsilon_{yx} H_y\right) = \beta^2 H_x \tag{5.4}$$

$$\frac{\partial^2 H_y}{\partial y^2} + \frac{\varepsilon_{xx}}{\varepsilon_{zz}}\frac{\partial^2 Hy}{\partial x^2} + \frac{\varepsilon_{xy}}{\varepsilon_{zz}}\frac{\partial^2 H_y}{\partial x \partial y} + \left(1 - \frac{\varepsilon_{xx}}{\varepsilon_{zz}}\right)\frac{\partial^2 H_x}{\partial y \partial x} \tag{5.5}$$

$$- \frac{\varepsilon_{xy}}{\varepsilon_{zz}}\frac{\partial^2 H_x}{\partial y^2} + \omega^2 \mu_0 \left(\varepsilon_{xx} H_y - \varepsilon_{xy} H_x\right) = \beta^2 H_y \tag{5.6}$$

Now the final step is to discretize these equations to construct the final eigen-matrix. In discretization process, the spacing between mesh points does not need to be uniform; in fact, non-uniform spacing in the cladding area increases the size of the computational domain without introducing extra nodes or reducing the precision of the calculation. In this simulation, the computational region is considered to be $20\,\mu$m by $20\,\mu$m square to assure that all mode amplitudes are negligible at all the boundaries for both coupler and single-mode fiber. Furthermore, since both structures have a mirror symmetry in y direction, one can take advantage of this symmetry to reduce a factor of two in time and storage of the simulation. Under symmetry, each field component transforms appropriately according to its vectorial nature as mentioned in table 5.3. In particular, electric field transforms as *vector*, while magnetic field transforms as *pseudo-vector*[4].

[4]In physics, a pseudo-vector is a vector object that transforms like a vector under a proper rotation, but gains an additional sign flip under reflection. In particular, electric fields or electric currents transform as vectors, while magnetic fields and magnetic currents transforms as pseudo-vectors.

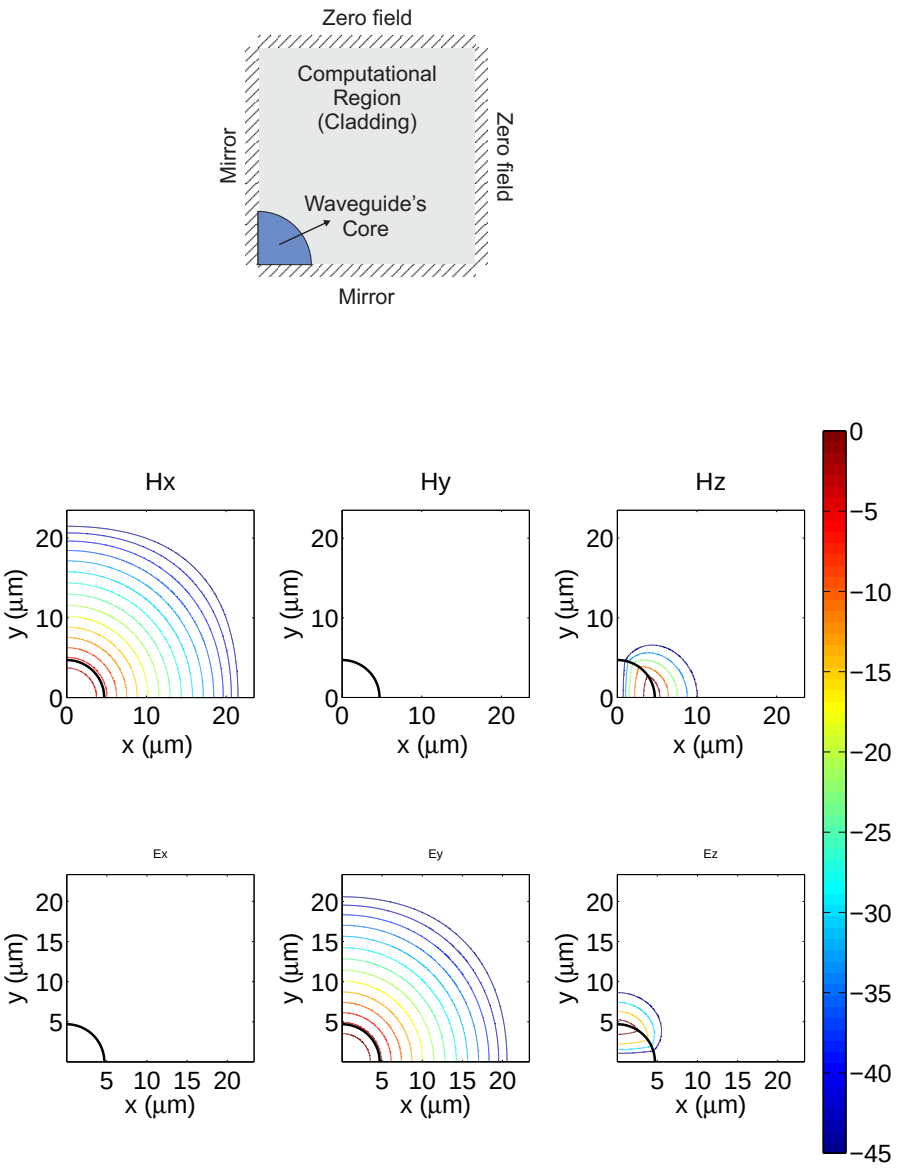

Figure 5.2: Electromagnetic field components of E^Y mode of a single-mode fiber with parameters of table 5.2. Black bold circle defines the location of the fiber core.

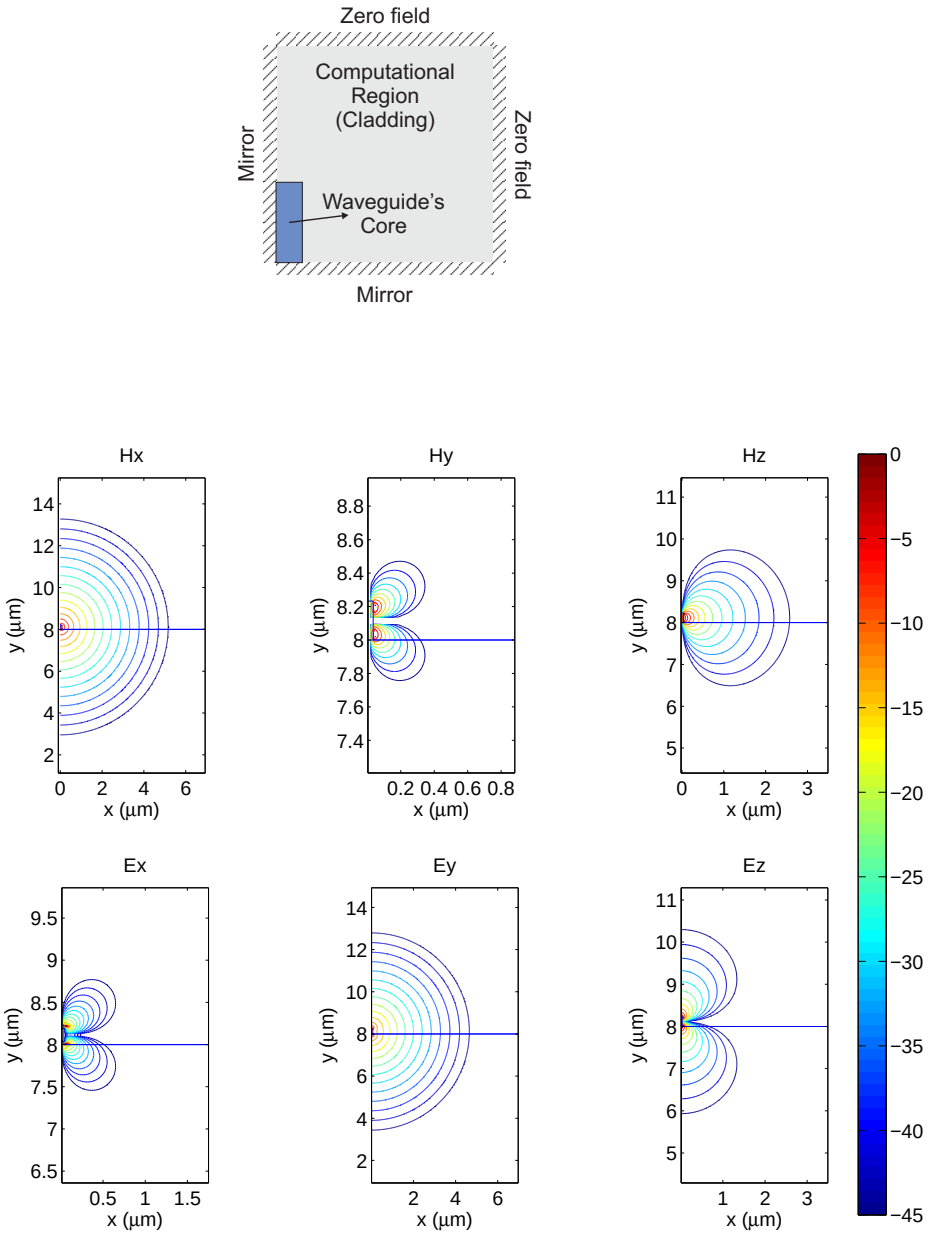

Figure 5.3: Electromagnetic field components of E^Y mode of a Si taper with parameters of table 5.1. Core width and height are 70.0 nm and 222.0 nm, respectively. Note that for illustration purposes, dimensions are not to scale.

Table 5.4: Coupling efficiency of 220 nm thick silicon waveguides with various widths to a single mode optical fiber.

width (nm)	200	100	80	70	60
η_c	0.0502	0.3412	0.4102	0.8525	0.9829
n_{eff}	1.52922	1.44863	1.44631	1.44501	1.44008

Having the optical mode profiles of the single mode fiber and the inverse taper (see Figs 5.2 and 5.3), the coupling efficiency (η_c) is defined as [106],

$$\eta_c = |a|^2 \frac{N}{P} \tag{5.7}$$

where

$$N = \frac{1}{2}\int_{\text{domain}} \left(\mathbf{E}^*_{T,t} \times \mathbf{H}_{T,t}\right) \cdot \mathbf{a}_z \, \mathrm{d}s \tag{5.8}$$

$$P = \frac{1}{2}\int_{\text{domain}} \left(\mathbf{E}^*_{T,f} \times \mathbf{H}_{T,f}\right) \cdot \mathbf{a}_z \, \mathrm{d}s \tag{5.9}$$

$$a = \frac{1}{2N}\int_{\text{domain}} \left(\mathbf{E}^*_{T,t} \times \mathbf{H}_{T,f}\right) \cdot \mathbf{a}_z \, \mathrm{d}s \tag{5.10}$$

here, subscripts f, t and T stand for the fiber, taper and transverse field components, respectively. Electromagnetic field profiles for E^Y modes of the taper and single-mode fiber are shown in Figs. 5.2 and 5.3. The coupling efficiency as a function of the coupler width for Si core layer is listed in table 5.4. As the width of the coupler tip increases, the mode size decreases. When the mode size of the coupler at its tip becomes similar to the mode size of the single-mode fiber, the coupling loss is minimized. For Si waveguide, this minimum value occurs for coupler width of around 60 nm. Even in this region, although the mode sizes are similar and also effective indices of both structure are very close to each other, the coupling efficiency is not exactly equal to one. This is due to the difference in the mode shape between the fiber and the coupler.

In summary, according to the discussion made in the previous chapter, there exists a minimum thickness and width for the dispersive layer to support the fundamental plasmonic mode. These minimum dimensions are related to the refractive indices of all the

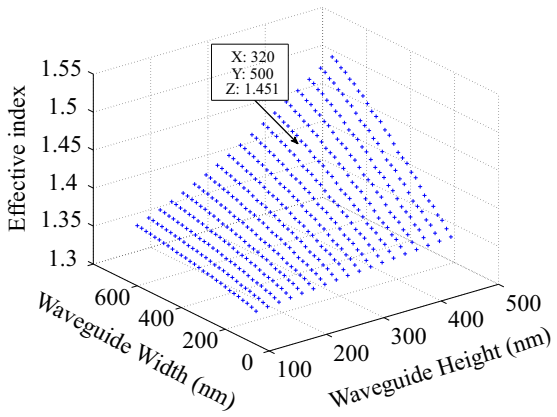

Figure 5.4: Effective index versus core thickness and width for a Si slab waveguide in an environment of SiO_2.

materials used in simulation that make the design of the coupler a bit challenging. To mitigate this problem, an optical converter is introduced in this chapter that connected the actual inverse taper to the active element such that the coupling loss and backreflection power were minimized. These results suggest that by using an inverse taper, we can simply gain an unlocalized mode at the taper tip with an effective index and a mode size very close to those of single mode fiber such that coupling loss between the detector and external optical link is extremely small.

5.2 Low Performance Optical Coupling, Grating Excitation

In this section, a systematic criteria is developed to design an input dielectric grating coupler as the input power collector for our single-photon detector. All the results and simulations are based on an improved perturbation analysis method [107]. The results of this simulations cover both TE and TM modes and they apply to both shallow and deep grating profiles [108, 109]. The purpose of this grating is to collect as much as possible of the input optical power to transfer the energy into the active element when the detector is employed for detection of free-space radiation.

The rigorous treatment of dielectric gratings is based on the pertinent boundary-value problem [110, 111] which is quite complex and requires time-consuming computer programs to yield the accurate quantitative results. To avoid this complexity several perturbation approaches have been developed [112, 113, 114, 115, 116], however the majority of these approaches are limited to specific profiles. Here, by using the improved perturbation approach, the restriction over grating profile has been removed. The mathematical derivation of the electromagnetic coupling problem is given in reference [107]. Using these results, the grating efficiency is expressed in terms of the known grating parameters through an approximate but explicit formula. For further optimizing the grating design, a full finite difference time domain simulation is also performed on the final structure.

The underlying idea behind the design of all gratings is to make a surface perturbation to the system such that a guiding wave of the structure is transfered into one or more leaky waves. This means that a grating is actually a scatterer such that the input energy is leaking out into space-harmonic fields of the form $\exp\left[i\left(\beta_0 + (2\pi n/d) + i\alpha\right)\right]$ where d is the grating period, α is describing the leakage of the energy and β_0 is closely equal to the K-vector of the incident surface wave considering that the permittivity of the grating section is not different from that of the waveguide structure by a large value. These leaky waves eventually radiate into the cladding region at angles

$$\Phi_n = \sin^{-1}\left(\beta_n / K_{\text{clad}}\right), \qquad n = 0, \pm 1, \pm 2, ... \tag{5.11}$$

According to this equation, out radiation only occurs for the leakage beams that satisfy

$|\beta_n/K_{\text{clad}}| < 1$. Hence the number of outgoing beams is be controlled by selecting a proper value of d. Based on the sign of the radiation angle, the output beams are divided into two sections, forward and backward radiation. The boundary of $N_{\text{eff}} = \lambda/d$ defines the boundary of these two sections and corresponds to the resonance case for which the input K-vector satisfies the gap condition of a one-dimension photonic crystal ($\beta_0 d = 2\pi$). This is the case where the entire power of the incident beam is reflected back to the waveguide structure rather than being transformed into the output leakage. To avoid this, in practice, a minimum angle of $3 - 4$ degrees is required for the first and probability the dominant leakage term. In theory, if the length of the grating is sufficiently long, it is possible to convert all of the available input energy into the output beams. In the reciprocal case of the input coupler, if the input beam has the intensity profile identical to that of the outgoing beam of the same structure when it is employed as an output coupler, a complete power conversion is achievable. In practice however, the incident beams most likely have profiles quite different from the matching profile. For example in the case of a Gaussian incident field, at most 80% of the incoming power can be transfered to the waveguide structure. For the case of a uniformly distributed incident beam, the maximum achievable coupling is only 81% [107]. In general, for these two well-known profiles, the maximum conversion is reached when the beam width (w_G) satisfies $\alpha w_G \sec(\theta_0) = 1.36$ and $\alpha w_G \sec(\theta_0) = 1.25$, respectively.

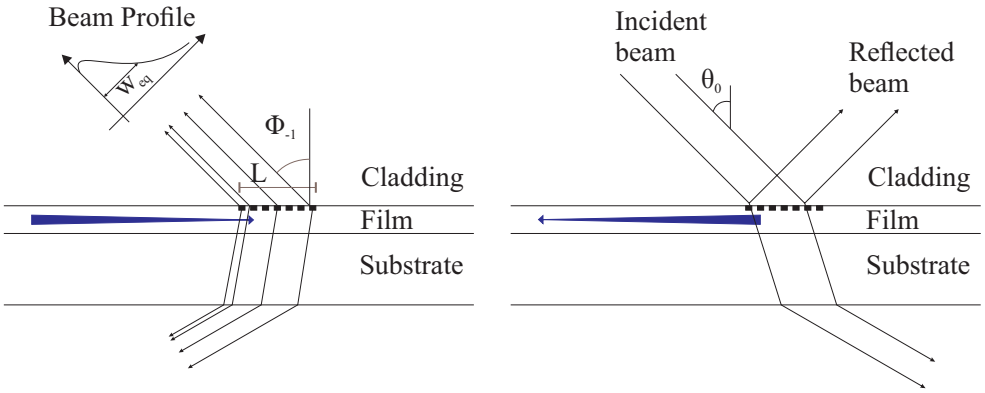

Figure 5.5: Dielectric grating coupler viewed as guided wave to leaky wave converters. (a) Output coupler, (b) Input coupler.

Before studying the actual design, the importance of the different physical parameters of a grating design is reviewed:

5.2.1 Effect of the Trenches Size

For a rectangular grating, the leakage parameter, α, is defined as the imaginary part of the eigenvalue of the Maxwell's boundary value problem[5]. Using improved perturbation theory, if only $n = -1$ field component is contributed to the leakage, then the leakage term can be approximated as [107],

$$\alpha = \alpha_h \left(\epsilon_r - \epsilon_a\right)^2 \sin^2\left(\pi d1/d\right) \tag{5.12}$$

where to the first order of magnitude, α_h is not a function of the trench size. According to this formulation, the leakage coefficient of the first field component reaches its maximum just close to $d_1 = d/2$ and varies as a squared sine function away from the maximum point. Consequently, for the first backward leakage term, the largest conversion occurs when the trenches size is just half of the actual grating period. The variation of α with respect to the trench width is illustrated in Fig. 5.6

5.2.2 Effect of Periodicity Length

The periodicity of the grating region influences the number of the outgoing beams and their leakage angle. Using improved perturbation theory it is possible to show that d/λ can vary without introducing large changes in the leakage power. For instance, for a normal grating design, the leakage varies only by 10% if d/λ sweeps over a range of $0.4 - 0.6$.

[5]Will be discussed in more details in section 5.2.3

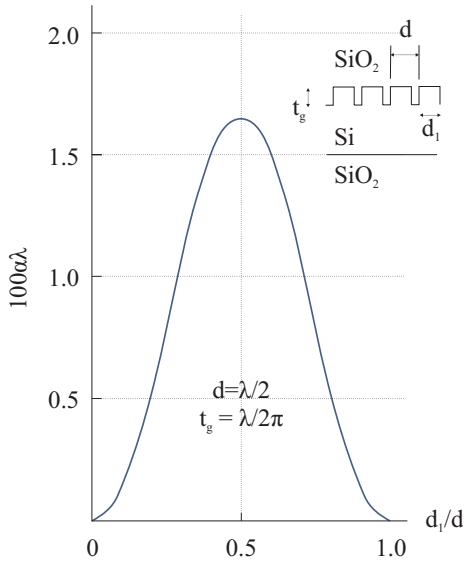

Figure 5.6: Simulation results for normalized leakage versus aspect ratio for a typical rectangular slab waveguide.

5.2.3 Basics of Improved Perturbation Analysis of Dielectric Gratings

As a starting point, the relative dielectric constant of a grating structure with an arbitrary profile is defined as:

$$\epsilon(x, z) = \epsilon_u + \epsilon_p(x, z) \tag{5.13}$$

where the subscript u denotes the material of the cladding, core, or grating region. Neglecting the spatially varying $\epsilon_p(x, z)$ parameter, the structure is just a simple multi-layered slab waveguide which is uniform with respect to both x and y directions. Note that, the term ϵ_p is zero for all regions except the grating section. In this special region, ϵ_g refers to the volume-average of the refractive index [108].

In improved perturbation method, the quantity $\epsilon_p = \epsilon_p(x, z)$ which is the actual variation of the grating layer, is described as the perturbation imposed to the multi-layered unperturbed structure. Due to the periodicity of this region, the perturbation can be

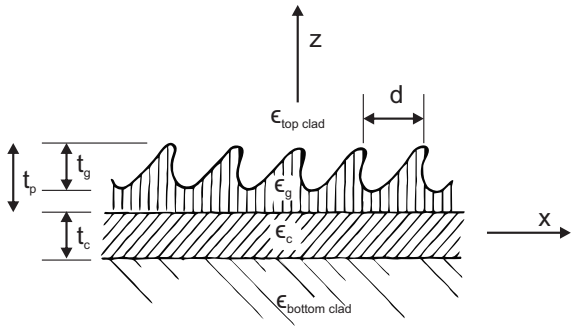

Figure 5.7: Geometry of an arbitrary grating structure

expanded as a Fourier series:

$$\epsilon_p = \epsilon_p(x,z) = \sum_{n=-\infty}^{\infty} \epsilon_n(z)\exp(i2n\pi x/d) \tag{5.14}$$

Since the average of the grating region is encapsulated in ϵ_u term, the $n = 0$ term satisfies:

$$\int_0^{t_g} \epsilon_0(z)\mathrm{d}z = 0 \tag{5.15}$$

Now by knowing the refractive index distribution of the structure, the electric and magnetic field vectors are written as,

$$\mathbf{E} = \mathbf{E}_u + \mathbf{E}_p \tag{5.16}$$

$$\mathbf{H} = \mathbf{H}_u + \mathbf{H}_p \tag{5.17}$$

where $\mathbf{E}$ and $\mathbf{H}$ refer to the fields in the actual structure. These two field elements can be written as $\mathbf{E}_u$ and $\mathbf{H}_u$ field elements of the unperturbed structure superposed with $\mathbf{E}_p$ and $\mathbf{H}_p$ fields when the periodic structure is introduced to modify the initial multi-layered structure into the actual grating configuration.

Regardless of the contribution of $\mathbf{E}_u$ and $\mathbf{H}_u$ field components to the equations (5.16) and (5.17), they are required to satisfy Maxwell equations independently. Knowing this, a

new Maxwell equation set is introduced as,

$$\nabla \times \mathbf{E}_p = i\omega\mu_0 \mathbf{H}_p \tag{5.18}$$

$$\nabla \times \mathbf{H}_p = -i\omega\epsilon_0 \left(\epsilon_u \mathbf{E}_p + \epsilon_p \mathbf{E}_p + \mathbf{P}\right) \tag{5.19}$$

Here $\mathbf{P} = \epsilon_p \mathbf{E}_u$ is a known dipole distribution generated by the interaction between the incident field and the periodic perturbation ϵ_p. Now by comparing $\epsilon_p \mathbf{E}_p$ term to all the other terms, it is possible to show that this term is a second order perturbation [107]. Hence the solution to the actual field elements is resolved into two steps; first, finding the field distribution of the unperturbed structure using homogeneous Maxwell equations and then calculating the perturbation terms of equations (5.18) and (5.19) along the same structure by employing inhomogeneous Maxwell equations. This leads to a result for electromagnetic field distributions inside the grating to the first order of perturbation. The guided wave modes of the unperturbed structure are invariant with respect to y axis and their filed are decomposed into either TE or TM modes. However, the presence of the grating region is modifying these waves so that they leak out energy into both the top and bottom capping regions. For a first order perturbation, i.e. $\epsilon_p \mathbf{E}_p \to 0$, the real surface wave propagation factor of the unperturbed structure, β_0 is replaced by a complex quantity $k_x = \beta_0 + i\alpha$.

5.2.4 Simulation Results

Our plasmonic detector is made of 8nm thick NbTiN films deposited on an SOI chip with 220nm thick silicon layer. Hydrogen silsesquioxane resist was spin-coated on top and pattered using 125keV electron beam lithography for both waveguide and nanowire patterning steps. The write parameters were carefully tuned to achieve sharp and smooth edges for dielectric waveguide sections as well as round bend curves for the nanowires as identical as possible to the designs. The resist was developed in a tetra-methyl ammonium hydroxide solution, and the pattern was transferred into the film using ion beam milling with Argon gas. Fig 5.8 depicts a high resolution SEM image of the grating section.

To achieve the highest possible coupling in the grating area and hence maximum available system detection efficiency, the improved perturbation analysis has been performed

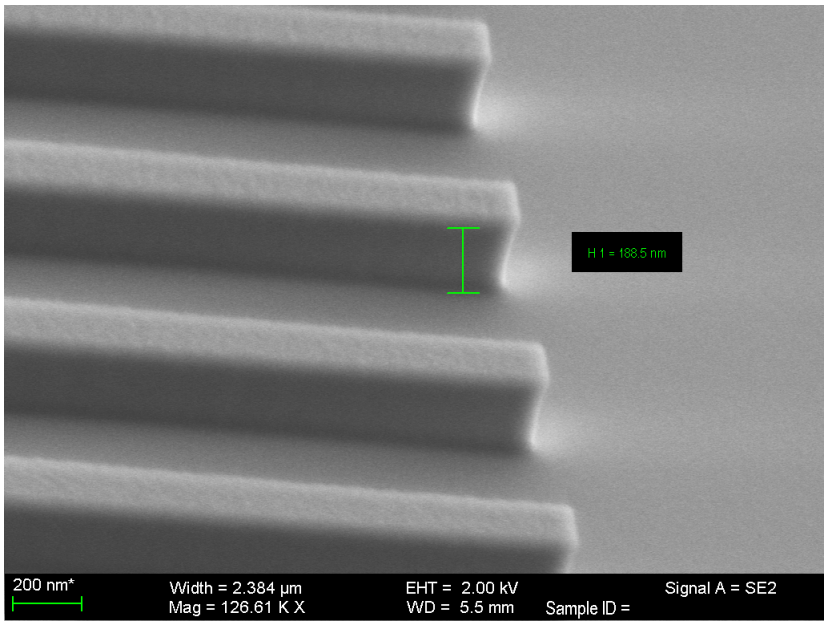

Figure 5.8: A high resolution SEM image of a deep grating design for free-space operation of the dielectric loaded plasmonic detector.

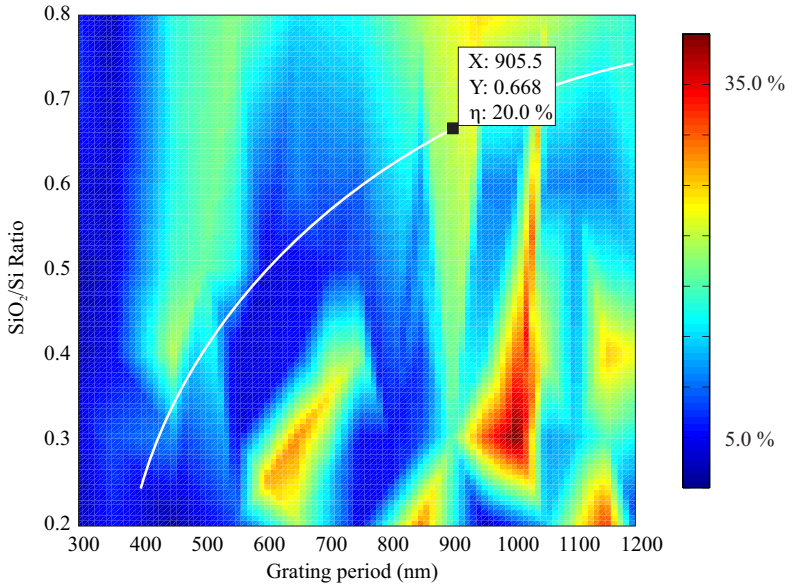

Figure 5.9: Simulation result for the light coupling efficiency versus grating periods and Si to SiO_2 ratio for a deep grating profile (220nm thick). The structure is excited with a Gaussian beam of TE polarization. White bold line depicts the efficiency of the fixed 300nm width silicon portion. There is a quarter wavelength SiO_2 capping layer on top of the entire structure. This capping layer is mandatory for the plasmonic operation of the detector and also it improves the coupling efficiency of the grating structure by acting as an optical cavity.

for a wide range of grating periods and trench sizes (grating period of 300nm to 1.2μm and grating ratio of 20% to 80%). Results of these simulations are listed in Figs. 5.9 and 5.10. For this particular case, since the thickness of the grating structure is identical to the actual weaveguiding structure, it is favorable to keep the width of the silicon portion the same as the actual waveguiding structure such that the grating coupler could be potentially collaborate in the single-photon detection as well. White bold lines in the TE and TM simulations depict the results for the coupling simulations for the fixed 300nm width silicon portions. Maximum value of the coupling for each polarization has been selected and used for the device fabrication.

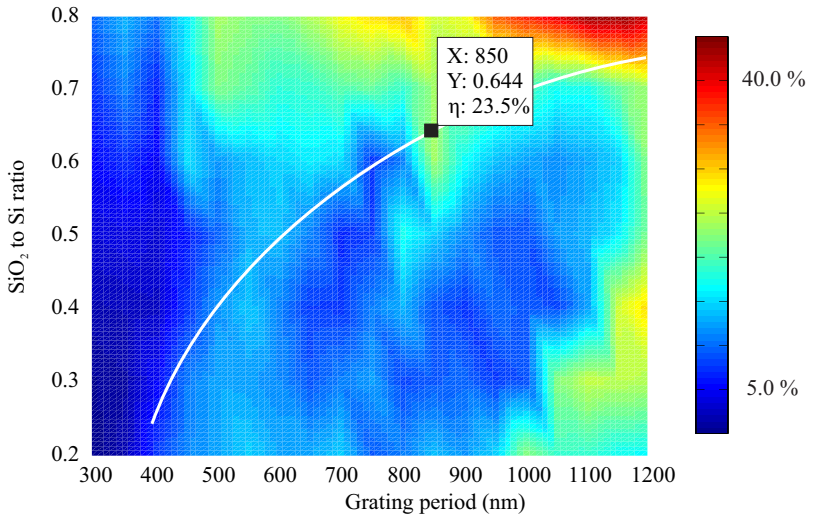

Figure 5.10: Simulation result for the light coupling efficiency versus grating periods and Si to SiO_2 ratio for a deep grating profile (220nm thick). The structure is excited with a Gaussian beam of TM polarization. White bold line depicts the efficiency of the fixed 300nm width silicon portion. There is a quarter wavelength SiO_2 capping layer on top of the entire structure. This capping layer is mandatory for the plasmonic operation of the detector and also it improves the coupling efficiency of the grating structure by acting as an optical cavity.

Chapter 6

Conclusion and Contribution

In conclusion, I proposed an integrated version of a nanowire single-photon detector. The main challenge of this work was to enhance the total system efficiency of this class of detectors while keeping the idea of integration at the forefront. In general, the low quantum efficiency of the detector is attributed to the great difference between the thickness of the superconducting film and the skin depth of the incident optical beam, such that the beam could readily pass through the meander structure of the detector without seeing the narrow superconducting layer. Our proposed dielectric loaded plasmonic detector solution addresses this problem. The design, simulation, and characterization of the required components from geometrical optimization to the photon detection process were performed during this work. A more detailed summary of the different steps are as follows,

I first explored the possible geometrical improvement of a nanowire single-photon detector at the bend area. The presence of these turns is mandatory to electrically connect straight nanowire segments together to form a single active element. However, it has been shown that these sharp turns could dramatically reduce the total system efficiency of a detector. In short, the adverse impact of these sharp turns can be classified into two categories: (1) Limiting the bias current of the device and hence putting an upper bound to the internal quantum efficiency of the device which is less than what the detector is capable of, and (2) generating excess dark counts at the bend areas due to the higher current concentration whereas the actual photon detection process happens at the straight

nanowire segments. A systematic approach to address the bend problem has been proposed and experimentally verified. In the experiment, it has been shown that the utilization of the optimally-designed bend structures could push the detector further as a more efficient single-photon detector in terms of having a higher critical current and lower dark count rates [21].

Next, I explored the physical origins of the dark count generation in a nano-pattered superconducting sheet. A clear picture of all possible processes that might lead to the normal belt formation when the input terminal of the detector is fully blocked is discussed. It has been both theoretically and experimentally shown that regardless of the physical model of the dissipative process, the dark count generation is always directly dependent to the width or height of a potential barrier, barrier which originates from the self energy of the superconductor. In general, it has been demonstrated that vortex hopping and vortex-antivortex unbinding in thermal or quantum levels are the primary resources of the dark count generation in a two-dimensional narrow superconducting sheet. To predict the thermal activation or quantum tunneling liberation rate, a precise estimate of the shape of this energy barrier at the film edges or at the location of singularity nucleation is crucial. This is while, in the London approximation for the barrier shape which is the most common model used to describe the barrier, there is an unacceptable simplification for the barrier calculation at the location of a singularity. For a more accurate estimation of the barrier shape, a quantum mechanical treatment needs to be proposed. In our quantum model, based on the inertial mass of the singularity and the barrier confinement, a current-controlled initial energy level is introduced for singularities. It has been experimentally verified that the usage of this energy level results in a more accurate prediction for the rate equations. The quantum treatment of the potential barrier also revealed that both the vortex-antivortex unbinding and the dissipative quantum tunneling models may have higher rates than those predicted by the classical models which suggest higher contribution of these sources of dissipation in the final dark count generation [59].

Finally, the idea of enhancing quantum efficiency of a nanowire single-photon detector through plasmonic excitation of wires was proposed. It has been showed that by placing the active element on top or bottom of a dielectric slab waveguide, it is possible for the superconducting nanowires to interact with the input optical light provided that the thick-

ness and width of all layers are chosen carefully. It has been shown that even when the superconducting layer has a few nanometer thickness, excitation of surface plasmons is still possible. That was shown to get the maximum optical confinement, and hence the maximum absorption, one needs to use a very thin high index dielectric material in proximity to a thin-film superconductor. The thickness of this core dielectric layer must be smaller than what is required for normal dielectric guiding at the same wavelength. Also, the structure needs to be placed in an environment of a symmetric low index medium. Even with all these consideration, it has been discussed that the width of the superconducting layer plays an important role in the amount of confinement. To fulfill this requirement, the detection process after absorption of a single-photon was studied to find the maximum possible cross section area that the system efficiency is acceptable. As a measure of system performance, a coefficient based on nonequilibrium superconductivity was introduced. Based on the simulation results, I demonstrated that there is no optimum width for a single superconducting wire that is wide enough to cover the entire optical mode and still provide high photon sensitivity. To address this issue a set of wires parallel to the direction of propagation with a spacing much smaller than the transverse mode field size with non-uniform filling factors was proposed [117].

References

[1] E. Knill, R. Laflamme, and G. J. Milburn. A scheme for efficient quantum computation with linear optics. *Nature*, 409(6816):46–52, Jan 4 2001.

[2] Hiroki Takesue, Sae Woo Nam, Qiang Zhang, Robert H. Hadfield, Toshimori Honjo, Kiyoshi Tamaki, and Yoshihisa Yamamoto. Quantum key distribution over a 40-dB channel loss using superconducting single-photon detectors. *Nature Photonics*, 1(6):343–348, 2007.

[3] Matthew E. Grein, Andrew J. Kerman, Eric A. Dauler, Oleg Shatrovoy, Richard J. Molnar, Danna Rosenberg, Jung Yoon, Catherine E. DeVoe, Daniel V. Murphy, Bryan S. Robinson, and et al. *Design of a ground-based optical receiver for the Lunar laser communications demonstration*, pages 78–82. Institute of Electrical and Electronics Engineers, May 2011.

[4] J. Zhang, N. Boiadjieva, G. Chulkova, H. Deslandes, G. N. Gol'tsman, A. Korneev, P. Kouminov, M. Leibowitz, W. Lo, R. Malinsky, O. Okunev, A. Pearlman, W. Slysz, K. Smirnov, C. Tsao, A. Verevkin, B. Voronov, K. Wilsher, and R. Sobolewski. Noninvasive CMOS circuit testing with NbN superconducting single-photon detectors. *Electronics Letters*, 39(14):1086, 2003.

[5] Martin J. Stevens, Robert H. Hadfield, Robert E. Schwall, Sae Woo Nam, Richard P. Mirin, and James A. Gupta. Fast lifetime measurements of infrared emitters using a low-jitter superconducting single-photon detector. *Applied Physics Letters*, 89(3):031109, 2006.

[6] F. Marsili, V. B. Verma, J. A. Stern, S. Harrington, A. E. Lita, T. Gerrits, I. Vayshenker, B. Baek, M. D. Shaw, R. P. Mirin, and et al. Detecting single infrared photons with 93 *Nature Photonics*, 7(3):210–214, Feb 2013.

[7] Robert H. Hadfield. Single-photon detectors for optical quantum information applications. *Nature Photonics*, 3(12):696–705, 2009.

[8] M. K. Akhlaghi and A. H. Majedi. Gated mode superconducting nanowire single photon detectors. *Optics express*, 20(2):1608–1616, Jan 16 2012.

[9] M. G. Thompson, A. Politi, J. C. F. Matthews, and J. L. O'Brien. Integrated waveguide circuits for optical quantum computing. *IET Circuits, Devices & Systems*, 5(2):94, 2011.

[10] Ruoxue Yan, Daniel Gargas, and Peidong Yang. Nanowire photonics. *Nature Photonics*, 3(10):569–576, 2009.

[11] J. P. Sprengers, A. Gaggero, D. Sahin, S. Jahanmirinejad, G. Frucci, F. Mattioli, R. Leoni, J. Beetz, M. Lermer, M. Kamp, S. Hofling, R. Sanjines, and A. Fiore. Waveguide superconducting single-photon detectors for integrated quantum photonic circuits. *Applied Physics Letters*, 99(18):181110, 2011.

[12] L. Colace, G. Masini, F. Galluzzi, G. Assanto, G. Capellini, L. Di Gaspare, E. Palange, and F. Evangelisti. Metalsemiconductormetal near-infrared light detector based on epitaxial Ge/Si. *Applied Physics Letters*, 72(24):3175, 1998.

[13] J. H. J. de Bruijne. Analysis of astronomical data from optical superconducting tunnel junctions. *Optical Engineering*, 41(6):1158, Jun 2002.

[14] Wolfgang Becker, Axel Bergmann, Giovanni L. Biscotti, and Angelika Rueck. *Advanced time-correlated single photon counting techniques for spectroscopy and imaging in biomedical systems*, pages 104–112. Commercial and Biomedical Applications of Ultrafast Lasers IV. SPIE - International Society for Optical Engineering, Jun 2004.

[15] Takashi Isoshima, Yasushi Isojima, Katsuhiko Hakomori, Kazuro Kikuchi, Katsuya Nagai, and Hachiro Nakagawa. Ultrahigh sensitivity single-photon detector using a

Si avalanche photodiode for the measurement of ultraweak biochemiluminescence. *Review of Scientific Instruments*, 66(4):2922, 1995.

[16] Alexei Trifonov, Darius Subacius, Audrius Berzanskis, and Anton Zavriyev. Single photon counting at telecom wavelength and quantum key distribution. *Journal of Modern Optics*, 51(9-10):1399–1415, Jun 2004.

[17] A. Pearlman, A. Cross, W. Slysz, J. Zhang, A. Verevkin, M. Currie, A. Korneev, P. Kouminov, K. Smirnov, and B. Voronov. Gigahertz counting rates of NbN single-photon detectors for quantum communications. *IEEE Transactions on Appiled Superconductivity*, 15(2):579–582, Jun 2005.

[18] J. C Boileau, R. Laflamme, M. Laforest, and C. Myers. Robust quantum communication using a polarization-entangled photon pair. *Physical Review Letters*, 93(22), Nov 2004.

[19] Chandra M. Natarajan, Michael G. Tanner, and Robert H. Hadfield. Superconducting nanowire single-photon detectors: Physics and applications. *Superconductor Science and Technology*, 25(6):063001, 2012; 2012.

[20] Bahaa E. A. Saleh and Malvin C. Teich. *Fundamentals of Photonics (Wiley Series in Pure and Applied Optics)*. Wiley-Interscience, 2007.

[21] M. K. Akhlaghi, H. Atikian, A. Eftekharian, M. Loncar, and A. H. Majedi. Reduced dark counts in optimized geometries for superconducting nanowire single photon detectors. *Optics express*, 20(21):23610–23616, Oct 8 2012.

[22] Aaron J. Miller, Sae Woo Nam, John M. Martinis, and Alexander V. Sergienko. Demonstration of a low-noise near-infrared photon counter with multiphoton discrimination. *Applied Physics Letters*, 83(4):791, 2003.

[23] D. Rosenberg, A. E. Lita, A. J. Miller, S. Nam, and R. E. Schwall. Performance of photon-number resolving transition-edge sensors with integrated 1550nm resonant cavities. *IEEE Transactions on Appiled Superconductivity*, 15(2):575–578, Jun 2005.

[24] Danna Rosenberg, Adriana Lita, Aaron Miller, and Sae Nam. Noise-free high-efficiency photon-number-resolving detectors. *Physical Review A*, 71(6), Jun 2005.

[25] A. Peacock, P. Verhoeve, N. Rando, A. van Dordrecht, B. G. Taylor, C. Erd, M. A. C. Perryman, R. Venn, J. Howlett, and D. J. Goldie. Single optical photon detection with a superconducting tunnel junction. *Nature*, 381(6578):135–137, May 1996.

[26] M. G. Tanner, C. M. Natarajan, V. K. Pottapenjara, J. A. OConnor, R. J. Warburton, R. H. Hadfield, B. Baek, S. Nam, S. N. Dorenbos, and E. Bermudez Urena. Enhanced telecom wavelength single-photon detection with NbTiN superconducting nanowires on oxidized silicon. *Applied Physics Letters*, 96(22):221109, 2010.

[27] Elisabeth Reiger, Sander Dorenbos, Valery Zwiller, Alexander Korneev, Galina Chulkova, Irina Milostnaya, Olga Minaeva, Gregory Goltsman, Jennifer Kitaygorsky, Dong Pan, and et al. Spectroscopy with nanostructured superconducting single photon detectors. *IEEE Journal of Selected Topics in Quantum Electronics*, 13(4):934–943, Jul 2007.

[28] R. Sobolewski, A. Verevkin, G. N. Gol'tsman, A. Lipatov, and K. Wilsher. Ultrafast superconducting single-photon optical detectors and their applications. *IEEE Transactions on Appiled Superconductivity*, 13(2):1151–1157, 2003.

[29] Alex D. Semenov, Gregory N. Goltsman, and Alexander A. Korneev. Quantum detection by current carrying superconducting film. *Physica C: Superconductivity*, 351(4):349–356, 2001.

[30] Anthony J. Annunziata, Orlando Quaranta, Daniel F. Santavicca, Alessandro Casaburi, Luigi Frunzio, Mikkel Ejrnaes, Michael J. Rooks, Roberto Cristiano, Sergio Pagano, Aviad Frydman, and Daniel E. Prober. Reset dynamics and latching in niobium superconducting nanowire single-photon detectors. *Journal of Applied Physics*, 108(8):084507, 2010.

[31] Andrew Kerman, Joel Yang, Richard Molnar, Eric Dauler, and Karl Berggren. Electrothermal feedback in superconducting nanowire single-photon detectors. *Physical Review B*, 79(10), 2009.

[32] L. Zhang, L. Kang, J. Chen, Y. Zhong, Q. Zhao, T. Jia, C. Cao, B. Jin, W. Xu, G. Sun, and P. Wu. Ultra-low dark count rate and high system efficiency single-photon detectors with 50 nm-wide superconducting wires. *Applied Physics B*, 102(4/19/2013):867–871, 2011.

[33] G. Goltsman, O. Minaeva, A. Korneev, M. Tarkhov, I. Rubtsova, A. Divochiy, I. Milostnaya, G. Chulkova, N. Kaurova, and B. Voronov. Middle-infrared to visible-light ultrafast superconducting single-photon detectors. *IEEE Transactions on Applied Superconductivity*, 17(2):246–251, Jun 2007.

[34] A. Hamed Majedi. Theoretical investigations on THz and optical superconductive surface plasmon interface. *IEEE Transactions on Applied Superconductivity*, 19(3):907–910, 2009.

[35] Pierre Berini, Robert Charbonneau, and Nancy Lahoud. Long-range surface plasmons on ultrathin membranes. *Nano Letters*, 7(5):1376–1380, 2007.

[36] John R. Clem and Karl K. Berggren. Geometry-dependent critical currents in superconducting nanocircuits. *Physical Review B*, 84(17):174510, 11-18 2011.

[37] H. L. Hortensius, E. F. C. Driessen, T. M. Klapwijk, K. K. Berggren, and J. R. Clem. Critical-current reduction in thin superconducting wires due to current crowding. *Applied Physics Letters*, 100(18):182602, 2012.

[38] D. Henrich, P. Reichensperger, M. Hofherr, J. M. Meckbach, K. Il'in, M. Siegel, A. Semenov, A. Zotova, and D. Yu Vodolazov. Geometry-induced reduction of the critical current in superconducting nanowires. *Physical Review B*, 86(14):144504, 10-04 2012.

[39] Araldo van de Kraats. Proximity effect in e-beam lithography. http://nanolithography.gatech.edu/proximity.htm.

[40] M. K. Akhlaghi, A. H. Majedi, and J. S. Lundeen. Nonlinearity in single photon detection: Modeling and quantum tomography. *Optics express*, 19(22):21305–21312, Oct 24 2011.

[41] L. N. Bulaevskii, M. J. Graf, C. D. Batista, and V. G. Kogan. Vortex-induced dissipation in narrow current-biased thin-film superconducting strips. *Physical Review B*, 83(14):144526, 04-27 2011.

[42] H. Bartolf, A. Engel, A. Schilling, K. Ilin, M. Siegel, H. W Hbers, and A. Semenov. Current-assisted thermally activated flux liberation in ultrathin nanopatterned NbN superconducting meander structures. *Physical Review B*, 81(2), 2010.

[43] A. Engel, A. D. Semenov, H. W Hbers, K. Ilin, and M. Siegel. Fluctuation effects in superconducting nanostrips. *Physica C: Superconductivity*, 444(1-2):12–18, 2006.

[44] J. Kitaygorsky, I. Komissarov, A. Jukna, D. Pan, O. Minaeva, N. Kaurova, A. Divochiy, A. Korneev, M. Tarkhov, B. Voronov, I. Milostnaya, G. Gol'tsman, and R. R. Sobolewski. Dark counts in nanostructured NbN superconducting single-photon detectors and bridges. *IEEE Transactions on Applied Superconductivity*, 17(2):275–278, 2007.

[45] A. J. Leggett. Percolation, localization, and superconductivity. *Plenum Press*, 1984.

[46] T. Yamashita, S. Miki, K. Makise, W. Qiu, H. Terai, M. Fujiwara, M. Sasaki, and Z. Wang. Origin of intrinsic dark count in superconducting nanowire single-photon detectors. *Applied Physics Letters*, 99(16):161105, 2011.

[47] John R. Clem. Two-dimensional vortices in a stack of thin superconducting films: A model for high-temperature superconducting multilayers. *Phys.Rev.B*, 43(10):7837–7846, Apr 1991.

[48] F. London. *Superfluids: Macroscopic Theory of Superconductivity.* Dover Publications Inc, 1953.

[49] L. Ginzburg and Zh Eksp. On the theory of superconductivity. *Teor. Fiz.*, 23:236, 1952.

[50] J. Pearl. Current distribution in superconducting films carrying quantized fluxoids. *Applied Physics Letters*, 5(4):65, 1964.

[51] Michael Tinkham. *Introduction to Superconductivity: Second Edition*. Dover Publications, New York, 2 edition, 2004.

[52] Ernst Brandt. Square and rectangular thin superconductors in a transverse magnetic field. *Physical Review Letters*, 74(15):3025–3028, 1995.

[53] Vladimir Kogan. Pearls vortex near the film edge. *Physical Review B*, 49(22):15874–15878, 1994.

[54] Ping Ao and David Thouless. Tunneling of a quantized vortex: Roles of pinning and dissipation. *Physical Review Letters*, 72(1):132–135, Jan 1994.

[55] F. Tafuri, J. R. Kirtley, D. Born, D. Stornaiuolo, P. G. Medaglia, P. Orgiani, G. Balestrino, and V. G. Kogan. Dissipation in ultra-thin current-carrying superconducting bridges; evidence for quantum tunneling of Pearl vortices. *Europhysics Letters (EPL)*, 73(6):948–954, 2006.

[56] W. V. Pogosov. Thermal suppression of surface barrier in ultrasmall superconducting structures. *Physical Review B*, 81(18):184517, 05-17 2010.

[57] W. V. Pogosov and V. R. Misko. Vortex quantum tunneling versus thermal activation in ultrathin superconducting nanoislands. *Phys.Rev.B*, 85(22):224508, Jun 2012.

[58] L. N. Bulaevskii, Matthias J. Graf, and V. G. Kogan. Vortex-assisted photon counts and their magnetic field dependence in single-photon superconducting detectors. *Physical Review B*, 85(1):14505, 01-17 2012.

[59] Amin Eftekharian, Haig Atikian, Mohsen K. Akhlaghi, Amir Jafari Salim, and A. Hamed Majedi. Quantum ground state effect on fluctuation rates in nano-patterned superconducting structures. *Physical Review Letters*, page submitted, 2013.

[60] H. Suhl. Inertial mass of a moving fluxoid. *Physical Review Letters*, 14(7):226–229, 1965.

[61] Gianni Blatter, Vadim Geshkenbein, and Valeri Vinokur. Quantum collective creep. *Physical Review Letters*, 66(25):3297–3300, 1991.

[62] Ji-Min Duan and Anthony Leggett. Inertial mass of a moving singularity in a fermi superfluid. *Physical Review Letters*, 68(8):1216–1219, 1992.

[63] E. Chudnovsky and A. Kuklov. Inertial mass of the Abrikosov vortex. *Physical Review Letters*, 91(6), 2003.

[64] Daniel Golubchik, Emil Polturak, and Gad Koren. Mass of a vortex in a superconducting film measured via magneto-optical imaging plus ultrafast heating and cooling. *Physical Review B*, 85(6):60504, 02-13 2012.

[65] Jung Han, June Kim, Min Kim, and Ping Ao. Effective vortex mass from microscopic theory. *Physical Review B*, 71(12), 2005.

[66] Shigehito Miki, Mikio Fujiwara, Masahide Sasaki, Burm Baek, Aaron J. Miller, Robert H. Hadfield, Sae Woo Nam, and Zhen Wang. Large sensitive-area NbN nanowire superconducting single-photon detectors fabricated on single-crystal MgO substrates. *Applied Physics Letters*, 92(6):061116, 2008.

[67] C. M. Natarajan, A. Peruzzo, S. Miki, M. Sasaki, Z. Wang, B. Baek, S. Nam, R. H. Hadfield, and J. L. OBrien. Operating quantum waveguide circuits with superconducting single-photon detectors. *Applied Physics Letters*, 96(21):211101, 2010.

[68] G. N. Goltsman, O. Okunev, G. Chulkova, A. Lipatov, A. Semenov, K. Smirnov, B. Voronov, A. Dzardanov, C. Williams, and Roman Sobolewski. Picosecond superconducting single-photon optical detector. *Applied Physics Letters*, 79(6):705, 2001.

[69] A. M. Kadin, M. Leung, A. D. Smith, and J. M. Murduck. Photofluxonic detection: A new mechanism for infrared detection in superconducting thin films. *Applied Physics Letters*, 57(26):2847, 1990.

[70] W. Zimmermann, E. H. Brandt, M. Bauer, E. Seider, and L. Genzel. Optical conductivity of BCS superconductors with arbitrary purity. *Physica C: Superconductivity*, 183(1-3):99–104, 1991.

[71] D. Walker and K. Scharnberg. Electromagnetic response of high-Tc superconductors. *Physical Review B*, 42(4):2211–2221, Aug 1990.

[72] R. Akis, J. Carbotte, and T. Timusk. Superconducting optical conductivity for arbitrary temperature and mean free path. *Physical Review B*, 43(16):12804–12808, Jun 1991.

[73] D. Mattis and J. Bardeen. Theory of the anomalous skin effect in normal and superconducting metals. *Physical Review*, 111(2):412–417, 1958.

[74] Shu-Ang Zhou. *Electrodynamics of Solids and Microwave Superconductivity*. Wiley-Interscience, 1999.

[75] K. K. Mei and G. C Liang. Electromagnetics of superconductors. *IEEE Transactions on Microwave Theory and Techniques*, 39(9):1545–1552, 1991.

[76] Stefan Alexander Maier. *Plasmonics: Fundamentals and Applications*. Springer, 2007.

[77] J. K. W. Yang, A. J. Kerman, E. A. Dauler, V. Anant, K. M. Rosfjord, and K. K. Berggren. Modeling the electrical and thermal response of superconducting nanowire single-photon detectors. *IEEE Transactions on Applied Superconductivity*, 17(2):581–585, 2007.

[78] J. M. Pitarke, V. M. Silkin, E. V. Chulkov, and P. M. Echenique. Theory of surface plasmons and surface-plasmon polaritons. *Reports on Progress in Physics*, 70(1):1–87, 2007; 2006.

[79] G. B. Hocker and W. K. Burns. Mode dispersion in diffused channel waveguides by the effective index method. *Applied Optics*, 16(1):113, Jan 1977.

[80] Tobias Holmgaard and Sergey Bozhevolnyi. Theoretical analysis of dielectric-loaded surface plasmon-polariton waveguides. *Physical Review B*, 75(24), Jun 2007.

[81] Kin S. Chiang. Performance of the effective-index method for the analysis of dielectric waveguides. *Optics Letters*, 16(10):714, May 1991.

[82] J. Grandidier, G. Colas des Francs, L. Markey, A. Bouhelier, S. Massenot, J. C Weeber, and A. Dereux. Dielectric-loaded surface plasmon polariton waveguides on a finite-width metal strip. *Applied Physics Letters*, 96(6):063105, 2010.

[83] E. Anemogiannis, E. N. Glytsis, and T. K. Gaylord. Determination of guided and leaky modes in lossless and lossy planar multilayer optical waveguides: Reflection pole method and wavevector density method. *Journal of Lightwave Technology*, 17(5):929–941, 1999.

[84] Athanasios Papoulis. *Circuits and Systems: A Modern Approach*. Oxford University Press, USA, 1995.

[85] Junpeng Guo and Ronen Adato. Extended long range plasmon waves in finite thickness metal film and layered dielectric materials. *Optics Express*, 14(25):12409, 2006; 2006.

[86] Dror Sarid. Long-range surface-plasma waves on very thin metal films. *Phys.Rev.Lett.*, 47(26):1927–1930, Dec 1981.

[87] Jason M. Montgomery and Stephen K. Gray. Enhancing surface plasmon polariton propagation lengths via coupling to asymmetric waveguide structures. *Phys.Rev.B*, 77(12):125407, Mar 2008.

[88] I. R. Hooper and J. R. Sambles. Dispersion of surface plasmon polaritons on short-pitch metal gratings. *Phys.Rev.B*, 65(16):165432, Apr 2002.

[89] Andreas Hohenau, Joachim R. Krenn, Andrey L. Stepanov, Aurelien Drezet, Harald Ditlbacher, Bernhard Steinberger, Alfred Leitner, and Franz R. Aussenegg. Dielectric optical elements for surface plasmons. *Optics Letters*, 30(8):893, Apr 2005.

[90] Pierre Berini. Plasmon-polariton waves guided by thin lossy metal films of finite width: Bound modes of asymmetric structures. *Physical Review B*, 63(12):10484–10503, 2001.

[91] Pierre Berini. Plasmon-polariton waves guided by thin lossy metal films of finite width: Bound modes of symmetric structures. *Physical Review B*, 61(15):10484–10503, 2000.

[92] Vikas Anant, Andrew J. Kerman, Eric A. Dauler, Joel K. W. Yang, Kristine M. Rosfjord, and Karl K. Berggren. Optical properties of superconducting nanowire single-photon detectors. *Optics Express*, 16(14):10750, 2008; 2008.

[93] A. G. Kozorezov, A. F. Volkov, J. K. Wigmore, A. Peacock, A. Poelaert, and R. den Hartog. Quasiparticle-phonon downconversion in nonequilibrium superconductors. *Phys.Rev.B*, 61(17):11807–11819, May 2000.

[94] N. Glass and D. Rogovin. Transient electrodynamic response of thin-film superconductors to laser radiation. *Physical Review B*, 39(16):11327–11344, 1989.

[95] R. Romestain, B. Delaet, P. Renaud-Goud, I. Wang, C. Jorel, J-C Villegier, and J-Ph Poizat. Fabrication of a superconducting niobium nitride hot electron bolometer for single-photon counting. *New Journal of Physics*, 6:129–129, 2004.

[96] A. Kadin, M. Leung, and A. Smith. Photon-assisted vortex depairing in two-dimensional superconductors. *Physical Review Letters*, 65(25):3193–3196, 1990.

[97] A. M. Kadin and M. W. Johnson. Nonequilibrium photon-induced hotspot: A new mechanism for photodetection in ultrathin metallic films. *Applied Physics Letters*, 69(25):3938, 1996.

[98] K. Likharev. Superconducting weak links. *Reviews of Modern Physics*, 51(1):101–159, 1979.

[99] A. N. Zotova and D. Y. Vodolazov. Photon detection by current-carrying superconducting film: A time-dependent Ginzburg-Landau approach. *Physical Review B*, 85(2):24509, 01-05 2012.

[100] M. Hofherr, D. Rall, K. S. Ilin, A. Semenov, N. Gippius, H-W Hbers, and M. Siegel. Superconducting nanowire single-photon detectors: Quantum efficiency vs. film thickness. *Journal of Physics: Conference Series*, 234(1):012017, 2010; 2010.

[101] M. Antelius, K. B. Gylfason, and H. Sohlstrom. An apodized SOI waveguide-to-fiber surface grating coupler for single lithography silicon photonics. *Optics express*, 19(4):3592–3598, Feb 14 2011.

[102] M. Kupriyanov and V. Lukichov. Temperature dependence of the pair-breaking current density in superconductors. *Fiz. Nizk. Temp.*, 6(445):445–453, 1980.

[103] Xiaolong Hu, Tian Zhong, James E. White, Eric A. Dauler, Faraz Najafi, Charles H. Herder, Franco N. Wong, and Karl K. Berggren. Fiber-coupled nanowire photon counter at 1550 nm with 24detection efficiency. *Optics Letters*, 34(23):3607, Nov 2009.

[104] Arman B. Fallahkhair, Kai S. Li, and Thomas E. Murphy. Vector finite difference modesolver for anisotropic dielectric waveguides. *Journal of Lightwave Technology*, 26(11):1423–1431, Jun 2008.

[105] Amnon Yariv and Pochi Yeh. *Photonics: Optical Electronics in Modern Communications (The Oxford Series in Electrical and Computer Engineering)*. Oxford University Press, USA, 2006.

[106] A. W. Snyder and J. Love. *Optical Waveguide Theory (Science Paperbacks, 190)*. Springer, 1983.

[107] T. Tamir and S. T. Peng. Analysis and design of grating couplers. *Applied Physics*, 14(3):235–254, Nov 1977.

[108] K. Handa, S. T. Peng, and T. Tamir. Improved perturbation analysis of dielectric gratings. *Applied Physics*, 5(4):325–328, Jan 1975.

[109] S. T. Peng and T. Tamir. TM-mode perturbation analysis of dielectric gratings. *Applied Physics*, 7(1):35–38, May 1975.

[110] M. Neviere, R. Petit, and M. Cadilhac. About the theory of optical grating coupler-waveguide systems. *Optics Communications*, 8(2):113–117, Jun 1973.

[111] S. T. Peng, T. Tamir, and H. L. Bertoni. Theory of periodic dielect waveguides. *IEEE Transactions on Microwave Theory and Techniques*, 23(1):123–133, Jan 1975.

[112] K. Ogawa, W. Chang, B. Sopori, and F. Rosenbaum. A theoretical analysis of etched grating couplers for integrated optics. *IEEE Journal of Quantum Electronics*, 9(1):29–42, Jan 1973.

[113] Kyohei Sakuda and Amnon Yariv. Analysis of optical propagation in a corrugated dielectric waveguide. *Optics Communications*, 8(1):1–4, May 1973.

[114] Kyohei Sakuda and Amnon Yariv. Analysis of optical propagation in a corrugated dielectric waveguide. *Optics Communications*, 8(1):1–4, May 1973.

[115] W. Rigrod and D. Marcuse. Radiation loss coefficients of asymmetric dielectric waveguides with shallow sinusoidal corrugations. *IEEE Journal of Quantum Electronics*, 12(11):673–685, Nov 1976.

[116] C. Ghizoni, Bor-Uei Chen, and Chung Tang. Theory and experiments on grating couplers for thin-film waveguides. *IEEE Journal of Quantum Electronics*, 12(2):69–73, Feb 1976.

[117] Amin Eftekharian, Haig Atikian, and A. Hamed Majedi. Plasmonic superconducting nanowire single photon detector. *Optics Express*, 21(3):3043, Jan 2013.

[118] K. Yu Arutyunov, D. S. Golubev, and A. D. Zaikin. Superconductivity in one dimension. *Physics Reports*, 464(1-2):1–70, 2008.

[119] Jeremy L. O'Brien, Akira Furusawa, and Jelena Vukovi. Photonic quantum technologies. *Nature Photonics*, 3(12):687–695, 2009.

[120] C. Weeks, G. Rosenberg, B. Seradjeh, and M. Franz. Anyons in a weakly interacting system. *Nature Physics*, 3(11):796–801, 2007; 2007.